論文 / 著書情報
Article / Book Information

題目(和文)	
Title(English)	Study on Near-Field Fuel/Air Mixture and Combustion Characteristics of Diesel Spray Flame in High Boosted Surrounding Gas
著者(和文)	ShinabuthDittapoom
Author(English)	Dittapoom Shinabuth
出典(和文)	学位:博士（工学）, 学位授与機関:東京工業大学, 報告番号:甲第12031号, 授与年月日:2021年6月30日, 学位の種別:課程博士, 審査員:小酒 英範,店橋 護,花村 克悟,平井 秀一郎,佐藤 進
Citation(English)	Degree:Doctor (Engineering), Conferring organization: Tokyo Institute of Technology, Report number:甲第12031号, Conferred date:2021/6/30, Degree Type:Course doctor, Examiner:,,,,
学位種別(和文)	博士論文
Type(English)	Doctoral Thesis

Study on Near-Field Fuel/Air Mixture and Combustion Characteristics of Diesel Spray Flame in High Boosted Surrounding Gas

Dittapoom Shinabuth

Advisor: Professor Hidenori Kosaka
Co-advisor: Associate Professor Susumu Sato

Dissertation
submitted in partial fulfillment of the requirements for the degree of
Doctor of Engineering

Department of Mechanical and Aerospace Engineering
Graduate School of Engineering
Tokyo Institute of Technology

June 2021

ABSTRACT

Nowadays, diesel engines introduce high boosted pressure in order to achieve high engine efficiency and reduce soot emission. This extra air is supposed to significantly influence mixing process and improve combustion efficiency. In experiment, surrounding gas conditions of 7 – 46.8 kg/m^3 were prepared by rapid compression and expansion machine RCEM. The nozzle hole length to diameter L/D ratio of 2.77, 3.73, 4.44 and 6.94 were used corresponding to nozzle hole length of 0.5-0.8 mm and orifice diameter of 0.072 – 0.180 mm. In spray visualization part, the close-up region from nozzle tip to 20 mm downstream was focused to simultaneously capture the vapor and liquid phases using shadowgraph and light scattering techniques respectively. The information extracted from the images was then used for estimation of fuel mixture in the near-field spray incorporated with a simple 1D jet model. The result showed that liquid length was dominated by both gas density including gas temperature and rate of fuel injection. The vapor cone angle showed tendency to increase with L/D ratio decreased. The widest vapor cone angle was found at L/D ratio of 2.77 which corresponded to achievement of the highest mass of fuel in vapor phase. It was an evidence that atomization is also one of the essential factors to improve vaporization. At the same gas temperature of 890 K, the fuel mass in liquid phase considerably reduced with increasing gas density. An increase in gas density resulted in substantially increase in entrainment. With identical orifice diameter of 0.180 mm, the smaller L/D=2.77 reported better atomization, shorten liquid length and enhanced entrainment compared with L/D=4.44.

In combustion part, the high-speed flame imaging with soot and NOx measurement were arranged. Flame temperature and KL factor were analyzed based on two-color method. The result showed that with small orifice nozzle of D=0.072 mm (L/D=6.94) and D=0.134 mm (L/D=3.73), low amount of injected fuel resulted in the lower rate of heat release, and low amount of soot emission. With identical orifice size nozzle of D=0.180 mm, the shorter hole length nozzle of L=0.5 mm (L/D=2.77) provided higher entrained gas amount and dense vapor fuel/air mixture was achieved at near-field region. This near-field mixture was found to consistently behave throughout the injection period as it was responsible for shorter ignition delay and combustion drastically promoted with shorter combustion duration. At high boosted gas condition, the lower amount of soot produced by the shorter hole length nozzle was prominently exhibited due to strong combustion resulting in higher flame temperature and soot oxidation performed intensively during late combustion phase. Additionally, NOx emission was found to be a function of equivalence ratio of vapor fuel/air mixture at upstream of ignition and strongly related with flame temperature. The combustion and emission showed significant correlation with near-field spray characteristics.

ACKNOWLEDGEMENTS

I would like to firstly express my special gratefulness to professor Hidenori Kosaka, my major advisor that accepted and educating me the scientific research for a total of eight years and associate professor Susumu Sato for an opportunity to work and study under their supervision as well as assistant professor Tsuyoshi Nagasawa. This study has been conducted as a part of a research project in Rapid Compression-Expansion Machine (RCEM) group, Kosaka-Sato laboratory. I gratefully acknowledge the cooperation of experimental works from Mr. Jeong Jaehoon, Mr. Pop-Paul Ewphun and Mr. Bae Jaeok members in RCEM group and Mr. Athiwat Butmarasri. The study may not be successful without the generous support from Mr. Toshiyuki Hirota and Mr. Akira Akichika, Nobby Tech. Ltd., Japan for providing a high-speed camera (Phantom v2511) with great assistance during operation.

I would also like to express my gratitude to Tokyo Institute of Technology for a scholarship provided by Japanese government (MEXT) in Department of Mechanical and Aerospace Engineering under the Sustainable Engineering Program.

Most importantly, I would like to give this accomplishment to my wife and my parents who always stand by me, encourage me, and have infinite faith in my research work.

CONTENTS

CHAPTER 1
INTRODUCTION

1.1 Background

Diesel engines have been widely used as the power source of commercial vehicles for a long period, which benefits from there high power output and high thermal efficiency compared with the conventional gasoline engines. In recent years, we techniques such as the downsizing engine body, sophisticated injection strategy, common-rail injection system, VGT (Variable Geometry Turbo), and inter-cooled EGR system et al., the diesel engines are capable to meet more stringent exhaust emission regulation. However, direct injection DI diesel engines are confronted by the enhancing requirement for the reduction of NOx and particulate emission, which is one of the main disadvantages compared with the gasoline engines. Moreover, the global warming problem caused by the green-house gas has gotten a great deal of international attention recently, thus the reduction of carbon dioxides emission as well as the improvement of fuel economy will become the most important concern for the automobile industry in the next several decades [1]. Endo S. [2] indicated the gradually tightened exhaust emission regulation of NOx and PM for on-rood diesel in the global main market from past to the future.

Because of the high cost of after treatment facility such as the NOx trapper, the main approach is still to maintain and improve the current techniques, in addition, the advanced combustion concepts such as HCCI (Homogeneous Charge Compression Ignition), PCI (Premixed Compression Ignition), MK (Modulated Kinetics) et al. have been proposed and studied worldwide because of their potential to achieve the ultra-low emission even without the help of after-treatment systems. In order to realize such low temperature and quasi-homogeneous combustion, it is necessary to improve the understanding of the fundamental mechanism of the combustible mixture formation process, which has been proved to be one of the key factors to determine the subsequent combustion and pollutant formation process in the diesel engines [3].

1.2 Literature Reviews

In this section, several experimental data and distinct phenomena from published literatures are reviewed. It starts with development trend of diesel engines, internal flow inside injector nozzle hole, fundamental of liquid fuel spray and diesel combustion as well as emission formation.

1.2.1 Current Trend of Heavy-Duty Diesel Engines

Although diesel engines have dramatically changed over the years, the basic qualities that initially made these engines desirable remain the same which are fuel economy, performance,

reliability, and durability [4]. Performance, reliability, and durability have seen big advances, but perhaps one of the largest changes in the modern diesel engines is the addition of sociability as a key driver for NOx, PM, and CO_2 emissions reductions [5]. In the same fashion, worldwide trend of heavy-duty truck diesel engine technologies is to meet future stringent exhaust emission legislations [6-9]. To meet future exhaust emission standards for heavy-duty truck diesel engines, the application of new technologies including exhaust gas after-treatment systems will be indispensable, especially in view of maintaining or even improving fuel consumption. By evaluating a variety of technology options, both in-cylinder and exhaust gas after-treatment are considered. There has been an improvement in fuel consumption and exhaust emissions through combustion modification by means of high-pressure injection [10, 11], air swirl control [12], the adoption of turbo-intercoolers [13–15], and changing the material of the piston from aluminum to iron [16].

Further improvements of fuel consumption and exhaust emissions, by means of both high-pressure boosting equipped with inter-cooler and high-pressure fuel injection, have been pursued by Aoyagi [17, 18]and Knecht [19, 20]. Particulate emissions decreased significantly with increased intake boost pressure due to the increased available air for soot oxidation at elevated intake pressures, while holding brake specific NOx constant [21]. Fuel quality improvements [22] in terms of less aromatics, increased cetane number, reduced sulfur content, or the addition of oxygenated compounds will significantly contribute to improved emissions not only for new engines but also for the whole fleet of older diesel vehicles. New fuels, such as DME to be injected as a liquid through new fuel injection systems in diesel engines will allow to operate diesel engines absolutely smokeless at diesel like thermal efficiency and significantly reduced gaseous emissions. Such applications are first foreseen primarily in urban areas for urban fleets with central fueling stations.

1.2.2 Internal Flow in Fuel Injector Nozzle Hole

The nozzle internal flow cavitation is regarded as one of the main factors that affect the spray atomization. It is known that under the high injection pressure when the nozzle internal flow velocity is high enough, the cavitation can be generated. This is because that the liquid phase vaporizes instantaneously when the local static pressure which decreases with velocity increasing is lower than the saturated vapor pressure. Hence a two-phase flow forms inside the nozzles. Lecoffre, Y. [31] explained about the cavitation flow which cavitation formation within the phase changing processes was displayed. The low enough pressure and vapor nucleation are two key factors that generate the two-phase flow [23]. The heterogeneous nucleation mainly attributes to the diesel nozzle internal flow [24, 25].The occurrence and development of the cavitation flow is very sensitive to the initial nucleation density and some researchers [26-30]

have studied the initial nucleation density with the cavitation development mathematically, while it did not work very well because of the limitation of nucleation density measurement inside the liquid. That is the reason why the cavitation flow prediction still has difficulties, and until now it just can be reproduced with some models under some assumptions.

When the two-phase flow is of interest under the nozzle fuel injection condition, the initial cavitation and pressure distribution inside the nozzle internal flow was presented. This kind of two phase flow is mainly caused by the hydraulic factors. The sudden change of the nozzle geometric on the hole inlet can generate the vena contracta and with the increasing of the flow velocity. The local pressure is reduced to the critical vapor pressure, where the cavitation bubbles will appear in the downstream. Specially, there are usually 4 kinds of cavitation. There are film-type, string type, hydraulic flip type, and multi-type cavitated flow. These kinds of flow can alter the fuel jet first stage break up directly and during the past several decades, a lot of scholars have tried to reveal the nature behind them. As introduced before, the researchers mainly paid attention to the single-hole nozzles because of the simple geometric and convenience for observation. The enlarged [32-34] and real-size models [35, 36] were conducted to observe the nozzle internal and the cavitation structure. The relationship between the nozzle geometry, cavitation flow, and nozzle discharge coefficient were understood by the researchers. However, limitation of the experimental equipment at that time, the experiments could not be conducted under the real engine operation conditions.

1.2.3 Fundamental of Liquid Fuel Spray

The concept of injecting a liquid through a small hole seems a simple process, but the physics of spray formation proves to be extremely complex. Although the analysis of liquid spray formation is a science discipline on its own, understanding some of its physical aspects is already valuable for numerical modeling. In this section, fundamental of liquid sprays such droplet formation, breakup regimes, and a review of previous studies are presented. These considerations imply no assumptions about the liquid, so they hold for a liquid spray. The description of a full-cone diesel spray includes liquid core, primary breakup, secondary breakup and evaporation regions. The disintegration of liquid jets is described by two main mechanisms. The first mechanism is breakup of the intact liquid core into droplets called primary breakup. This mechanism is characterized by the droplet size and the breakup length, which is defined as the length of the intact liquid core.

Effects inside of the nozzle such as cavitation and transition from nozzle to the dense spray region are the main impact of the primary breakup. The second mechanism is breakup of droplets into smaller ones, which is called secondary breakup. Here, the size of the droplets is a characteristic parameter. The aerodynamic force is a strong parameter relevant to the second

droplet disintegration. Both breakup length and droplet size are dependent on the properties of the liquid and the surrounding gas. One of dominant parameter is the relative velocity between injected liquid and surrounding gas. The primary breakup is the most important mechanism in fuel injection systems, because it determines the size of the droplets that separate from the liquid core, hence therefore also determines evaporation behavior and it marks the starting point for further breakup into smaller droplets. The formation of diesel spray at vicinity of nozzle is visualized by Crua, C. et al. [37]. The experiment was carried out by shadowgraph technique coupled with long range microscope in order to visualize the breakup phenomena. It was found that the tip of the fuel jet was seen to take the shape of an oblate spheroidal cap immediately after leaving the nozzle. The spheroidal cap was found to consist of residual fuel trapped in the injector hole after the end of the injection process. The penetration of different injection pressure of 40 MPa and 160 MPa with gas pressure variation from 4 MPa to 8 MPa are plotted. In addition to a visualization of very vicinity point of nozzle, Manin. J. et al. [38] conducted near-field experiment at the early injection stage of 1.2-mm length from the nozzle exit at high gas pressure and temperature up to 6 MPa and 900 K respectively. They investigated the spray structure after end of injection. It was found that long fuel ligaments and the formation of droplets of relatively large diameter can be seen at relatively low gas temperature while it was not clear indication of drops and ligaments at critical state. Above the critical point on the p-T diagram of operating gas conditions, the transitional region between classical spray breakup and diffusion controlled mixing region that appeared at high gas pressure condition was drawn. Another research area that utilized the supercritical fluid in fuel spray is a rocket engine application.

1.2.4 Mixture Formation and Air Entrainment Processes

The spray evolution and mixture formation process are thought as the most important key factors for the subsequent combustion process. Therefore, it is necessary to understand the spray evolution process deeply which can make a contribution to improve the combustion and emission performance. Plenty of researches focused on spray atomization. The internal turbulent [39, 40], cavitation [41], mutation of the boundary condition at nozzle exit [42] and surface wave caused by aerodynamic interference [43] were found to be dominated during the atomization process separately. Recently, the fundamental experiments especially for the visualization of the spray evolution have shown a good progress. It was found that the spray atomization could not be explained by each factor described above individually. In fact, the atomization processes were affected by the combined factors in which the internal flow turbulence, cavitation instability, and aerodynamic forces are paramount [44, 45]. It is known that the phenomenon of coherent liquid disintegrating into ligaments and large droplets is

defined as primary break-up, and this process usually happens during the internal flow stage even the spray does not emerging from the nozzle hole. This is attributed by the turbulence and cavitation. Wu, P. K. et al. [46] found that the droplets form from turbulent eddies when the surface energy is lower than the radial fluctuations of kinetic energy of the eddy. The turbulent effect highly depends on the flow velocity. When the spray emerges from the nozzle orifice, aerodynamic-induced break-up plays an important role in mixture formation. Previous studies [48, 49] indicated that the coherent liquid does not disintegrate into small droplets immediately and there is a region closed to nozzle exit with ligaments and dense large droplets. This process should also be included into the primary break-up process because the internal turbulence and cavitation exert more decisive effect than aerodynamic forces on fuel disintegration during this process. When the spray extends the break-up length, aerodynamic force leads to the formation of smaller droplets which is called the secondary break-up. This process highly depends on the ratio of aerodynamic to surface tension which is defined as gas phase Weber number. It is well known that different break-up models exist according to different Weber numbers. According to different Weber numbers, different break-up models are classified. [50]. All of these break-up mechanisms works on diesel engine sprays, and the disintegration process contributed by high Weber number takes place in upstream. On the other hand, the break-up process belonging to low Weber number appears in downstream. Compared with the investigation of microscopic spray characteristics in last section, the macroscopic spray characteristics is simpler to observe. Spray tip penetration and spray angle can affect the ambient gas entrainment and the mixture formation quality. Concerning the wall wetting effect of diesel spray, overlong spray tip penetration can result in higher hydrocarbon (HC) and carbon monoxide (CO) emissions, and also higher consumption of fuel and lubricant. However, too short spray tip penetration can decrease the utilization of ambient gas.

As introduced before, the break-up process is mainly dominated by the aerodynamic force which mainly performs as the ambient gas entrainment especially for the secondary break up processes. Therefore, the air entrainment has more attention by researchers. Ricou and Spalding [52] proposed an air entrainment coefficient for a turbulent gaseous jet in 1961 which was injected into the stagnant air with uniform pressure environment by applying the porous-wall technique. The ambient gas time-resolved velocity distribution around the spray was investigated by Ha et al. [53] using a hot wire anemometer. They concluded that the ambient gas mainly entrained into the spray volume form the upstream while the gas was pushed away in the spray tip region. The Laser Doppler Velocimetry (LDV) [54, 55] was used to study the air entrainment in transient diesel spray. They found that the ambient gas entrainment rate during the quasi-stable injection period is constant. The surrounding gas flow behaviors and the relationships between the gas entrained rate and ambient gas density and temperature were also

investigated by them. Recently, the development of Particle Image Velocimetry (PIV) technique reveals more possibility to observe the ambient gas flow and mixture formation processes. There is a common agreement that the surrounding airflow could be divided into three regions based on the flow properties [56-59]. When the injection happens, the ambient gas is pushed away firstly by the spray head (region 1: head vortex zone), and then the ambient gas recirculates along two sides of the spray head (region 2: gas recirculation zone), finally the gas entrains into the following spray zone from the spray tail region (near quasi static zone).

Bruneaux et al. [60] applied Laser Induced Fluorescence (LIF) and PIV techniques simultaneously. They found that there was also evident air entrainment in the recirculation zone. In the recent decades, observing the distributions of vapor and liquid phases of the fuel spray simultaneously has been widely studied by many scholars. Yeh et al. [61] found that the Laser Induced Exciplex Fluorescence (LIEF) technique is suitable for this observation based on the function of vapor concentration and fluorescence intensity. Espey et al., [62] tried to use Rayleigh Scattering (LRS) technique to get images of quantitative fuel vapor concentrations in an evaporating Diesel spray. Moreover, the Spontaneous Raman Scattering (SRS) technique was also used to obtain air-fuel ratio distribution of diesel spray, and Heinze [63] and Rabenstein [64] used this technique and found that the mixture formation process highly depends on the propagation velocity of inner and front spray. Schmalzing et al. [65] applied Shadowgraph and Schlieren Photography technique to observe the liquid and vapor phase penetration. Bruneaux [66] made an investigation on the vapor phase mixing using LIEF and announced that the mixing formation could be improved by increasing injection pressure or reducing hole diameter. Zhang [67] achieved the equivalence ratio distributions of vapor phase and liquid phase of Diesel-liked spray simultaneously by applying the Laser Absorption-Scattering technique (LAS). He revealed that the upstream region of the spray is mainly occupied by high equivalence ratio of liquid phase while the high equivalence ratio vapor region where the auto-ignition possibly taking place locates near the spray tip.

1.2.5 Diesel Combustion and Emissions

The combustion process in Diesel engines is initiated by the auto-ignition, which is resulted from the increasing temperature and pressure inside the cylinder during the compression process. Due to the high calorific value of diesel and high compression ratio of diesel engine, the pressure and temperature around the top dead center (TDC) of 4MPa and 1000 K, respectively [68]. The typical variation trend between fuel injection rate, cylinder pressure, and heat release rate for Diesel engine is shown in Figure 1.1. The combustion process can be divided into three stages. The first one is premixed combustion stage when the premixed mixture formed during the ignition delay, undergoes reaction. The flame temperature and heat release rate increase

quickly and the flame luminosity mainly comes from the weak chemical radicals during this stage. The second one is diffusion combustion stage. The combustion during this stage mainly locates in the periphery region of the spray and the flame luminosity is much higher because of soot incandescence. The last combustion stage usually happens after the end of injection (EOI) when the soot oxidation rate is higher than the production rate.

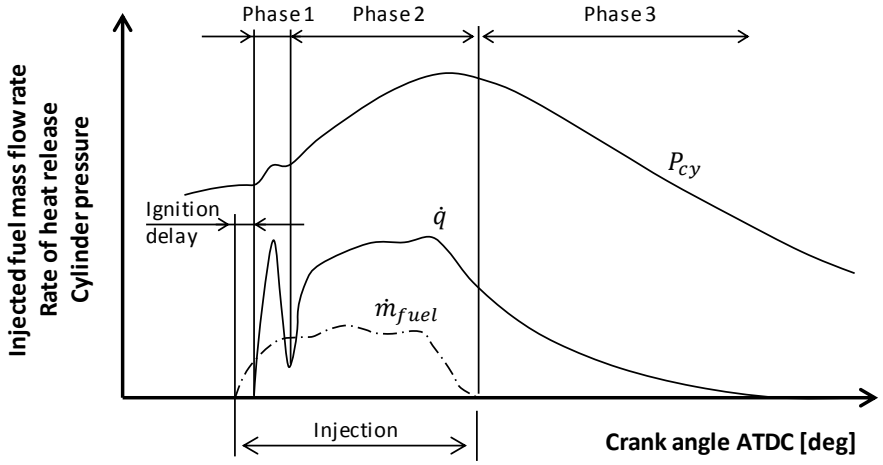

Figure 1.1 Phases of the conventional diesel combustion process.

Dec [69] and Flynn et al. [70] firstly descripted the Diesel engine combustion concept systematically. They conducted the experiment in an optical engine to observe the auto-ignition by adopting chemiluminescence imaging system, to measure soot concentration by using Laser Induced Incandescence (LII) method, and to determine polycyclic aromatic hydrocarbons (PAH) by applying Planar Laser-Induced Fluorescence (PLIF) technique. Several interesting results were exhibited by their experiments. A sheath of fuel vapor and hot air is formed around the spray and also at the leading edge of the spray after the fuel is injected into the chamber. The auto-ignition occurs at multi points nearly simultaneously at the spray downstream region and the premixed combustion mainly occurs volumetrically throughout the cross section of the leading portion of the jet, the injected fuel is heated to 825 K by mixing with the entrained hot gas, and the reactions consumes 15% of the total combustion heat. Moreover, a thin diffusion flame is formed surrounding the burning plume, and the rich combustion products (CO, UHC and particles) are completely burnt in this region. At the same time, the high temperature and high oxygen concentrations at the diffusion flame interface can provide ideal environment for NOx formation reactions [71]. It is well known that it is impossible to both reduce soot and NOx emissions simultaneously in traditional D.I. Diesel engines, and this phenomenon is called as soot -NOx trade off [47].

In the conceptual combustion model introduced above, the ignition process was detected by applying a line-of-sight technique of chemiluminescence recording system, which was not able to provide the spatially resolved information. Moreover, the soot formation processes caused by the soot particles from their precursors have not been investigated deeply. Kosaka et al. [72] presented a detail combustion model as shown in Figure 1.2 which makes the ignition processes spatially clearly and also makes an extensive research on soot formation and oxidation processes.

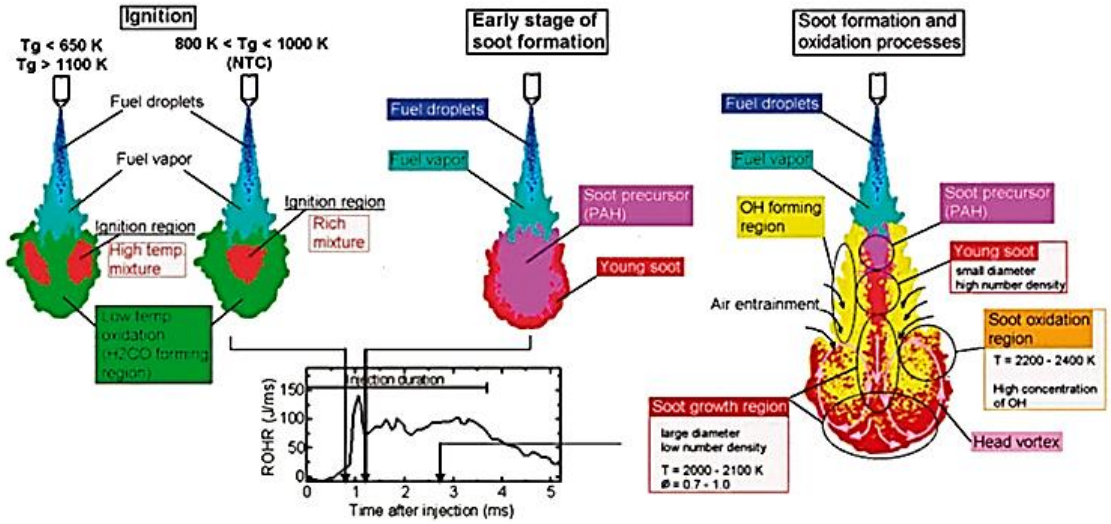

Figure 1.2 Conceptual models of ignition, soot formation, and oxidation process in a diesel spray flame [72].

They applied formaldehyde (HCHO) LIF method to detect the ignition position because the formaldehyde is one of the intermediate species marking the start of oxidation reactions [73]. It was found that the auto-ignition region has highly dependence on the ambient gas temperature. As the soot precursor PAH [74] was observed in the spray downstream at the start of mixing controlled combustion timing. When it comes to the diffusion combustion stage, PAH and young soot are formed in sequence in the central fuel rich region, and grows to the spray tip with the convection flow. Finally, the soot particles are delivered to the upstream side by the head vortex, and then they are oxidized quickly by the lean combustion.

The latest Diesel engine combustion model was proposed by Bruneaux [75, 77]. This model pays more attention to the low temperature fuel decomposition and high temperature burnt gases by applying LIF 355 and hydroxide (OH) LIF techniques compared with the previous combustion models. It is found that the hot ignition occurs inside the HCHO cloud. At the initial

stage of diffusion combustion, the low temperature reaction still occurs in the peripheral region. During the whole mixing controlled combustion process, there is a shell-shaped region of OH between reaction zone of diffusion flame and soot cloud [76]. In these three diesel combustion models, it is evident that there is distance between nozzle tip and the most upstream of stable combustion region during the quasi-steady combustion process which was defined as flame lift-off length [78, 79]. It is believed that the flame lift-off length plays a significant role in combustion and emission processes [80] because the premixing of injected fuel and gas entrainment which have important effects on the subsequent combustion just occurs in the downstream of the lift-off length.

1.3 Objectives

There are two studied parts in this thesis which are a vicinity of nozzle field spray visualization classified as upstream fuel spray study and corresponding combustion and emissions. The thesis objectives are listed as follows:

1. To clarify effect of nozzle specifications and surrounding gas conditions particularly at high density conditions on mixture formation and gas entrainment of diesel spray at near-nozzle field region.

2. To observe corresponding combustion characteristics including soot and NOx emissions in connection with analyzed near-field spray data.

3. To clarify a relation of soot and NOx emissions with combustion characteristics as well as near-field spray behaviors.

1.4 Outline of the Thesis

Generally, this thesis includes two research activities. The first part is a near-field fuel spray visualization and the second part is a combustion part including emissions which both experiment were conducted at the same facilities.

In chapter 1, the recent trend for heavy-duty diesel engine development was reviewed including improvement of fuel/air mixing and after-treatment system. The research objective and outline of the thesis were introduced in this chapter.

In chapter 2, the imaging techniques used to visualization diesel spray and combustion flame were given. For spray imaging, the simultaneous scattering and shadowgraph imaging technique was used. The scattering technique was verified validity that the light only scatters from liquid portion inside spray. In classical shadowgraph, a shadowgraph of diesel sprays includes both shadows of liquid phase and of vapor phase of fuel. In diesel combustion, the flame luminosity is dominated by soot radiation. In this study, the high-speed direct photography was used for diesel flame imaging.

In chapter 3, it was focused on spray formation process. In experiment, four nozzle specifications with variation of nozzle hole lengths and nozzle orifice diameters were used to observe the effect of nozzle specifications on spray formation.

In chapter 4, it was focused on combustion and emission based on measured data and also correlated with spray characteristics in near-field region which was intensively analyzed and discussed in chapter 3. At the last part of this chapter, NOx formation correlated to flame temperatures and equivalence ratio of vapor fuel/air mixture at start of combustion was presented.

In chapter 5, summarization of all the research works undertaken including the key findings was presented. Future research developments and recommendations were also given.

Bibliography

[1] Scolari, P., Towads A Sustainable Mobility at the Turn of the Century: the Environmental Challenge, ATA-Ingegneria Automotoristica, 50, 11-12, 1997.

[2] Endo, S. Powertrain Technologies of Commercial Vehicles for Today and Future, SAE/JSAE International, Keynotes Kyoto, Japan, 2011.

[3] Higgins, B., Siebers, D., and Aradi, A. Diesel Spray Ignition and Premixed-Burn Behavior, SAE paper 2000-01-0940, 2000.

[4] Design and Development of Heavy Duty Diesel Engines A Handbook, Springer, Lakshminarayanan, P. A., Agarwal, Avinash Kumar (Eds.), 2020.

[5] Advanced Direct Injection Combustion Engine Technologies and Development Diesel Engines, Pages 269-288, 2010.

[6] Jiang D M, Huang Z H. Combustion of internal engine alternative fuels, Xi'an Jiaotong University Press, Xi’an, 2007.

[7] Liu S H, Shen Z L, Bi Y H, et al. “Effects of biofuels on performance and emissions of diesel engine under high-altitude hypoxic condition. ” in Transactions of the Chinese Society of Agricultural Engineering (Transactions of the CSAE), 30(13), pp.53-59, 2014.

[8] Yang S, Liu N R, Yang X X. “Experimental study on particle size distribution in diesel exhaust”, in Chinese Journal of Environmental Engineering, 8(11), pp.4892-4896, 2014.

[9] Chauhan B S, Kumar N, Haeng M C. “A Study on the Performance and Emission of a Diesel Engine Fueled with Jatropha Biodiesel Oil and its Blends”, in Energy,37(1), pp.616-622, 2012.

[10] Sugihara, H., Nakagawa, H., Shouyama, K., Yamamoto, A. Hino new K13C diesel engine equipped with common-rail type fuel injection equipment (in Japanese). Engine Technol., 01(04), 40–45, 1999.

[11] Itoh, S., Nakamura, K. Reduction of diesel exhaust gas emission with common rail system (in Japanese, with English summary). J. JSAE, 55(9), 46–52, 2001.

[12] Endo, S., Otani, T., Kakinai, A. An improvement of pumping loss of high boosted diesel engines. SAE paper 885102, 1988.

[13] Suzuki, T., Sato, A., Suenaga, K. Development of a higher boost turbocharged diesel engine for better fuel economy in heavy vehicles. SAE paper 830379, 1983.

[14] Sato, A., Suenaga, K., Noda, M., Maeda, Y. Advanced boost-up in Hino EP100-II turbocharged and charge-cooled diesel engine. SAE paper 870298, 1987.

[15] Stover, T. R., Reichenbach, D., Lifferth, E. The Cummins signature 600 heavy duty diesel engine. SAE paper 981035, 1998.

[16] Tsujita, M., Niino, S., Ishizuka, T., Kakinai, A., Sato, A. Advanced fuel economy in Hino new P11C turbochaged and charge-cooled heavy duty diesel engine. SAE paper 930272, 1993.

[17] Aoyagi, Y. Challenge to super high thermal efficiency of diesel engine (in Japanese). J. JSME, 105(1007), 667–671, 2002.

[18] Aoyagi, Y. Present and future technologies for reducing exhaust emissions in diesel engines (in Japanese, with English summary). J. JSAE, 55(9), 10–16, 2001.

[19] Knecht, W. European emission legislation of heavy duty diesel engines and strategies for compliance. In Proceedings of the Conference on Thermofluidynamic processes in diesel engines (THIESEL 2000), Valencia, Spain, 13-15 September, pp. 289–302, 2000.

[20] Knecht, W. Development trend of heavy duty diesel engines in the view of future European legislation requirements. In Proceedings of the 7th International Conference on Modeling and diagnostics for advanced engine systems (JSME COMODIA 2008), Sapporo, Japan, 28-31 July, pp. 1–8, 2008.

[21] Tanin, K., Wickman, D., Montgomery, D., Das, S. et al., "The Influence of Boost Pressure on Emissions and Fuel Consumption of a Heavy-Duty Single-Cylinder D.I. Diesel Engine," SAE Technical Paper 1999-01-0840, 1999.

[22] Elena Magaril, and Romen Magaril, Fuel Quality: Challenges to the Sustainable Development of Automobile Transport and Approach to Solution, ICSC Web of Conferences, 6 03001, 2016.

[23] Huang Jing-chuan and Han Cheng-cai. Influences of Gas Nucleus Scale on Cavitation. Applied Mathematics and Mechanics, 13(4):359-367, 1992.

[24] Brennen, E. P. Cavitation and Bubble Dynamics. Oxford University Press, Oxford, 1995.

[25] Delale, C. F., Okita, K., and Matsumoto, Y. Steady-State Cavitating Nozzle Flows with Nucleation. J. Fluids Eng., 127(4): 770-777, 2005.

[26] Keller A P. The Influence of the Cavitation Nucleus Spectrum on Cavitation Inception, Investigated with a Scattered Light Counting Method. ASME J. Basic Eng., pp. 917-925, 1972.

[27] Katz, J. and Acosta, A. Observations of Nuclei in Cavitating Flows. Applied Scientific Research, 38(1): 123-132, 1982.

[28] Meyer, R.S., Billet, M.L, and Holl, J.W. Freestream Nuclei and Traveling Bubble Cavitation. ASME J. Fluids Eng., Vol. 114, pp. 672-679, 1992.

[29] Liu, Z. and Brennen, C.E. Cavitation Nuclei Population and Event Rates. Trans. ASME, J. Fluids Eng., vol. 120, pp. 728-737, 1998.

[30] Arora, M., Ohl, C. D., and Lohse, D. Effect of Nuclei Concentration on Cavitation Cluster Dynamics. J. Acoust. Soc. Am., 121(6), pp. 3432-3436, 2007.

[31] Lecoffre, Y. Cavitation Bubble Trackers. Brookfield, VT: A. A. Balkema, 1999.

[32] Soteriou, C., Andrews, R., and Smith, M. Direct Injection Diesel Sprays and the Effect of Cavitation and Hydraulic Flip on Atomization. SAE Technical Paper 950080, 1995.

[33] Afzal, H., Arcoumanis, C., Gavaises, M., and Kampanis, N. Internal Flow in Diesel Injector Nozzles: Modelling and Experiments. IMechE Paper S492/S2/99, 1999.

[34] Roth H, Gavaises M and Arcoumanis C. Cavitation Initiation, Its Development and Link with Flow Turbulence in Diesel Injector Nozzles. SAE Trans. J. Engines, 2002-01-0214 111-3, pp. 561-580, 2002.

[35] Chaves, H., Knapp, M., Kubitzek, A., et al. Experimental Study of Cavitation in the Nozzle Hole of Diesel Injectors Using Transparent Nozzles. SAE Technical Paper No.950290, 1995.

[36] Badock, C., Wirth, R., Fath, A., and Leipertz, A. Investigation of Cavitation in Real Size Diesel Injection Nozzles. Int. J. Heat Fluid Flow, vol. 20, pp. 538-544, 1999.

[37] Crua, C., Shoba, T., Heikal, M., Gold, M. et al., "High-Speed Microscopic Imaging of the Initial Stage of Diesel Spray Formation and Primary Breakup," SAE Technical Paper 2010-01-2247, 2010.

[38] Manin J., Bardi M., Pickett L. M., Dahms R. N. and Oefelein J. C., "Microscopic Investigation of the Atomization and Mixing Processes of Diesel Sprays Injected into High Pressure and Temperature Environments," Fuel 134, 531–43, 2014.

[39] DeJuhasz, K. J. Dispersion of Sprays in Solid Injection Oil Engines. Trans. ASME, 53: 65-77, 1931.

[40] Schweitzer, P. H. Mechanism of Disintegration of Liquid Jets. Journal of Applied Physics, 8: 513-521, 1937.

[41] Bergwerk, W. Flow Pattern in Diesel Nozzle Spray Holes, Proceedings of the Institution of Mechanical Engineers, vol.173, pp.655-674, 1959.

[42] Rupe, J. H. The Liquid-Phase Mixing of a Pair of Impinging Stream. Jet Propulsion Lab. Progress Report.20-195, California Inst. of Technology, Pasadena, 1953.

[43] Castleman, R. A. The Mechanism of the Atomization of Liquids. J. Res. Natl. Bur. Std, 6: 369-376, 1931.

[44] Arcoumanis, C., Gavaises, M., and French, B. Effect of Fuel Injection Processes on the Structure of Diesel Sprays. SAE Technical Paper 970799, 1997.

[45] Smallwood, G. J., and Gülder, Ö. L. Views on the Structure of Transient Diesel Sprays. Atomization and Spray, 10: 355-386, 2000.

[46] Wu, P. K., and Faeth, G. M. Onset and End of Drop Formation along the Surface of Turbulent Liquid Jets in Still Gases. Phy. of Fluids, 7 (11): 2915-2917, 1995.

[47] Baumgarten, C. Mixture Formation in Internal Combustion Engine. Berlin Heidelberg, Springer- Verlag, 2006.

[48] Hiroyasu, H. and Arai, M. Structures of Fuel Sprays in Diesel Engines. SAE Technical Paper, 900475, 1990.

[49] Hiroyasu, H., Arai, M. and Shimizu, M. Break-up Length of a Liquid Jet and Internal Flow in a Nozzle, ICLASS-91, 5th International Conference on Liquid Atomization and Spray Systems, Gaithersburg, Maryland, July, 1991.

[50] Pilch, M., and Erdman, C. A. Use of Breakup Time Data and Velocity History Data to Predict the Maximum Size of Stable Fragments for Acceleration-Induced Breakup of a Liquid Drop. Int. J. Multiphase Flow, 13:741-757, 1987.

[51] F. P. Ricou and D. B. Spalding. Measurements of entrainment by axysymmetrical turbulent jets.J.Fluid Mech., 11(01):21–32, 1961.

[52] Ricou, D. R., and Spalding, D. B. Measurement of Entrainment by Axis-Symmetrical Turbulent Jets. J. Fluid Mech., 11:21-32, 1961.

[53] Ha, J. Y., lida, N., Sato, G. T., Hayashi, A. and Tanabe, H. Experimental Investigation of the Entrainment into Diesel Spray. SAE Technical Paper 841078, 1984.

[54] Cossali, G. E., Brunello, G., and Coghe, A. LDV Characterization of Air Entrainment in Transient Diesel Sprays. SAE Technical Paper 910178, 1991.

[55] Cossali, G. E., Gerla, A., Coghe, A., and Brunello, G. Effect of Gas Density and Temperature on Air Entrainment in a Transient Diesel Spray. SAE Technical Paper 960862, 1996.

[56] Araneo, L., Coghe, A., Brunello, G., and Cossali, G. Experimental Investigation of Gas Density Effects on Diesel Spray Penetration and Entrainment, SAE Technical Paper, 1999-01-0525, 1999.

[57] Rajalingam, B. V., and Farrell, P. V. The Effect of Injection Pressure on Air Entrainment into Transient Diesel Sprays. SAE Technical Paper 1999-01-0523, 1999.

[58] Rhim, D.R., and Farrell, P. V. Air Flow Characteristics Surrounding Evaporating Transient Diesel Sprays. SAE Technical Paper 2002-01-0499, 2002.

[59] Sepret, V., Bazile, R., Marchal, M., and Couteau, G. Effect of Ambient Density and Orifice Diameter on Gas Entrainment by a Single-Hole Diesel Spray. Exp. Fluids, 49:1293-1305, 2010.

[60] Bruneaux, G., Causse, M., and Omrane, A. Air Entrainment in Diesel-Like Gas Jet by Simultaneous Flow Velocity and Fuel Concentration Measurements, Comparison of Free and Wall Impinging Jet Configurations. SAE Technical Paper 2011-01-1828, 2011.

[61] Yeh, C., Kamimoto, T., Kosaka, H., and Kobori, S. Quantitative Measurement of 2-D Fuel Vapor Concentration in a Transient Spray via Laser-Induced Fluorescence Technique. SAE Technical Paper 941953, 1994.

[62] Espey, C., Dec, J. E., Litzinger, T. A., and Santavicca, D. A. Planar Laser Rayleigh Scattering for Quantitative Vapor-Fuel Imaging in a Diesel Jet. Combustion and Flame, 109: 65-78, 1997.

[63] Heinze, T., and Schmidt, T. Fuel-Air Ratios in a Spray, Determined between Injection and Autoignition by Pulsed Spontaneous Raman Spectroscopy. SAE Technical Paper 892102, 1989.

[64] Rabenstein, F., Egermann, J., and Leipertz, A. Quantitative Analysis of Vapor Phase Structures in Transient Liquid Fuel Sprays. COMODIA, Kyoto, Japan, 1998.

[65] Schmalzing, C. O., Stapf, P., Maly, R. R., Renner, G., Stetter, H., and Dwyer, H. A. A Holistic Hydraulic and Spray Model- Liquid and Vapor Phase Penetration of Fuel Sprays in DI Diesel Engines. SAE Technical Paper 1999-01-3549, 1999.

[66] Bruneaux, G., Verhoeven, D., and Baritaud, T. High Pressure Diesel Spray and Combustion Visualization in a Transparent Model Diesel Engine. SAE Technical Paper 1999-01-3648, 1999.

[67] Zhang, Y. Y., A Study on Mixture Formation in Diesel Sprays with Split Injection Strategy. Dissertation, University of Hiroshima, 2001.

[68] Kamimoto, T., and Kobayashi, H. Combustion Processes in Diesel Engines. Progress in Energy and Combustion Science, 17:163-189, 1991.

[69] Dec, J. E. A Conceptual Model of DI Diesel Combustion Based on Laser-Sheet Imaging. SAE Technical Paper 970873, 1997.

[70] Flynn, P. F., Durrett, R. P., Hunter, G. L., zur Loye, A. O., Akinyemi, O. C., Dec, J. E., and Westbrook, C. K. Diesel Combustion: An Integrated View Combining Laser Diagnostics, Chemical Kinetics, And Empirical Validation. SAE Technical Paper 1999-01-0509, 1999.

[71] Zeldovich, Y. B., The Oxidation of Nitrogen in Combustion and Explosions. Acta Physicochim. 21:577, 1946.

[72] Kosaka, H., Aizawa, T., and Kamimoto, T. Two-Dimensional Imaging of Ignition and Soot Formation Process in a Diesel Flame. International Journal of Engine Research, 6(1): 21-42, 2005.

[73] Kosaka, H., Drewes, V., Catalfamo, L., Aradi, A. A., Iida, N., and Kamimoto, T. Two–Dimensional Imaging of Formaldehyde Formed During the Ignition Process of a Diesel Fuel Spray. SAE Technical Paper 2000-01-0236, 2000.

[74] Tree, D. R., and Svensson, K. I. Soot Processes in Compression Ignition Engines. Progress in Energy and Combustion Science, 33: 272-309, 2007.

[75] Bruneaux, G. Combustion Structure of Free and Wall-Impingement Diesel Jets by Simultaneous Laser-Induced Fluorescence of Formaldehyde, Poly-Aromatic Hydrocarbons, and Hydroxides. International Journal of Engine Research, 9: 249-265, 2008.

[76] Li, K., Dong, P., Matsuo, T., Shi, B. et al. Characteristics of Diesel Spray Flame under Flat Wall Impinging Condition --LAS, OH* Chemiluminescence and Two Color Pyrometry Results," SAE Technical Paper 2014-01-2636, 2014.

[77] Bruneaux, G. Combustion Structure of Free and Wall-Impingement Diesel Jets by Simultaneous Laser-Induced Fluorescence of Formaldehyde, Poly-Aromatic Hydrocarbons, and Hydroxides. International Journal of Engine Research, 9: 249-265, 2008.

[78] Higgins, B., and Siebers, D. Measurement of the Flame Lift-Off Location on DI Diesel Sprays Using OH Chemiluminescence. SAE Technical Paper 2001-01-0918, 2001.

[79] Siebers, D., and Higgins, B. Flame Lift-Off on Direct-Injection Diesel Sprays Under Quiescent Conditions. SAE Technical Paper 2001-01-0530, 2001.

[80] Chraplyvy, J., and Karlsson, A. Flame Lift-off in Diesel Spray. Symposium (International) on Combustion, 26: 2557-2564, 1996.

CHAPTER 2
IMAGING TECHNIQUES FOR LIQUID-GAS PHASES AND COMBUSTION IN DIESEL SPRAY FLAME

2.1 Simultaneous Imaging of Liquid and Gas Phases

The combustion event occurring inside a diesel engine is initiated by an auto ignited diffusion flame. Violent chemical reactions usually take place within the boundary sections of the fuel jet where favorable equivalence ratios for combustion are formed. Due to this nature of the combustion process, the mixing process of the fuel and air has a significant impact on the combustion quality of the fuel, thus affecting the energy conversion efficiency and the emission performance of the engine. Understanding of diesel spray characteristics has been widely investigated [1-3]. Two major approaches, experiments and modeling, have been extensively adopted to understand detailed characteristics of diesel sprays, including the penetration rates, spray dispersion, vaporization, and fuel distribution. Volumes of experimental data obtained from various test setups lay a foundation for this research area. Test conditions cover a wide range of fuel injection pressures, nozzle geometries, ambient densities, ambient temperatures, and ambient gas compositions. Constant volume pressurized chambers capable of maintaining diesel-engine-like environments are commonly used for diesel spray investigation [3-5]. A number of visualization techniques have been developed and applied to this research area. Shadowgraph imaging [6-9] is widely used for visualization of transparent media with temperature or density gradient. The relatively simple optical setup provides sensitivity to the gradient of index of refraction caused by the difference in density. Such techniques are suitable for observing diesel spray formation where significant differences between densities of liquid fuel, vaporized fuel, and ambient gas exist. With the help of current technology, high speed cameras, satisfactory temporal resolution can be achieved. The disadvantage of shadowgraph imaging is that the sensitivity of the optics greatly affects the measurements such as spray cone angle [2] and penetration in vaporizing spray. Mie scattering is another commonly used technique which takes advantage of elastic scattering of light with broken-up liquid particles of typical diameters comparable to wavelength of incident light. Only liquid parts of the spray will yield a signal, making Mie scattering an ideal method for liquid spray visualization [10, 11]. Rayleigh scattering, on the other hand, is used to visualize gaseous fuel molecule distribution. Rayleigh scattering images acquired by Idicheria and Pickett [12] showed the varying gaseous fuel concentration distribution within the cross-sectional area of the jet plume. However the liquid part of the plume has to be avoided from the incident laser sheet to reduce interference on the Rayleigh image.

As vapor and liquid fuel phases exist concurrently in diesel spray, the quantitative

measurement becomes complicated. Some researchers have proposed valuable approaches in attempting such measurements including laser induced exciplex fluorescence LIEF [13-15]. The planar laser-induced exciplex fluorescence (PLIEF) technique has also been used to visualize and measure the fuel/air concentration fields in both liquid and vapor phases of direct injection (DI) diesel sprays. In the recent decade, Suzuki et al. [16] and Zhang et al. [17, 18] proposed an optical diagnostic based on ultraviolet-visible laser absorption-scattering LAS to detect the vapor concentration and droplet density inside a fuel spray. As the LAS technique can provide quantitative concentration information of both vapor and liquid droplets, the signal-to-noise ratio is high, and not easily affected by oxygen quenching which is often encountered in LIEF.

In this section, the simultaneous liquid and gas phase imaging technique based on shadowgraph and scattering measurement method is described including optical setup and processing the images for obtaining the spray characteristics under wide range of surrounding gas conditions.

2.1.1 Scattering imaging technique

Scattering is the light-particle interaction which acts to transform an incident electromagnetic radiation into a new electromagnetic radiation of identical or different properties. During this light-particle interaction, the incident electromagnetic energy can also be transformed into another sort of energy. The scattering of light is to affirm that scattering is caused by the heterogeneity of a system. Assuming for example that a beam of light traverses a perfectly homogeneous medium, no scattering events would occur. As only a vacuum can be defined as a perfect homogeneous medium, all other media scatter light when illuminated by electromagnetic radiation. Depending on the arrangement of atoms or molecules in a medium, scattering will be more or less effective. When a particle such as an atom, a molecule, a liquid or a solid particle is illuminated by an electromagnetic wave, the discrete electric charges (the electrons and protons) are set into an oscillatory motion by the electric field of the incident wave. This oscillation causes the acceleration of the electric charges, which produces radiation of electromagnetic energy in all directions.

Figure 2.1 shows the volume-illumination light scattering imaging arrangement. The laser directs through the compression chamber with diesel spray penetrating from top to bottom. Once the light interacts with fuel droplets, scattering signal is observed and imaged through a high-speed camera placed in 90-degree angle difference from the laser path. Scattering image is sensitive to the liquid phase of the fuel spray. The liquid boundary and liquid length are detected using the methodology described in the next section of processing of spray photograph.

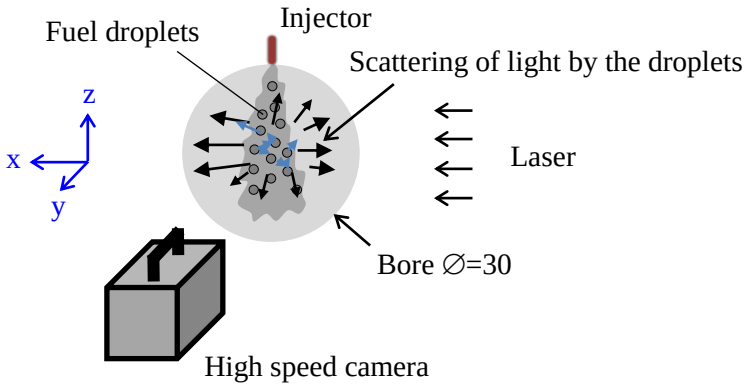

Figure 2.1 Side-view scattering imaging technique. The angle between laser light and camera view is 90 degrees.

2.1.2 Shadowgraph imaging technique

Shadowgraph imaging has been used for many years to identify refractive index gradients in various experiments [19]. For vaporizing diesel sprays, these techniques show the boundary between vaporized fuel and background ambient gases because the refractive index differences exist between the fuel and ambient gases and density gradients created in the ambient gases as the vaporized fuel spray cools the ambient. Of course, strong density and refractive index gradients are also created at combustion interfaces where the high-temperature combustion creates low-density regions. Shadowgraph techniques therefore provide important information about the temperature and composition of the system. The high-speed shadowgraph visualization is possible using simple continuous light sources such as lamps. In addition to high-speed shadowgraph imaging of diesel sprays, single-shot shadowgraph imaging has been applied to diesel sprays using short-pulse light sources [20-23].

Figure 2.2 collimated light is passed along a line of site through the compression chamber and directed onto a high-speed camera sensor. From this setup, shadowgraph image is used to identify the vapor boundary of diesel spray.

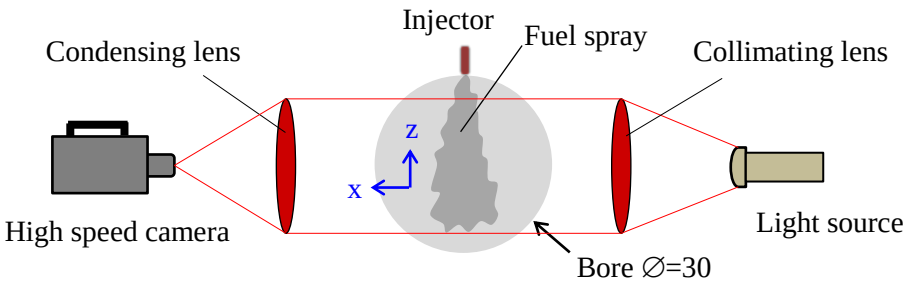

Figure 2.2 Shadowgraph imaging technique. It is the line-of-sight imaging.

2.1.3 Liquid-gas phase measurement system

In this research for near-field spray visualization section, it is intended to separately image both vapor and liquid phases of fuel spray in order to observe spray structure and vaporization characteristics of injected fuel when emerges into large variation of gas condition. The light scattering imaging technique is properly selected as an indicator of liquid phase and high density spray while the shadowgraph imaging is used for identification of vapor boundary of the spray.

In the experiment, the desired surrounding gas conditions conducted in this work were prepared by rapid compression machine RCM [24]. The compression chamber and optical accessible arrangement are schematically shown in Figure 2.3 and the layout of quartz window is shown in Figure 2.4b. In this setup, 0-20 mm from nozzle tip towards downstream spray was taken by means of simultaneous classical shadowgraph and scattering imaging technique. Specifications of imaging devices are listed in Table 2.1. The pulsed-diode laser (CAVILUX HF) with wave length of 640 nm was used as a light source for both scattering and shadowgraph. With this system, the collimated incident laser light with beam diameter of approximately 20 mm was directed through the quartz window placed in front of the compression chamber. The fuel spray was achieved between two prisms, which were homogenously built with a quartz window. The prisms were used for irradiating the spray and imaging of shadowgraph. Once the fuel jet left the nozzle, the liquid fuel core and droplets were immediately illuminated by the light beam. The light emerged from right to left side perpendicular to the camera view. The laser light was pretty strong to illuminate the liquid droplets. From that, the neutral-density filter (ND 2.0) corresponding to transmittance of 0.01 was stuck in front of the quartz at the shadow side to reduce amount of laser light and made shadowgraph to be visible clearly. Both images were captured at the same time by one high-speed CMOS camera (MEMRECAM ACS-1) fitted with 105-mm-macro lens (f/2.8 Micro-NIKKOR). The captured area was 22 x 33 mm at 8.3 μs frame interval and the final optical resolution was 10 pixels/mm. An example of a taken photograph is also included in Figure 2.3 showing the shadowgraph and scattering images on the left and right side respectively. During the experiment, the pulse duration remained constant which was set to be 90 ns for all operating gas conditions. One should be noted that the shadowgraph and scattering images were simultaneously taken using a high speed camera. With this, those photographs were taken at the view of 90-degree angle difference.

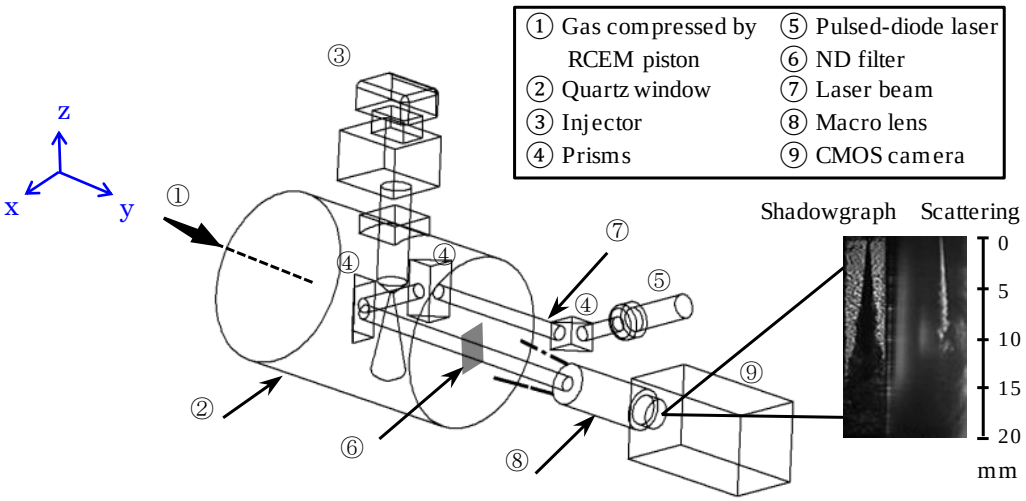

Figure 2.3 Optical arrangement for simultaneous scattering and shadowgraph imaging. Note that scattering was imaged with 90-degree difference from shadowgraph path.

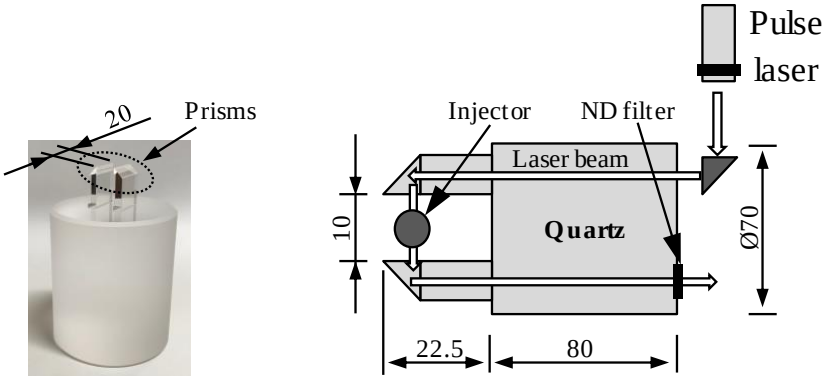

(a) (b)

Figure 2.4 (a) Special designed quartz window with prisms and (b) Top-view layout in mm (not to scale).

Table 2.1 Imaging condition.

Light source	
Type	Pulsed-diode laser
Wave length	640 nm
Pulse duration	90 ns
High-speed camera and Lens	
Frame rate	120 kFPS
Exposure	1.5 μs
Resolution	224 x 336 pixels
Captured area	22 x 33 mm
Lens	105 mm f/2.8

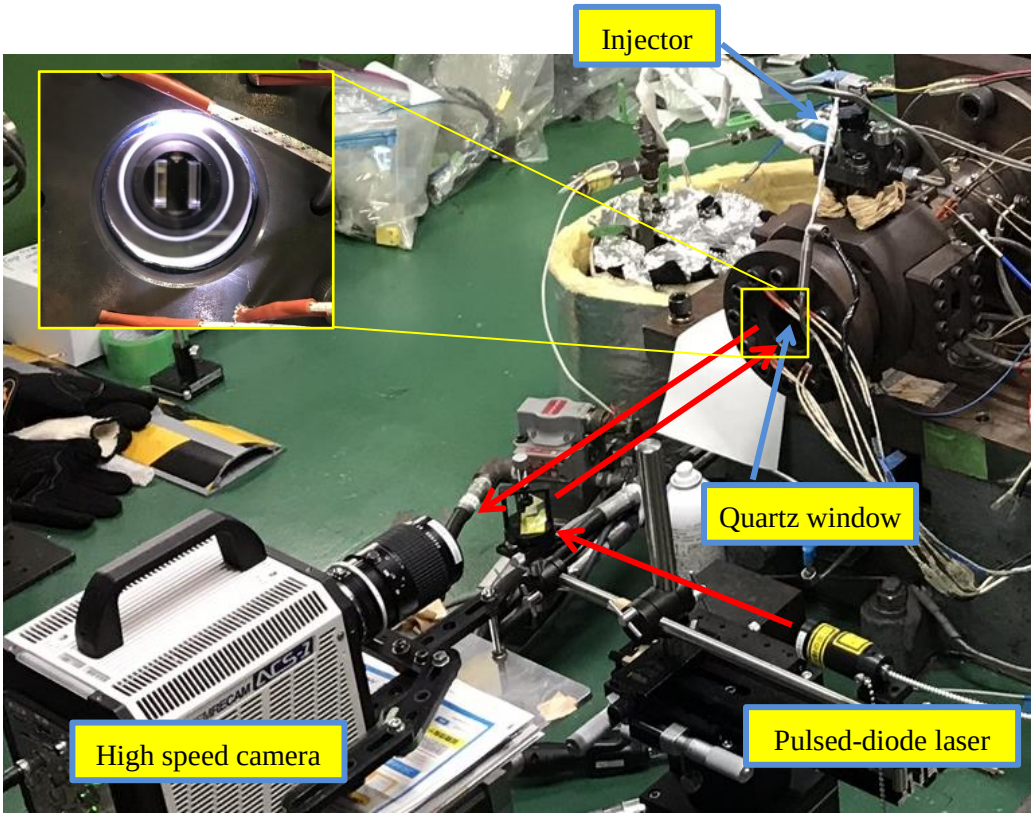

Figure 2.5 Real experimental setup for simultaneous scattering and shadowgraph imaging.

2.2 Estimation of Scattering Intensities

Mie scattering is elastic scattered light of particles that have a diameter similar to or larger than the wavelength of the incident light. The Mie signal is proportional to the square of the particle diameter. Mie scattering is much stronger than Rayleigh scattering and, therefore, a potential source of interference for this weaker light scattering process. There is a strong angular dependency of the scattered intensity especially for smaller particles which has to be considered for successful Mie imaging experiments. The scattering efficiency factor Q_{sct} can be either lower or higher than the unity 1, this means that for an illuminated particle, the area shadowed can be bigger or smaller than the geometrical cross-section. For droplets bigger than the wavelength for example λ = 532 nm, the shadowed area is generally bigger than the geometrical cross-section area. This is partially due to the fact that some energy is removed by interference between the scattered radiation and the incident wave. Figure 2.6 shows the evolution of the scattering efficiency factor Q_{sct} as a function of the particle diameter considering an incident illumination wavelength of 532 nm. Based on 1D jet model developed by Musculus and Kattke [25], the fuel concentration inside the spray at specific surrounding gas condition can be estimated as shown in Figure 2.7.

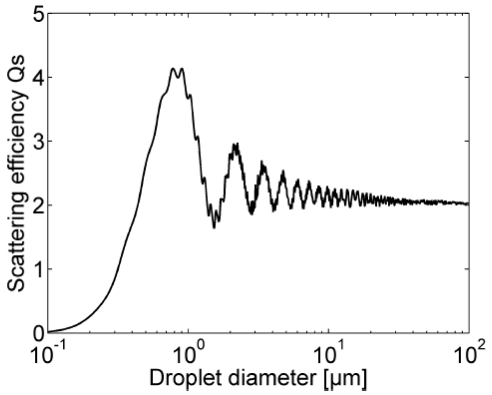

Figure 2.6 Scattering efficiency factor of a spherical droplet (n=1.42) as a function of the droplet diameter. Incident radiation wavelength is 532 nm [26].

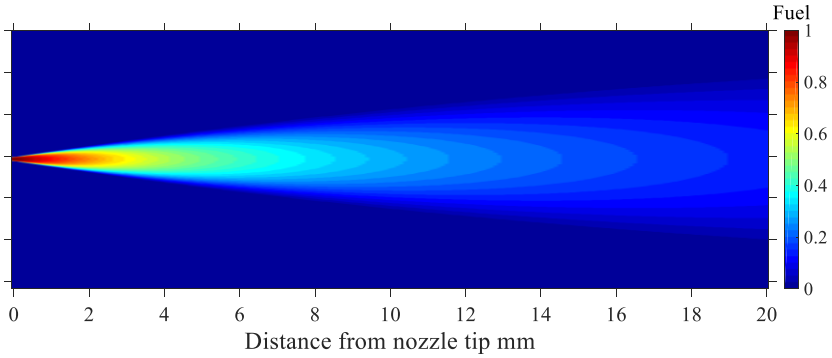

Figure 2.7 Estimated fuel concentration at near-field region based on experimental data and 1D jet model [25]. Gas condition: 890 K, 46.8 kg/m^3. Calculation scheme is described in Chapter 3.

The scattering intensity can be obtained by the following expression

$$\frac{I_{Mie}}{I_0} = Q_{sct} N_f \left(\frac{\pi d^2}{4}\right) \tag{2.1}$$

where I_0 is the intensity of the incident laser light, Q_{sct} is the scattering efficiency which is assumed to be $Q_{sct} = 2$ for light scattered from droplet diameter of 20 μm, N_f is the number density of liquid phase fuel which can be obtained from the estimated fuel concentration in specified scattering zone based on Musculus's model [25], d is the diameter of the particle which is equal to the droplet diameter.

Rayleigh scattering is the elastic scattering of light by particles much smaller than the wavelength of the light. That is the case for gas phase molecules and, therefore, this method is suited for laser imaging in gases. Rayleigh scattering of sunlight by atmospheric molecules is the reason for the observed blue color of the sky, because the scattering efficiency varies inversely with the fourth power of the wavelength. For a single component gas with known scattering cross section the Rayleigh signal is directly proportional to the gas density. The scattered light is almost at the same wavelength as the incident light i. e. Rayleigh scattering is not species selective. Rayleigh scattering requires either constant gas composition or known mole fractions of all major species for the density measurement of a gas mixture. In some cases Rayleigh scattering is stronger for one species than another, and it can be used to image mixing processes such as fuel/air mixing. Rayleigh scattering is much weaker than Mie scattering. For multicomponent mixture of ideal gases, the Rayleigh scattering intensity I_R is given as

$$\frac{I_R}{I_0} = N_m \sum_i X_i \, \sigma_i \tag{2.2}$$

where I_0 is the intensity of the incident laser light, N_m is the number density of the mixture which is $N_m = N_f + N_{amb}$, X_i is the mole fraction with relation of $X_f + X_{amb} = 1$ and σ_i is the scattering cross section. The ratio of cross sections [27] for the diesel reference fuel and air was determined to be $\sigma_f/\sigma_a = 305$.

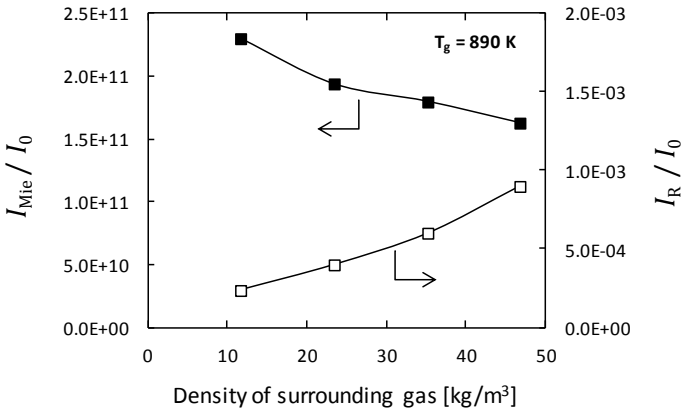

Figure 2.8 Calculated Mie scattering I_{Mie} (liquid phase scattered) and Rayleigh scattering I_R (gas phase scattered) with different surrounding gas density at gas temperature of 890 K.

The scattering technique employed in this study was verified validity whether light scatters only from liquid or includes gas phase. In Figure 2.8, relative intensity difference between Rayleigh and Mie scattering regimes showed as entirely different as in order of 13-14 for wide range of surrounding gas conditions of 11.7-46.8 kg/m^3 which corresponds to the gas pressure of 3-12 MPa. Therefore, the large difference between those scattering regimes is fairly reasonable for the scattering imaging technique used for quantification of liquid portion inside spray.

2.3 Processing of Spray Photograph

The microscopic imaging was arranged to simultaneously perform the high-speed shadowgraph and scattering focusing on near-field region. From the setup, the 20-mm spray far from nozzle tip was appropriately captured with two types of spray information contained in a single shot of imaging. The shadowgraphy was used to represent the vapor phase spray boundary which includes fuel vapor and entrained gas. The scattering image corresponded to the liquid phase because of high density portion in the spray that dense enough to sufficiently light scattered.

2.3.1 Liquid boundary detection

Figure 2.9 shows the process for obtaining the liquid phase scattering. There are 2 instantaneous images needed for processing. One is Figure 2.9a is the background image at time before fuel injection which is assigned as I_0 while $I_{1.3}$ is an instantaneous image at 1.3 ms ASOI as shown in Figure 2.9b. Each image consists of shadowgraph on the left side and scattering image on the right side. The fuel injects in the vertical direction from top to bottom. However, there was a possible case that a slightly inclined spray image was observed due to mounting issue. The spatial noise from variation of turbulence of surrounding gas is reduced from raw image by subtraction the previous image as shown in Figure 2.9c. To identify the liquid boundary, the image intensity in cross section of the scattering image was considered which are 5 mm and 8.7 mm distance in z-direction far from nozzle tip. Figure 2.10 shows the cross-sectional image intensities for two different lines.

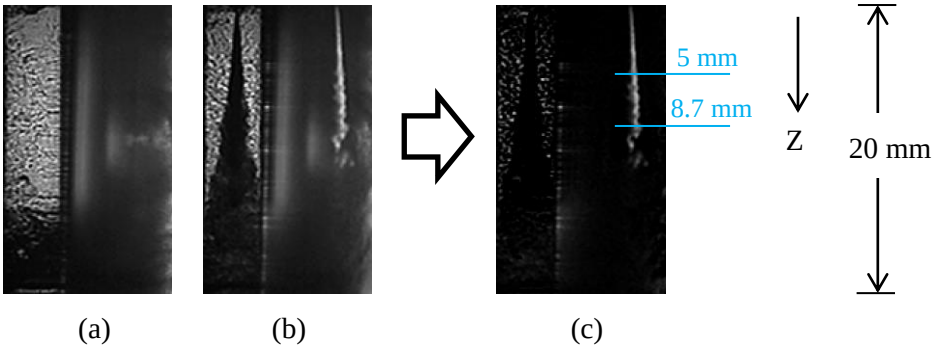

Figure 2.9 Procedures of scattering image subtraction. (a) Background image at 0 ms, (b) Spray image at 1.3 ms ASOI, and (c) Image subtraction of $I_{1.3}$ - I_0. Gas condition of 890 K, 46.8 kg/m^3. Nozzle of D=0.180 mm, L=0.5 mm, L/D=2.77.

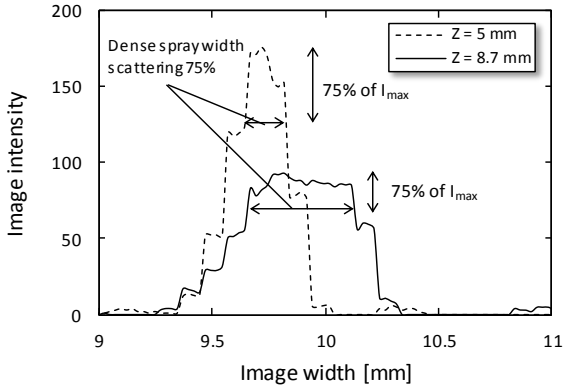

Figure 2.10 Cross-sectional image intensity of the processed scattering image.

The purpose of scattering image is to observe the signal that identifies the dense fuel or liquid portion inside the spray, so that it is reasonable to consider the maximum scattering intensity as a value for thresholding. In this case, the 75% of maximum image intensity is used to show for thresholding the scattering image to obtain the liquid phase fuel. The three value different of 65%, 75% and 85% of maximum image intensity are used for comparison whether is suitable or not. Figure 2.11(a-c) show binarized images which is executed by three threshold values. Figure 2.11(d-f) show corresponding detected liquid boundary which is superimposed over the raw images. It can be seen that the liquid boundary is found to be over compared the raw scattering image in liquid width for 65% of maximum image intensity. On the other hands, the 85% of maximum image intensity seems to be not enough detected liquid portion. For 75% of maximum image intensity, it is found to be a suitable condition for thresholding which can detect the liquid boundary at the dense region appropriately.

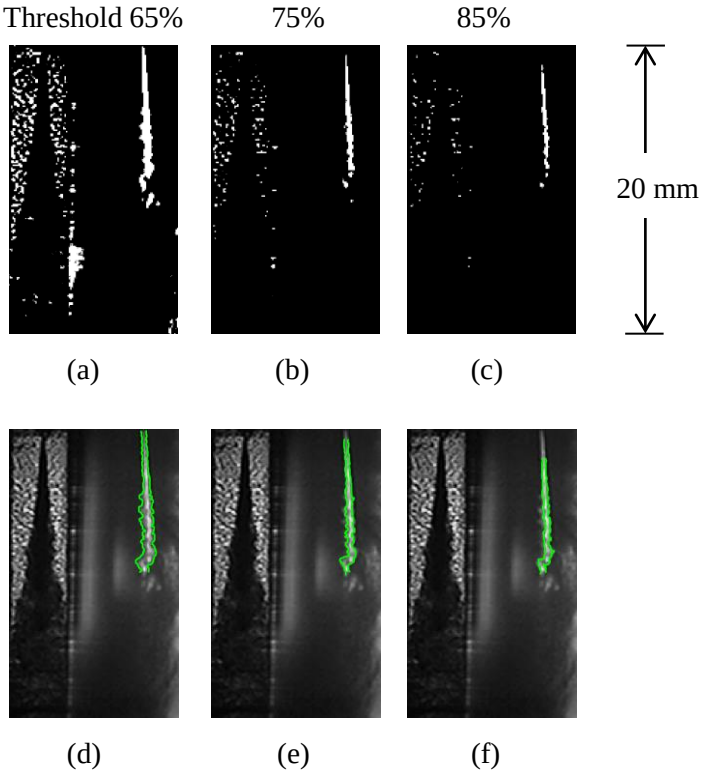

Figure 2.11 Variation of thresholds for liquid fuel boundary at 1.3 ms ASOI. (a-c) Binarized images after thresholding, and (d-f) Detected liquid boundaries superimposed over the raw images.

2.3.2 Vapor boundary detection

Figure 2.12 shows the process for obtaining the gas phase boundary. In fact, inside the spray plume consists of liquid fuel, vapor fuel and entrained gas. There are 2 instantaneous images needed for processing. One is Figure 2.12a is the background image at time before fuel injection which is assigned as I_0 while $I_{1.3}$ is an instantaneous image at 1.3 ms ASOI as shown in Figure 2.12b. Each image consists of shadowgraph on the left side and scattering image on the right side. It is noted that the circular averaging filter is applied to both raw images in order to reduce the spike values or noises due to variation of surrounding gas. The image subtraction is shown in Figure 2.12c. In this step, one high image intensity is clearly identified before it is inverted based on gray scale image as shown in Figure 2.12d. All pixel values containing inside the images are observed for arrangement of its level as shown in Figure 2.13. The purpose of this step is to identify the sharp gradient between surrounding and the spray plume boundary. Therefore, image intensity of about 170 is likely reasonable value as it can cut almost all high intensity image cells and remains the low one for gas phase. The width of the spray is detected by the strategy shown in Figure 2.14. In order to reach enough detection accuracy of the gas phase boundary, three threshold are used which is 160, 170 and 180 as shown in Figure 2.15. Figure 2.15(a-c) show the binarized images executed by three thresholds while Figure 2.15(d-f) show the detected vapor fuel boundaries. It is observed that the threshold of 170 is the most appropriate for using to capture the edge of spray plume imaged by shadowgraph.

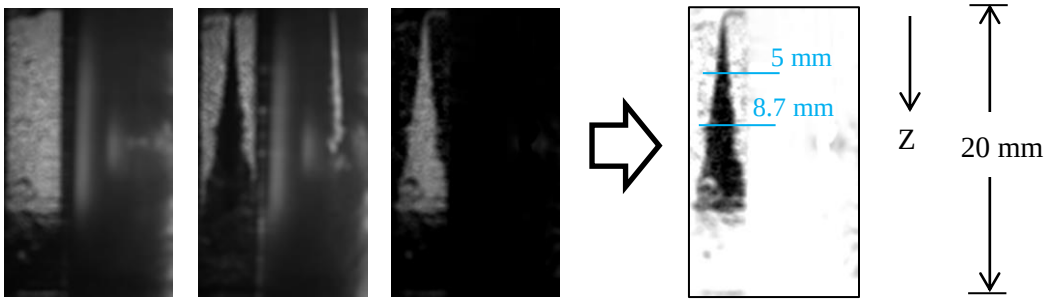

Figure 2.12 Procedures of shadow image subtraction. (a) Background image with circular averaging filter at 0 ms, (b) Spray image with circular averaging filter at 1.3 ms ASOI, (c) Image subtraction of I_0 - $I_{1.3}$, and (d) inverse gray-scale image. Gas condition of 890 K, 46.8 kg/m^3. Nozzle of D=0.180 mm, L=0.5 mm, L/D=2.77.

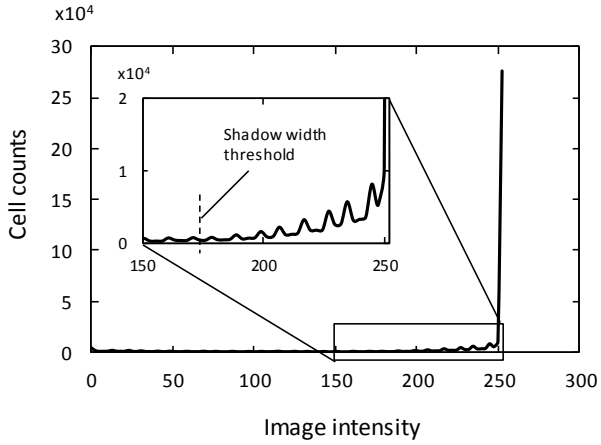

Figure 2.13 Histogram of inverse gray-scale image intensity.

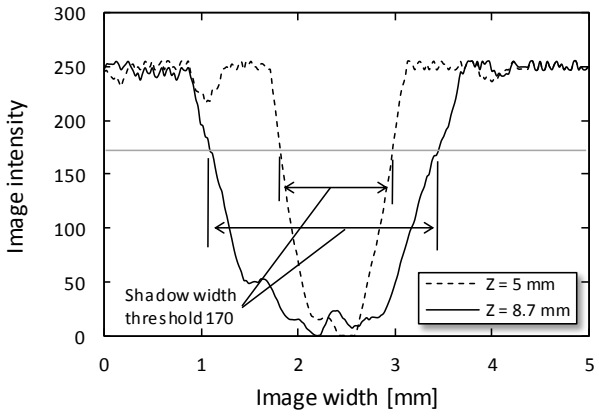

Figure 2.14 Cross-sectional image intensity of the processed shadow image.

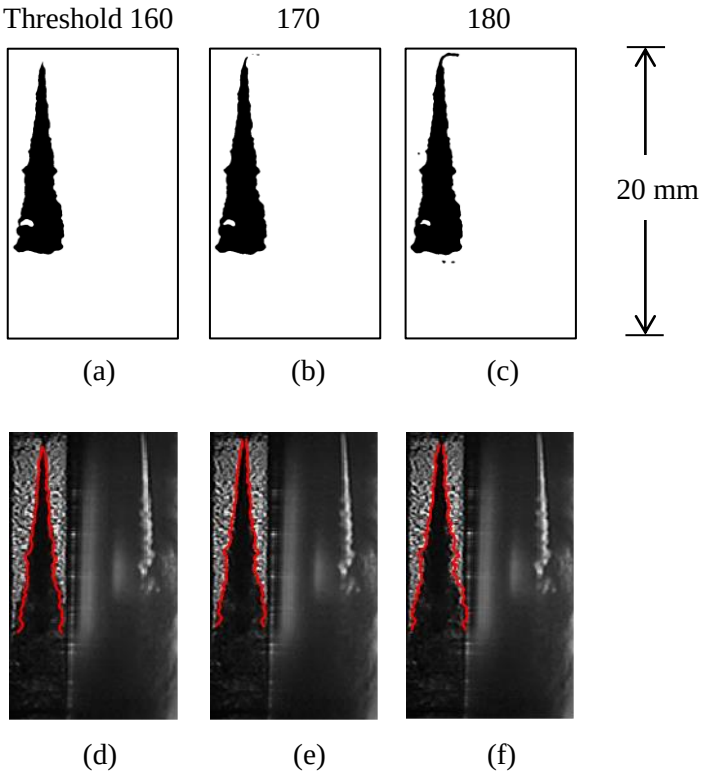

Figure 2.15 Variation of thresholds for vapor fuel boundary at 1.3 ms ASOI. (a-c) Binarized images after thresholding, and (d-f) Detected vapor boundaries superimposed over the raw images.

2.3.3 Cone angles and liquid length

Once the liquid and vapor boundaries are identified, linear regression is used for generating a linear function where starting point is at nozzle tip through downstream. A cone angle composes of two lines marking from the nozzle outlet passing through the averaged values of the detected spray boundary fluctuations. For shadowgraph and scattering cone angle, detection length is confined to be 12 mm for all gas conditions due to the limitation of visualization width that vapor phase is able to spread exceedingly as shown in Figure 2.16a. This is to ensure that all parts of vapor phase spray is strictly located inside the specified detection region. For liquid length LL, there were several cases that the liquid phase penetrated over the visualization region of 20 mm. However, if it exists inside the visualization region, the liquid length is measured to be 9.7 mm in this case shown on scattering image. Figure 2.16b shows the evolution of both cone angles processed every frame from 0-1.5 ms ASOI. The cone angles suddenly expand, once the fuel injects into the high pressure and high temperature chamber. Those fluctuations

remain almost constant at 1.3-1.5 ms ASOI, so that this period is used to for averaging the cone angles and defined as an averaged scattering θ_{sct} and shadowgraph θ_{sha} cone angle.

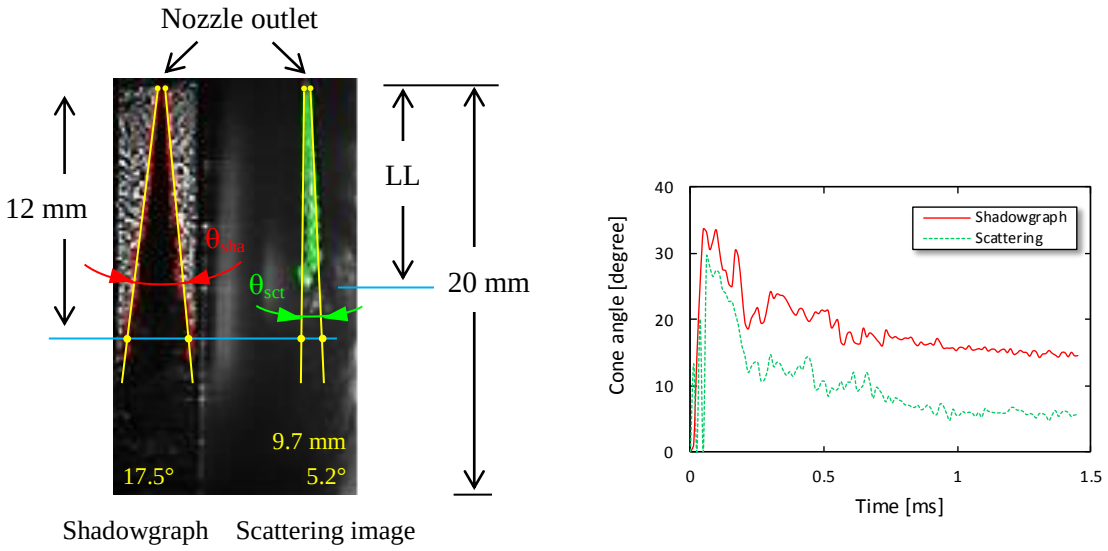

(a) (b)

Figure 2.16 (a) Image processing for vapor and liquid cone angle detection shown in red and green respectively, (b) Evolution of cone angles with time. The LL is the measured liquid length. Gas condition of 890 K, 46.8 kg/m^3. Nozzle of D=0.180 mm, L=0.5 mm, L/D=2.77.

2.3.4 Spray penetration

Techniques to visualize spray penetration and primary combustion indicators for fuel sprays have been well established and standardized methods have been recommended [28-30]. Fuel vapor penetration measurements are used to confirm similar spray and mixing behavior between ambient conditions with the nominally identical injectors [31]. Without quantification, the "boundary" of the spray can be difficult to define as it relates to spreading angle or penetration. Second, the mixing processes in this room temperature experiment may be different than those in the high-temperature, high-pressure in-cylinder engine environment. Droplets in diesel fuel sprays injected into gases at high temperature and pressure will vaporize and create a different physical environment in which mixing occurs. Using high-speed schlieren imaging, Naber and Siebers [7] compared the penetration and spreading angle of evaporating (high-temperature) and non-evaporating (low-temperature) sprays over an extensive range of gas densities, even surpassing that typically experienced in an engine (3-60 kg/m^3). They also found that the penetration rate and spreading angle of an evaporating spray were both lower than that of a non-evaporating spray, which they attributed to vaporization cooling that contracts the spray.

Since the boundary detection on both liquid and vapor phase have previously been demonstrated in subsection, Figure 2.17a shows the processed vapor and liquid boundaries. Figure 2.17b shows the definition of the vapor and liquid penetration which both penetrations are identified by leading edge of the plumes. For each time frame, vapor penetration is longer than liquid penetration because liquid is encountered with vaporization and mixing processes. In addition, liquid penetration remains unchanged starting from 58 μs ASOI when the rate of injection is equals to rate of vaporization. Figure 2.18 shows the measured vapor and liquid penetration at gas condition of 890 K and 46.8 kg/m^3. At the initial stage of 0-50 μs ASOI, the both vapor and liquid phase fuel rapidly penetrates into the high pressure chamber due to high spray momentum. After that vapor penetration is relatively slowdown coinciding with liquid penetration remains constant at almost 9 mm.

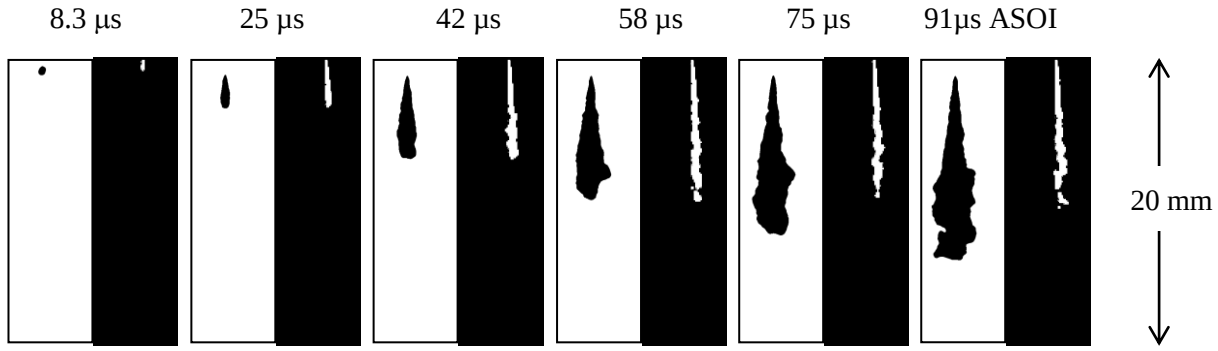

(a) Processed images.

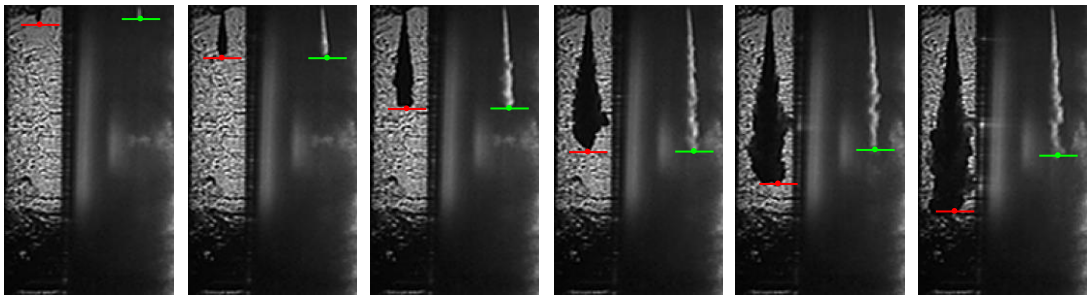

(b) Detected penetrations superimposed over the raw images.

Figure 2.17 Detection of vapor and liquid penetration. Gas condition of 890 K, 46.8 kg/m^3. Nozzle of D=0.180 mm, L=0.5 mm, L/D=2.77.

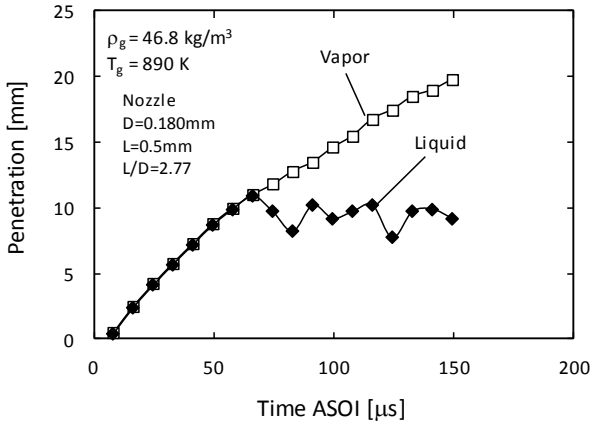

Figure 2.18 Measured vapor and liquid penetration. Gas condition of 890 K, 46.8 kg/m^3. Nozzle of D=0.180 mm, L=0.5 mm, L/D=2.77.

2.4 High Speed Direct Photography of Diesel Flame

The flame luminosity was focused on this photography because it can not only be used to observe the global flame structure and combustion behaviors, but also be viewed as the basic of two-color method. The experimental setup for high-speed flame recording system which combustion flame is driven by rapid compression machine RCM is shown in Figure 2.19.

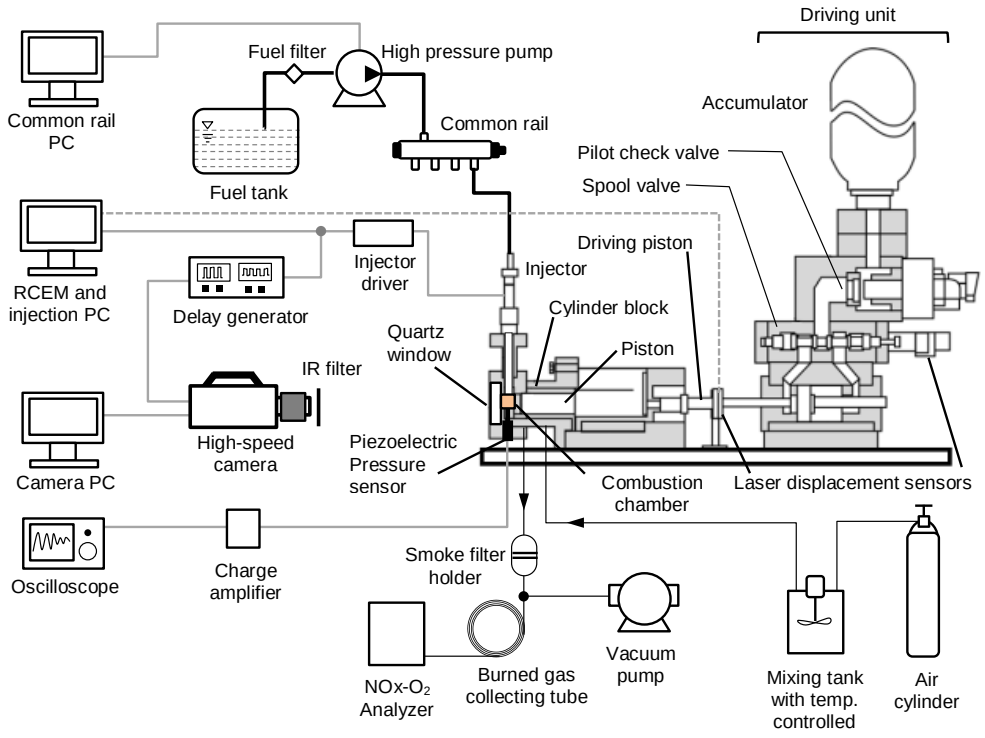

Figure 2.19 Experimental setup for high-speed imaging and emission measurement driven by rapid compression-expansion machine. Device specifications are described in Chapter 4.

2.4.1 Two-Color Pyrometry

Hottel and Broughton developed a two-colour method in 1932 to measure the luminous flame temperature and KL factor [32]. The equations involved in the method were formulated using Wien's law and the emissivity of flames. In their paper, they state that 'The emissivity of a luminous flame ε is numerically equal to its absorptivity based on Kirchhoff's law. Hottel and Broughton measured the spectral transmittance of a row of 12 jet flames and 6 amylacetate (C7H14O2) lamps, and expressed the transmittance using the absorption law given by the right-hand side of Eq. (2.3).

$$\varepsilon = 1 - exp\left(-\frac{KL}{\lambda^{\alpha}}\right) \tag{2.3}$$

where KL is a factor relating to soot concentration and flame thickness L. l is the wavelength in micrometer and a is an index characterizing the effect of wavelength l on emissivity. They obtained $\alpha = 1.39$ in the visible wavelength range from their transmittance measurements of luminous amyl acetate flames.

In 1946, Uyehara et al. first applied a two-colour method to measure the flame temperature and KL factor in an indirect injection diesel engine [33, 34]. In 1980, Matsui et al. showed the effects of engine parameters on flame temperature and the KL factor in a direct injection diesel engine [35].

According to the Wien's equation, the monochromatic emissive power of a black body N(λ,T) depends on the temperature and the specific wavelength, which can be expressed as:

$$N(\lambda, T) = C_1 \lambda^{-5} \exp\left(-\frac{C_2}{\lambda T_a}\right) \tag{2.4}$$

where C_1=3.74177x10^{-16} [W-m^2] and C_2=1.43878x10^{-2} [m-K] are the first Planck's constant and the second Planck's constant respectively; λ is the wavelength and T_a is the temperature of the black body.

Under non-blackbody emission condition, the mission power is expressed as:

$$N(\lambda, T) = \varepsilon_\lambda C_1 \lambda^{-5} \exp\left(-\frac{C_2}{\lambda T_a}\right) \tag{2.5}$$

where T is the temperature of the non-black body; ε_λ is the monochromatic emissivity of a non-black body. Combining Eq. (2.3), Eq. (2.4) and Eq. (2.5) gives

$$KL = -\lambda^\alpha \ln\left[1 - \exp\left(-\frac{C_2}{\lambda}\left(\frac{1}{T_a} - \frac{1}{T}\right)\right)\right] \tag{2.6}$$

If there are two specific wavelengths λ_1 and λ_2 that are measured simultaneously, the value KL which is proportional to the integrated soot concentration can be eliminated:

$$\left[1 - \exp\left(-\frac{C_2}{\lambda_1}\left(\frac{1}{T_{a1}} - \frac{1}{T}\right)\right)\right]^{\lambda_1^\alpha} = \left[1 - \exp\left(-\frac{C_2}{\lambda_2}\left(\frac{1}{T_{a2}} - \frac{1}{T}\right)\right)\right]^{\lambda_2^\alpha} \tag{2.7}$$

Provided the black body temperatures T_{a1} and T_{a2} at two specific wavelength λ_1 and λ_2 can be obtained according to the calibration data, the actual temperature and the KL value calculated.

2.4.2 Blackbody calibration

The relation between flame image intensity and apparent temperature is calibrated using the blackbody furnace as shown in Figure 2.20. The temperature controlled blackbody furnace can be heated to be 2200 K as a maximum. A high speed video color camera is used and the intensity of Red, Green and Blue channels could be obtained for each record. Firstly, at furnace temperature of 1900 K, the camera records six kinds of luminous intensity which are attenuated through six levels of neutral filters placed in front of the camera, then the calibration lines similar to Figure 2.21a is obtained. After that without neutral filter, the blackbody furnace is heated by 50 K increment. In this step, camera records the luminous intensity with blackbody furnace temperature changed and Figure 2.21b can be generated. Three effective wavelengths of color camera could be acquired by the slope and C_2 as λ_{red}=623.47 nm, λ_{green}=542.39 nm, λ_{blue}=488.60 nm. Only the red and green channels are selected for our two-color calculation because these two channels have spectral responses appropriately representing the flame temperature with insignificant flame overlap. From Fig 2.21b, the temperatures of blackbody at two effective wavelengths are received and the actual temperature could be calculated by applying Eq. (2.7). Figure 2.22 shows calculated flame temperature and KL factor analyzed based on two-color method described above.

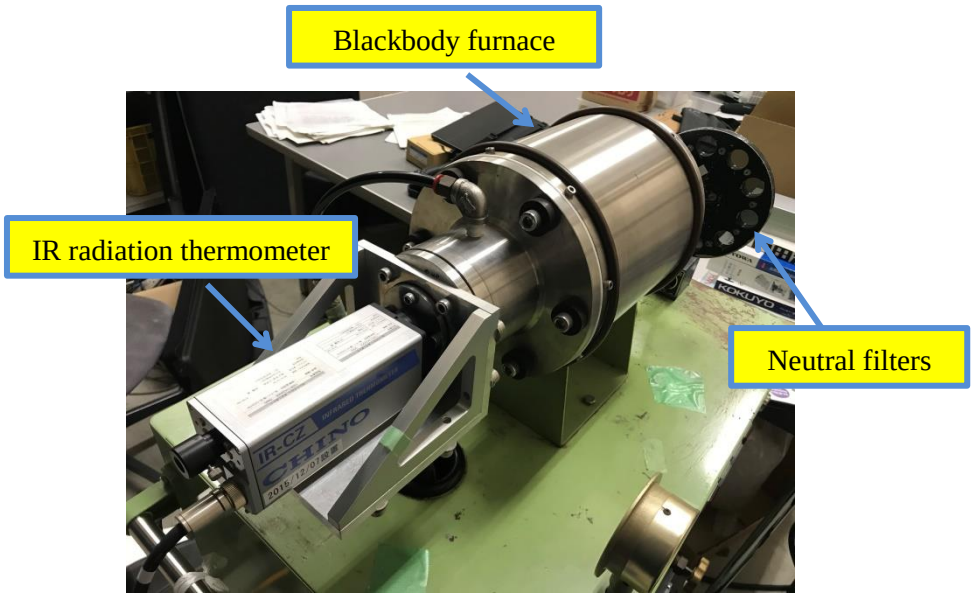

Figure 2.20 Blackbody furnace used for calibration of detector for two-color method.

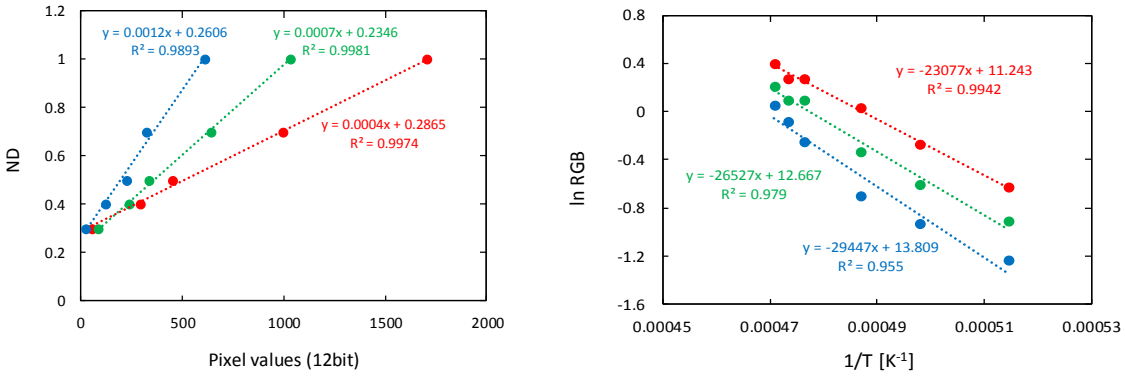

(a) (b)

Figure 2.21 Blackbody calibration curves for two-color method. (a) with neutral filter at T=1900 K and (b) without neutral filter and heated condition of T=1900-2200 K.

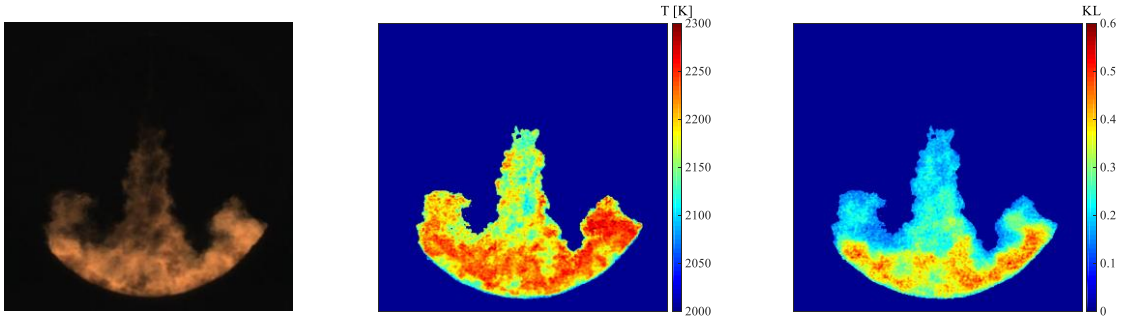

(a) (b) (c)

Figure 2.22 Flame temperature and KL factor analyzed based on two-color method. (a) Luminous flame, (b) Flame temperature, (c) KL factor. Gas condition: 900 K, 12 MPa.

2.5 Conclusions

The imaging techniques used to visualization diesel spray and combustion flame were given. For spray imaging, the simultaneous scattering and shadowgraph imaging technique was used. The scattering technique was verified validity that the light only scatters from liquid portion inside spray. In classical shadowgraph, a shadowgraph of diesel sprays includes both shadows of liquid phase and of vapor phase of fuel. Advantage of using this simultaneous technique is only using a single high-speed camera, spray structure and several characteristics including both liquid and vapor phase data such as liquid length, liquid and vapor cone angles can be detected. In addition, processing of spray photo was described and the effect of the thresholds was also demonstrated in order to achieve appropriate processed photograph. In diesel combustion, the flame luminosity is dominated by soot radiation. In this study, the high-speed direct photography was used for diesel flame imaging. After imaging the combustion flame, the black body calibration and two-color method calculation processes are necessary for flame temperature and KL factor which is related to soot volumetric fraction inside the flame.

Bibliography

[1] Iyer, V. and Abraham, J., “Penetration and Dispersion of Transient Gas Jets and Sprays,” Combust. Sci. Technol. 130(1-6):315-334, 1997.

[2] Pickett, L., Manin, J., Genzale, C., Siebers, D. et al., “Relationship Between Diesel Fuel Spray Vapor Penetration/Dispersion and Local Fuel Mixture Fraction,” SAE Int. J. Engines 4(1):764-799, 2011.

[3] Pastor, J., Payri, R., Garcia-Oliver, J., and Nerva, J., “Schlieren Measurements of the ECN-Spray A Penetration under Inert and Reacting Conditions,” SAE Technical Paper 2012-01-0456, 2012.

[4] Pickett, L., Genzale, C., Bruneaux, G., Malbec, L. et al.,“Comparison of Diesel Spray Combustion in Different High-Temperature, High-Pressure Facilities,” SAE Int. J. Engines 3(2):156-181, 2010.

[5] Montanaro, A., Allocca, L., Johnson, J., Lee, S. et al., “Influence of the Nozzle Geometry of a Diesel Single-Hole Injector on Liquid and Vapor Phase Distributions at Engine-Like Conditions,” SAE Technical Paper 2013-24-0038, 2013.

[6] Edwards, C.F., Siebers, D.L., Hoskin, D.H., “A Study of the Auto Ignition Process of a Diesel Spray via High Speed Visualization,” SAE Paper 920108, 1992.

[7] Naber, J.D. and Siebers, D.L., “Effects of Gas Density and Vaporization on Penetration and Disper-sion of Diesel Sprays,” SAE Paper 960034, 1996.

[8] Wakai, K., Nishida, K., Yoshizaki, T., and Hiroyasu, H., "Ignition Delays of DME and Diesel Fuel Sprays Injected by a D.I. Diesel Injector," SAE Paper 1999-01-3600, 1999.

[9] Ochoterena, R., Larsson, M., Andersson, S., and Denbratt, I., "Optical Studies of Spray Development and Combustion Characterization of Oxygenated and Fischer-Tropsch Fuels," SAE Paper 2008-01-1393, 2008.

[10] Pickett, L., Kook, S., and Williams, T., “Visualization of Diesel Spray Penetration, Cool-Flame, Ignition, High-Temperature Combustion, and Soot Formation Using High-Speed Imaging,”SAE Int. J. Engines 2(1):439-459, 2009.

[11] Parrish, S. E. and Zink, R. J., “Development and Application of an Imaging System to Evaluate Liquid and Vapor Envelopes of Sprays from a Multi-Hole Gasoline Fuel Injector Operating under Engine-Like Conditions,” Atomization Sprays. 22(8):647-661, 2012.

[12] Idicheria, C. and Pickett, L., "Quantitative Mixing Measurements in a Vaporizing Diesel Spray by Rayleigh Imaging," SAE Technical Paper 2007-01-0647, 2007.

[13] Melton L A, Spectrally separated fluorescence for diesel fuel droplets and vapor Appl. Opt. 22 2224–6, 1983.

[14] L.A. Melton, and J.F. Verdieck, 20th Symposium (International) on Combustion, 1283-1290 1984.

[15] A. R. Chraplyvy, “ Non-intrusive Measurements of Vapor Concentrations inside Sprays”, Applied Optics, Vol.20, No.15, pp.2620-2624, 1981.

[16] Suzuki, M., Nishida, K. and Hiroyasu, H., “Simultaneously Concentration Measurement of Vapor and Liquid in an Evaporating Diesel Srapy,” SAE paper 930863, 1993.

[17] Zhang, Y., Yoshizaki, T. and Nishida, K., “Imaging of Droplets and Vapor Distributions in a Diesel Fuel Sr[ay by Means of a Laser Absorption-Scattering Technique,” Applied Optics, Vol.39, No.33, 2000.

[18] Zhang, Y., Nishida, K., and Yoshizaki, T., “Quantitative Measurement of Droplets and Vapor Concentration Distributions in Diesel Sprays by Processing UV and Visible Images”, SAE Technical Paper 2001-01-1294, 2001.

[19] Settles, G.S., Schlieren and Shadowgraph Techniques, Springer-Verlag, 2001.

[20] Pastor, J. V., Garcia, J.M., Pastor, J. M., and Zapata, L. D., "Evaporating Diesel Spray Visualization Using a Double-Pass Shadowgraphy/Schlieren Imaging," SAE Paper 2007-24-0026, 2007.

[21] Pawlowski, A., Kneer, R., Lippert, A., and Parrish, S. E., "Investigation of the Interaction of Sprays From Clustered Orifices Under Ambient Conditions Relevant for Diesel Engines," SAE Paper 2008-01-0928, 2008.

[22] Kunkulagunta, K.R., "Video Imaging and Analysis of Common Rail Sprays in an Optical Engine Using Shadowgraphy Technique," SAE Paper 2000-01-1255, 2000.

[23] Byseveen, M., Almas, T., Ulvund, K. A., Jorgensen, A., and Kvinge, F., "Development of a Shadowgraph Image Technique Describing the Fuel Spray Behavior in a Rapid Compression Machine," SAE Paper 2004-01-2934, 2004.

[24] Kobori, S. and Kamimoto, T., "Development of a Rapid Compression-Expansion Machine Simulating Diesel Combustion," SAE Technical Paper 952514, 1995.

[25] Mark P.B. Musculus and Kyle Kattke, "Entrainment Waves in Diesel Spray," SAE 2009-01-1355, 2009.

[26] R. M. Sullenberger, S. M. Redmond, D. Crompton, A. M. Stolyarov, and W. D. Herzog, "Spatially-resolved individual particle spectroscopy using photothermal modulation of Mie scattering," Opt. Lett. 42, 203-206, 2017.

[27] Espey, C. et al. “Planar laser rayleigh scattering for quantitative vapor-fuel imaging in a diesel jet” Combustion and Flame 109: 65-86, 1997.

[28] N. Maes, M. Meijer, N. Dam, B. Somers, et al. Characterization of Spray A flame structure for parametric variations in ECN constant-volume vessels using chemiluminescence and laser-induced fluorescence Combust. Flame, 174 , pp. 138-151, 2016.

[29] B. Higgins, D. Siebers, Measurement of the Flame Lift-Off Location on DI Diesel Sprays Using OH Chemiluminescence, SAE Technical Paper 2001-01-0918, 2001.

[30] Arai, M., Tabata, M., Hiroyasu, H., and Shimizu, M., "Disintegrating Process and Spray Characterization of Fuel Jet Injected by a Diesel Nozzle," SAE Technical Paper 840275, 1984.

[31] Noud M., Scott A.S., Michele B., et al. Spray penetration, combustion, and soot formation characteristics of the ECN Spray C and Spray D injectors in multiple combustion facilities, Applied Thermal Engineering, ISSN: 1359-4311, Vol: 172, 2020.

[32] Hottel,H.C. and Broughton, F. P. Determination of true temperature and total radiation from luminous gas flames. Ind. Eng. Chem., 4(2), 166–175, 1932.

[33] Uyehara, O. A., Myers, P. S., Watson, K. M., and Wilson, L. A. Flame-temperature measurement in internal-combustion engines. Trans. ASME, January, 17–30, 1946.

[34] Uyehara, O. A., Myers, P. S., Watson, K. M., and Wilson, L. A. Diesel combustion temperatures-the influence of operating variables. Trans. ASME, July, 465–477, 1947.

[35] Matsui, Y., Kamimoto, T., and Matsuoka, S. A study on the application of the two-color method to the measurement of flame temperature and soot concentration in diesel engines. Trans. SAE, 89–3, paper 800970, 3034–3055, 1980.

CHAPTER 3
EFFECT OF NOZZLE SPECIFICATIONS AND SURROUNDING GAS CONDITIONS ON NEAR-FIELD MIXTURE FORMATION

3.1 Introduction

The mixture formation plays a dominant role in diesel engine, because it relates with the combustion efficiency subsequently resulting in fuel consumption and emission. In direct injection diesel engine, the injected fuel is required to distribute properly and complete evaporation within a short time interval in combustion chamber for shortening the time to combustion. An understanding of a spray behavior is a standpoint as one of the most significant challenges for engine design. The current diesel engine employs high boost pressure, high injection pressure and high exhaust gas recirculation (EGR) rates to achieve better output power and meet emission standards. These strategies provide a typical top-dead center (TDC) gas condition before fuel injection exceeding 4 MPa and 800 K [1]. Under the conditions which the surrounding pressure and temperature exceeding the thermodynamic critical point of the injected fuel, fuel jet exhibits remarkable characteristics which are distinctive fashion compared with that at low pressure and temperature according to fundamental thermodynamic analysis [2, 3]. Because of the diminishment of surface tension and enthalpy of vaporization, the sharp distinction between the liquid and gas phases vanishes. The improved microscopic diagnostics [4] was conducted at the near-nozzle field region. They reported above certain pressures and temperatures a dense fluid mixing with diminishing surface tension was observed for n-dodecane sprays after the end of injection (EOI). Several spray visualization techniques have been available for a study of fuel spray physics such as X-ray [5-7], planar laser-induced exciplex fluorescence (PLIEF) [8], phase doppler interferometry (PDI) [9] and high-speed shadowgraph imaging [10]. To determine the liquid phase in the spray, Mie scattering is a preferable imaging technique to visualize the liquid portion in the fuel jet [11]. There have been few publications presenting flow characteristics from different nozzle hole lengths [12, 13]. The computational fluid dynamics (CFD) simulations for different nozzle configurations were performed and described the flow behaviors inside the nozzles [14]. From the literature reviewed in spray diagnostics, it has been limited research works conducted the simultaneously imaging for vapor and liquid phase fuel spray particularly focusing on near nozzle region. The objective of the present work is to investigate the effect of nozzle hole length to diameter ratio under wide ranges of surrounding gas condition. The experiment employs an optical microscopy technique to capture liquid and vapor phase information in near-field region.

3.2 Numerical Simulation for Cavitation in Nozzle Hole

Cavitation in a fuel injector nozzle can be defined as the phase transition of liquid into vapor due to sudden local pressure drop. At the entrance of nozzle, there is a strong change in cross-section and flow direction due to present of sharp edges. Addition to this, the boundary layer tends to separate from the hole wall and the vena contracta is formed. As a consequence, a recirculation zone appears between the vena contracta and the orifice wall. There is a pressure fluctuation in this region due to the acceleration of the fluid. During the pressure depression, if the static pressure falls below the vaporization pressure, the cavitation will be appeared. More specifically, to start the cavitation in this region, presence of nuclei which is called as small bubbles and their diameters change around 10^{-6} μm are needed. If the small bubbles enter into the low pressure region, they start to grow up and lead to cavitation. Cavitation inside a fuel injector nozzle tends to enhance the jet turbulence which leads to increase the spray angle and to promote the fuel atomization of the diesel engine. When the injection pressure is low, the cavitation only appears at the entrance of the nozzle. With an increase of injection pressure cavitation inside nozzle starts to develop and extend throughout nozzle exit. As a result, cavitation alters the velocity profile and turbulence level inside nozzle, and directly affects the primary break-up and subsequent atomization of fuel. Finally, the enhanced atomization also results in better combustion process, which in turn will decrease the fuel consumption and reduce the released harmful exhaust gases and particulate emissions. Addition to benefits of the cavitation inside fuel injector nozzle, it should be mentioned about the disadvantages that can be seen in the multi-hole nozzle as a severe erosion problem. In some cases, the erosion problem can lead to disastrous results. Therefore, significant damages and erosion can be seen on the provided most of modern nozzles, which are particularly used with high pressure common-rail systems after operating few hundred hours of operation [24]. In order to better understand the effects of cavitation inside injector nozzle, a large variety of experimental works have been performed using large-scale transparent nozzles [25–30], which enable to facilitate visualization of cavitation structure. Although, there are some experimental works using real size of injector nozzle [31–34], it should be noted that performing experiment with an actual nozzle is very difficult due to refraction of light at cylindrical side wall of the nozzle and complexity of the transient cavitating flow.

These drawbacks make the experimental visualization and measurements extremely difficult in an actual nozzle, and also create a big difficulty to execute the experimental work at exactly same operating conditions and geometry. Therefore, lots of numerical models have been developed for many years to predict and simulate the cavitation in injector nozzles [35-43]. The huge density and viscosity differences between liquid and gas phases make the numerical simulations difficult. That is why the experimental and numerical works of the turbulent

cavitating flow inside fuel injector nozzle and its influence on spray atomization are still an on-going and prominent research topic.

3.2.1 Numerical Setup

Understanding the cavitation flow in a nozzle of fuel injector for diesel engines has major importance, since it plays a significant role in the fuel spray atomization and strongly affects diesel engine performance and emissions. Because of the experimental difficulties connected with flow measurements and visualization inside actual size of injector nozzle, Computational Fluid Dynamics (CFD) simulations stand for an important tool to predict and model the cavitation inside injector nozzle with the development of high performance computers. Therefore, CFD works becomes in great demand topic compared to experimental studies due to being easy, low work-time and low-cost. The main objective of the present work is to develop an effective combination of numerical models, which is able to simulate the cavitation in high pressure difference between injection and chamber pressure with changing the nozzle hole lengths and orifice diameters.

The present study is carried out using the open-source OpenFOAM which is based on object-oriented programming, free open source CFD tool [44]. The simulation is based on currently available unsteady cavitation solver called cavitatingFoam . The cavitatingFoam solver is a transient cavitation solver that employs the HEFM approach to capture phase-change in isothermal, compressible cavitating flows. The main assumptions in the cavitatingFoam solver are as follows [45-47]. Figure 3.1 shows the computational mesh with boundary conditions assigned. To compromise computational time, the 90-degree sector is prepared for computational fluid domain. In order to consider the effect of flow behavior and vortex generated inside the sac volume, fixed needle left at 0.05 mm is decided. The fuel enters the domain at the inlet surface of the sac which is assigned to be 150 MPa as injection pressure used in the experiment while the total pressure of 6 MPa is assigned to the end of the chamber which is equal to the ambient pressure as shown in Figure 3.1a. Two surfaces for cyclic patches show in Figure 3.1b. At the nozzle hole, the flow drastically increases due to small orifice. To resolve physical phenomena occurred during the entrance and inside the hole, mesh size should be determined appropriately.

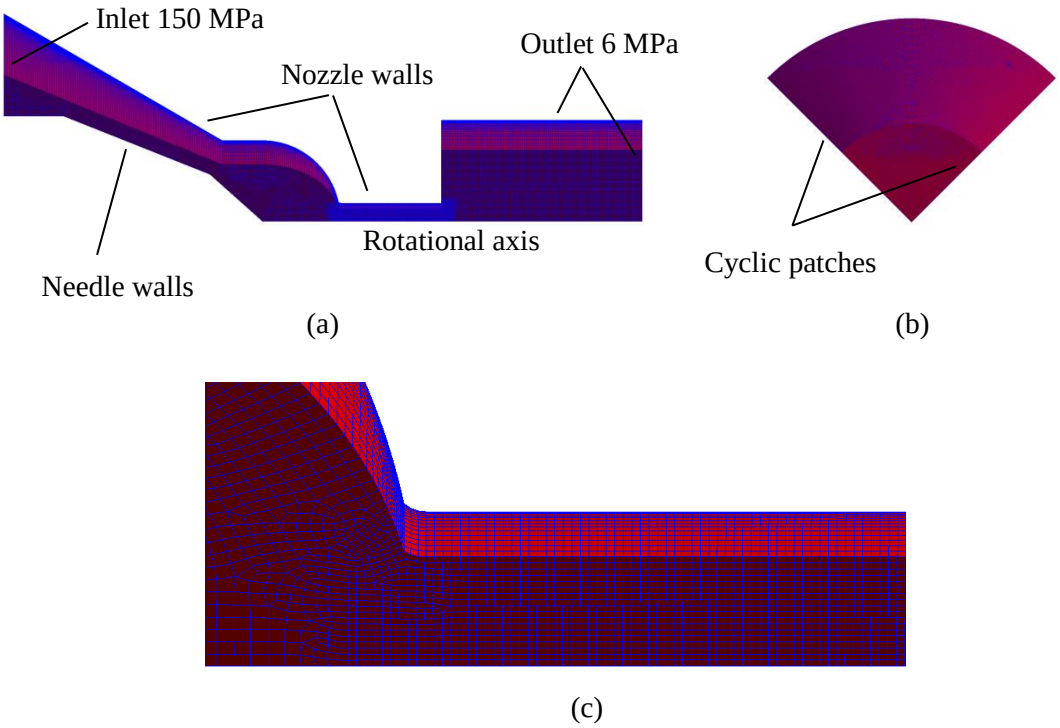

Figure 3.1 Computational mesh with fixed needle lift. (a) boundary conditions, (b) 90-degree sector with cyclic patches, and (c) close up of 5-μm mesh size at nozzle hole.

3.2.2 Mesh Independence Study

In order to take into account the significance of in-nozzle generated turbulence on primary atomization, the size of the cells in the nozzle for the fine resolution case was decreased. Table 3.1 shows the computation parameters to be varied such as refinement at sac volume, injector hole volume, and the chamber volume. Six meshes are created from very coarse to fine by decreasing the element size by a factor of about two between each consecutive. The averaged total pressure and mean velocity at nozzle exit are calculated for all meshes at time after start of simulation ASOS of 0.8 ms and the result is shown in Figure 3.2.

As usual, grids are compared by evaluating the mean velocity in the fluid domain and the pressure drops across the orifice at nozzle exit. The results show that the difference between the 0.84×10^6 element grid and the $2.18\text{x}10^6$ element grid is less than 3% for mean velocity and 5% for the pressure differences. For this reason, the 0.84×10^6 grid is selected for further computations.

Table 3.1 Mesh independence study.

Case	Averaged mesh size (μm)			Cell count
	Sac	Hole	Chamber	
Very coarse	20	10	10	$0.27x10^6$
Coarse-a	14	7	10	$0.34x10^6$
Coarse-b	10	7	10	$0.52x10^6$
Medium-a	10	5	10	$0.84x10^6$
Medium-b	5	5	10	$2.18x10^6$
Fine	2	2	5	$8.53x10^6$

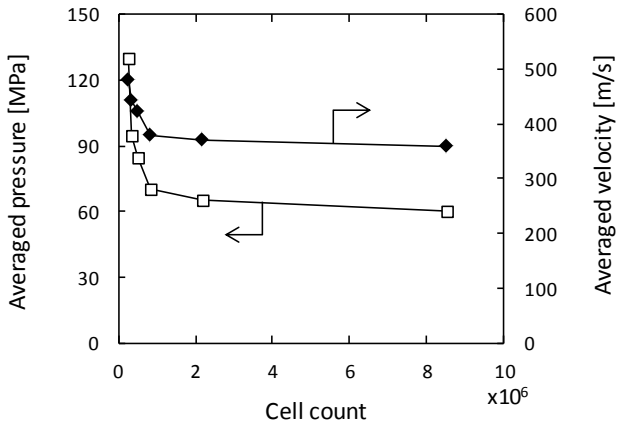

Figure 3.2 Comparison of averaged pressure and averaged velocity for different mesh resolutions calculated on a cross-sectional plane at the nozzle hole exit, the sac inlet pressure of 150 MPa and the chamber outlet pressure 6 MPa.

Figure 3.3 shows the calculation time that is required for different mesh setup. The problem is solved by the computer workstation equipped with CPU E5-2699v3@2.30GHZ, 18 logical processors and 256 GB of memory. Time step is controlled to be $1e^{-8}$ s and the calculation is executed until 0.8 ms for simulation time. For very coarse mesh, the calculation takes 12 hrs to complete while 95 hrs is required for fine mesh. As in previous decision, the Medium-a case was confirmed mesh indecency, the calculation needs 39 hrs to complete which can reduce the computational time by 3 times compared with that of fine mesh and receive the same results.

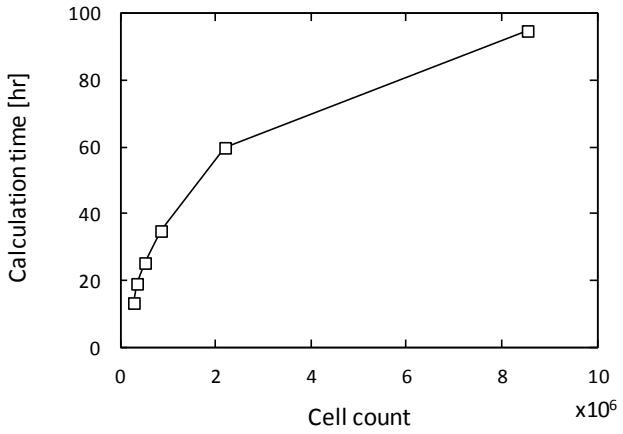

Figure 3.3 Variation of computational speeds with number of cells.

3.2.3 Effect of Nozzle Specifications on Cavitation

In general, when fluid flows through the small orifice, it is accelerated and the pressure drops suddenly. For this reason, cavitation is possible to be generated inside the nozzle hole when the static pressure drops under the vapor pressure. Figure 3.4 shows the vapor volume fraction for different nozzle specifications that are identical uses in the experiment described in Chapter 3 and 4. The vapor phase is generated near the entrance and moves downstream. At 0.6 ms ASOS for all nozzle specifications, vapor phase behavior is found to be steady. For nozzle orifice size of D=0.180 mm, L=0.5 mm, vapor phase reaches the nozzle exit while the longer hole length nozzle of D=0.180 mm, L=0.8 mm, vapor phase emerges inside the nozzle hole with low concentration found at the nozzle exit. From this result, breakup length is expected to be shorter for the shorter hole length nozzle of D=0.180 mm, L=0.5 mm compared with that of the longer one. This is because once jet leaves the nozzle exit, it encounters with high drag force generated by the ambient pressure. It could also enhance collapse of the bubbles which eventually leads to promotion of breakup process. In addition, fuel mass flow rate that generated by the shorter hole length nozzle is also expected to be lower than that of the longer one due to the cavitation partially filled the hole leading to prevention of the flow.

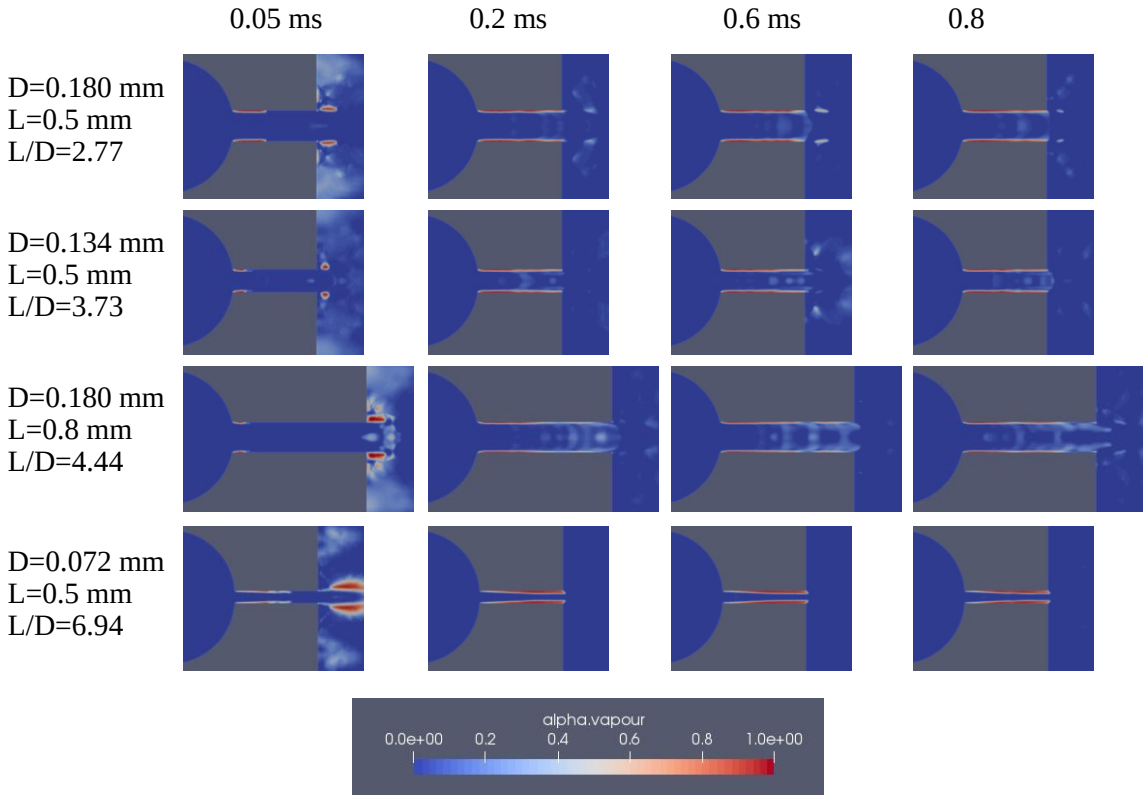

Figure 3.4 Vapor volume fraction for different nozzle specifications at four Instantaneous time after start of simulation ASOS.

3.2.4 Predicted Mass Flow Rate and Discharge Coefficient

The mass flow rate across the entire cross-sectional area of the nozzle hole can be calculated by integrating the stream wise velocity and density profiles over the cross-sectional surface area at nozzle exit as shown in Figure 3.5.

$$\dot{m} = \int_0^{2\pi} \int_0^R \rho_z(r) u_z(r) r dr d\theta \tag{3.1}$$

where $\dot{m}$ is the mass flow rate, rho is the liquid density, u_z is the streamwise velocity profile, r is the radial coordinate, R is the radius of orifice and θ is the angle in radian.

$$u_{max} = \sqrt{\frac{2 \cdot (P_{inj} - P_b)}{\rho_f}} \tag{3.2}$$

$$C_d = \frac{\dot{m}}{\dot{m}_{th}} = \frac{\dot{m}}{\rho_f u_{max} A} \tag{3.3}$$

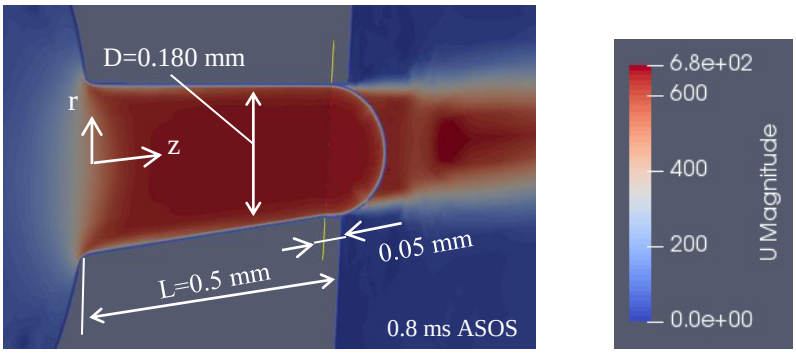

D=0.180 mm, L=0.5 mm, L/D=2.77

Figure 3.5 Velocity distribution and cross-sectional plane created at nozzle exit for calculated mass flow rate and velocity components. Computation at inlet of 150 MPa and outlet 6 MPa.

The calculation is terminated at 1 ms time after start of simulation ASOS. It has already been confirmed that the flow reaches steady condition. Calculation of mass flow rate requires density and velocity gradients generated from CFD in z-direction as integral description is shown in Eq. (3.1). Discharge coefficient can then be obtained by combination of Eq. (3.1) and (3.2). The comparison of mass flow rate across the nozzle and calculated discharge coefficient between the experiment and calculation based on CFD is shown in Figure 3.6. Mass flow rate measured by Zeuch's method is found to be higher than that of the calculation one except nozzle of D=0.134 mm, L=0.5 mm. This is implied that the cavitation calculated by CFD is over generated that prevent the flow. The reason for this discrepancy is also due to the simple of cavitation model that could not resolve complex phenomena such as cavitation deformed and collapsed. For smallest nozzle orifice size of D=0.072 mm, L=0.5 mm, large amount of cavitation is generated.

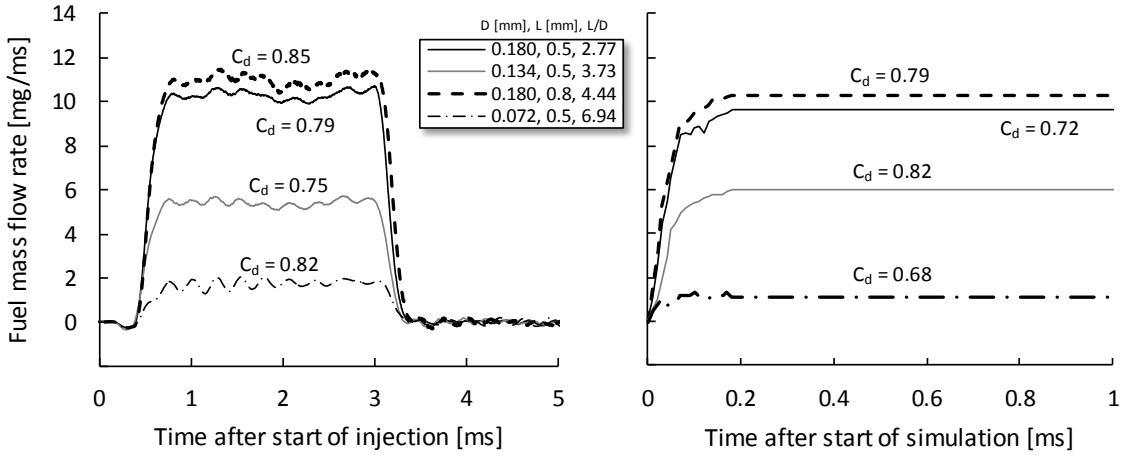

(a) (b)

Figure 3.6 Comparison of mass flow rate for different nozzle specifications. (a) experiment by Zeuch's method and (b) computation.

3.2.5 Velocity Profiles at Nozzle Exit

In this study, it was hypothesized that the different in nozzle orifice and nozzle hole length would generate different internal flow behavior. The cavitation generated inside the nozzle hole was illustrated and discussed previously. The resulting cavitation would affect other flow characteristics such as axial and radial velocity profiles. Velocity magnitude is shown in Figure 3.7. For all nozzle specifications, the maximum velocity is found to locate at the center of nozzle hole which is almost 680 m/s, because they are all the same inlet and outlet pressures that drives the flow. The smooth velocity gradient can be observed for the nozzle that containing large amount of cavitation such as D=0.180 mm, L=0.5 mm including smaller orifice size nozzles of D=0.134 mm and D=0.072 mm. This is because the cavitation prevents the flow at the area near the nozzle wall. Figure 3.8 shows the axial velocity profile measured at nozzle exit. Comparing between identical orifice size nozzle of D=0.180 mm, the shorter hole length nozzle gives a smoother velocity profile near the wall. Figure 3.9 shows the radial velocity profile which describes the velocity in r-direction. There are some differences in peak and profile shape. It is said that cavitation inside the nozzle tends to slowdown the flow in both axial and radial direction where cavitation existing.

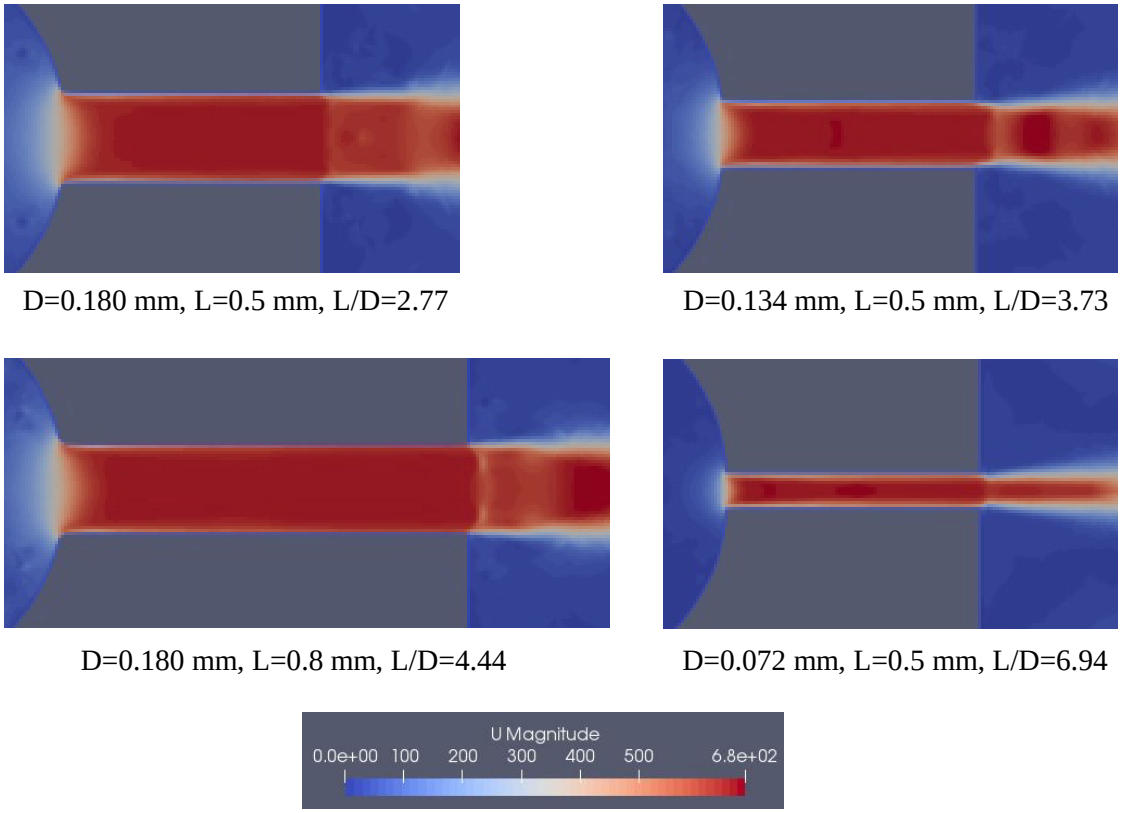

Figure 3.7 Velocity magnitude for different nozzle specifications at 0.8 time after start of simulation.

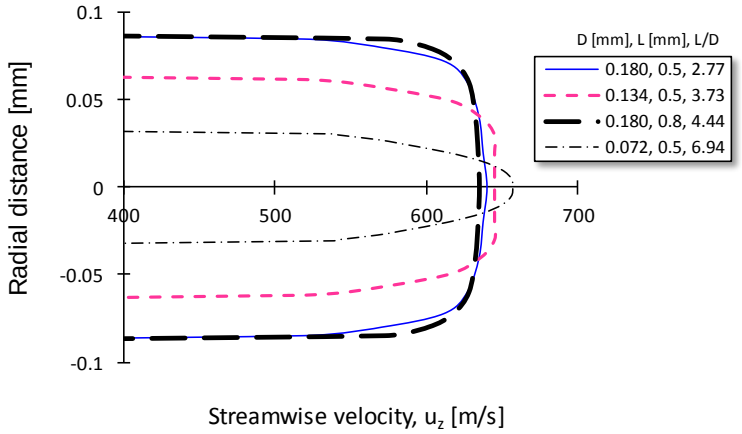

Figure 3.8 Axial velocity profile (u_z) at nozzle exit for different nozzle specifications.

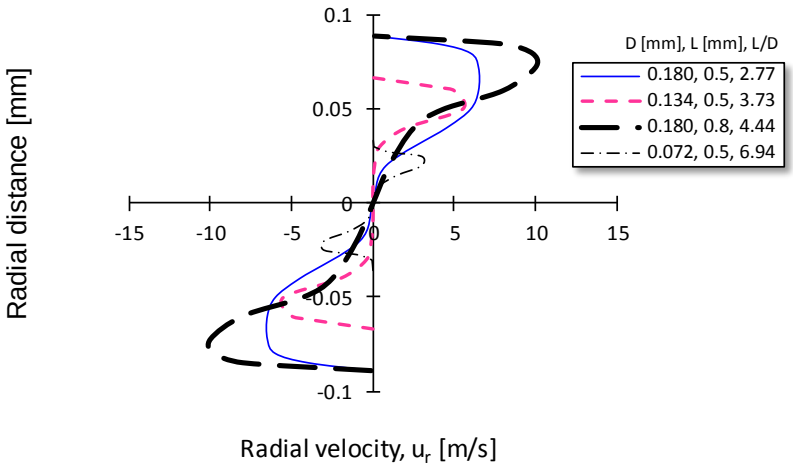

Figure 3.9 Radial velocity profile (u_r) at nozzle exit for different nozzle specifications.

3.3 Experimental Setup

In this study, it is intended to separately image both vapor and liquid phases of fuel spray in order to observe spray structure and vaporization characteristics of injected fuel when emerges into large variation of gas condition. The light scattering imaging technique is properly selected as an indicator of liquid phase and high density spray. The scattering technique employed in this study was verified validity whether light scatters only from liquid or includes gas phase. The Rayleigh scattering [15] describes the scattering from the gas phase and molecules, while Mie scattering [16] accounts for scattering from liquid fuel droplets. In calculation, a simple one-dimensional jet model [17] was employed to estimate mixture fraction and number density of gas phase. The Rayleigh scattering cross section of diesel fuel in gas phase was obtained from [15] and the approximated diesel droplet diameter of 20 μm was used for liquid phase. As a result, averaged intensity difference between Rayleigh and Mie scattering regimes showed as entirely different as in order of 14-15 for wide range of surrounding gas conditions of 4-6 MPa and 500-900 K for pressure and temperature respectively. Therefore, the large difference between those scattering regimes is fairly reasonable for the scattering imaging technique used for quantification of liquid portion inside spray. In classical shadowgraph, a shadowgraph of diesel sprays includes both shadows of liquid phase and of vapor phase fuel. The desired surrounding gas conditions conducted in this work were prepared by rapid compression-expansion machine (RCEM) [18]. The compression chamber and optical accessible arrangement are schematically shown in Figure 3.10. In this experiment, 0-20 mm from nozzle tip towards downstream spray was taken by means of simultaneous classical shadowgraph and scattering imaging technique. The detail of optical setup was previously

shown in Chapter 2. In Table 3.2, the stroke of the RCEM was 150.5 mm with the compression ratio of 12.1. Four single-hole type nozzles with variation of L/D ratios were used for experiment. The injection pressure was kept at one pressure of 150 MPa and fuel inlet temperature was about 310 K. Due to small bore of 30 mm of compression chamber, injection duration was decided to be 1.5 ms to avoid impingement until imaging ended of injection state. Fuel properties consisted of three compositions with critical point of 1.67 MPa and 677 K for critical pressure and temperature respectively. The nitrogen gas was supplied as surrounding gas to suppress combustion.

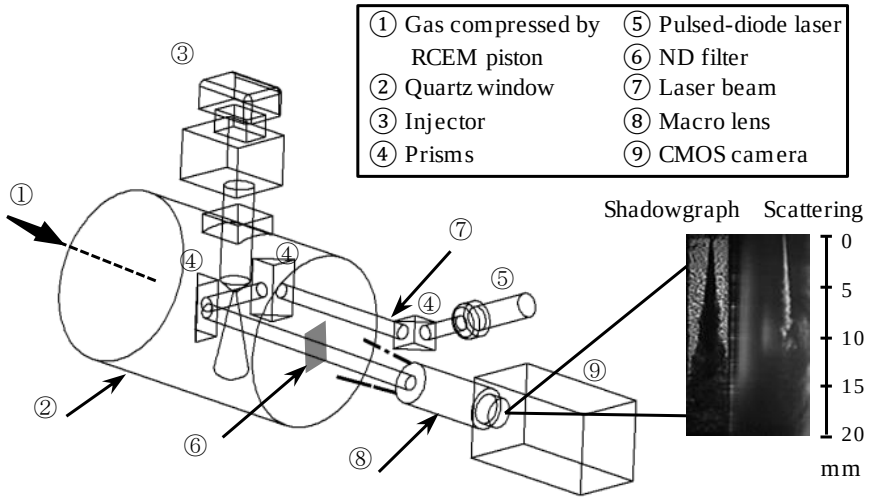

Figure 3.10 Optical arrangements for simultaneously shadowgraph and scattering imaging.

Table 3.2 Experimental conditions in RCEM.

RCEM and Chamber specifications	
Piston speed	30 ms/comp. (~1200 rpm)
Bore x Stroke	30 x 150.5 mm
Displacement	425.32 cc
Compression ratio	12.1
Injection conditions	
Nozzle hole number	1 (all nozzles)
Orifice diameter D Nozzle hole length L (L/D)	0.180 mm, 0.5 mm, (2.77)
	0.134 mm, 0.5 mm, (3.73)
	0.180 mm, 0.8 mm, (4.44)
	0.072 mm, 0.5 mm, (6.94)
Fuel temperature	310 K (± 10 K)
Injection pressure	150 MPa
Injection duration	1.5 ms
Fuel properties	
n-paraffins % mass	$C_{12}H_{26}$: 11.6% $C_{13}H_{28}$: 62.6% $C_{14}H_{30}$: 25.7%
Critical pressure	1.67 MPa
Critical temperature	677 K
Density at 300 K	745.3 kg/m^3
Surface tension at 300 K	20.8 mN/m
Surrounding conditions	
Gas	Nitrogen
Pressure (P_g)	1.8 – 12.4 MPa
Temperature (T_g)	534 – 890 K
Density (ρ_g)	7 – 46.8 kg/m^3

For the surrounding gas condition relevant to current diesel spray, gas pressure and temperature at top dead center TDC exceed 4 MPa and 800 K [1] respectively. Therefore, the experimental condition is determined to perform from surrounding gas conditions below the critical point of the used fuel through the supercritical region for wide range study of gas condition on spray structure and spray characteristics. In this experiment, the nitrogen gas was

used as a surrounding gas. In Figure 3.11, the operating gas conditions are plotted on the pressure versus temperature space with the critical point of the fuel included. The 17 conditions plotted are the total of prepared surrounding gas conditions at TDC before fuel injection. The gas pressure was measured by in-cylinder pressure sensor while the gas temperature took advantage of the adiabatic compression process. A wide range of surrounding circumstances is set ranging from 1.8-12.4 MPa and 534-890 K for gas pressure and temperature respectively. The gas conditions indicating in the P-T map are determined from the variation of study aspects which contains 3 classifications. The first one is three constant gas temperatures of 534 K, 712 K and 890 K. The second is three constant gas pressures of 1.86 MPa, 3.71 MPa and 7.44 MPa. The final is four constant gas densities of 11.7 kg/m^3, 23.4 kg/m^3, 35.2 kg/m^3 and 46.8 kg/m^3.

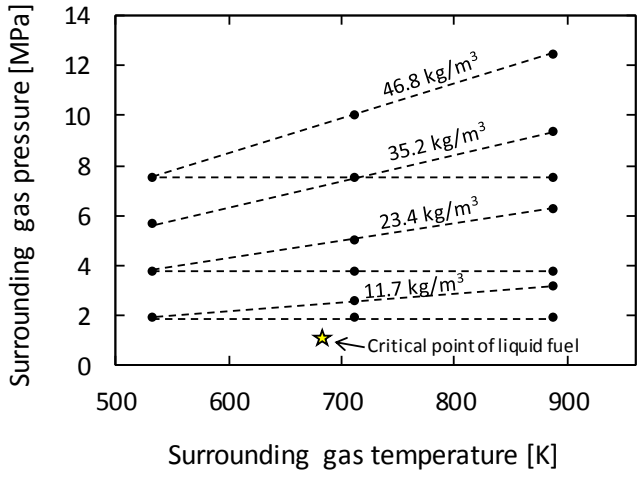

Figure 3.11 P-T diagram representing surrounding gas conditions including critical point of the fuel. The dashed lines indicate constant gas density and constant gas pressure conditions.

3.4 One Dimensional Spray Model and Fuel/Air Mixture Fraction

In diesel combustion, the mixture preparation of fuel and surrounding gas is of primary importance to control combustion and emissions. For direct-injection engine, an atomized liquid spray evolves into a vaporized fuel jet as it penetrates into the combustion chamber. This study employs the Musculus's model with given our measured data such as liquid cone angle θ_{sct}, vapor cone angle θ_{sha} and liquid length LL. This is for estimation of fraction of liquid fuel, vapor fuel and entrained gas in the near-nozzle spray region. Musculus and Kattke have developed the non-evaporating 1D diesel spray model which approach is based on entrainment wave concept [17]. The calculation was assumed that mixture distribution in evaporating spray is

the same with that in non-evaporating spray. Additionally, the profile of velocity and fuel volume fraction in a cross section is given. The model used a one-dimensional numerical control-volume solution, discretized along the spray axis and assumed no velocity slip between injected fuel and entrained gases. Using Musculus's model, the predicted penetration and mixture distribution were precisely compared to Rayleigh-scattering mixing experiment with acceptable discrepancies [23]. In Figure 3.12, the fuel liquid volume fraction $\bar{x}_f$ is predictable in all locations of specified spray area. The overbar signifies turbulent mean value. The subscript c denotes the value on the jet centerline. The non-dimensional radial coordinate ξ = r/R is the ratio of the radial coordinate r to the jet width R. Regarding the liquid-fuel radial profile, the fully developed profile for vapor-fuel fraction which is approximately Gaussian with α=1.5. In Figure 3.12, there are basically two regions which are the liquid region and the vapor region. The liquid region identifies liquid fuel portion that refers to the scattering image in this experiment. On the other hand, vapor region comprises of both vapor fuel and entrained gas. The calculation requires such as cone angles measured from shadowgraph and scattering images, nozzle specifications, injection pressure and gas conditions as input parameters. The estimated fuel volume fraction $\bar{x}_f$ obtained from the Musculus's model is then used for estimation of liquid fuel mass m_{flq}, vapor fuel mass m_{fvp}, and entrained gas mass m_{N2} using Eq. (1-3) respectively.

$$m_{flq} = \int_0^{LL} \int_0^{2\pi} \int_0^{r_{sct}} \rho_{f,lq} \bar{x}_f(r,z) r dr d\theta dz \tag{3.4}$$

The fuel mass in vapor phase $m_{f,vp}$ is calculated by

$$m_{fvp} = \int_0^{VL} \int_0^{2\pi} \int_{r_{sct}}^{r_{sha}} \rho_{f,lq} \bar{x}_f(r,z) r dr d\theta dz \tag{3.5}$$

The entrained gas amount m_{N2} is as follows

$$m_{N2} = \int_0^{VL} \int_0^{2\pi} \int_0^{r_{sha}} \rho_{N2} \{1 - \bar{x}_f(r,z)\} r dr d\theta dz \tag{3.6}$$

where ρ_f and ρ_{N2} are the fuel and surrounding densities respectivley. The $r_{sct}$and r_{sha} are the radius of spray in scattering image and in shadrowgraph respectively. The LL is the liquid length and VL is the visualization region. It is noted that if the liquid fuel penetrates over 20 mm of visualization region, the liquid length is set to be 20 mm in calculation. The liquid

fuel mass is obtained from the liquid fuel density ρ_{flq} and fuel volume fraction $\bar{x}_f$ integrated over the liquid scattering region as expressed in Eq. (3.4). The calculation of vapor fuel mass is carried out in the region that liquid scattering region subtracted from the vapor shadowgraph region as expressed in Eq. (3.5). In Eq. (3.6), the entrained gas mass is calculated in whole spray zone including liquid scattering zone. The calculation needs surrounding gas density ρ_{N2} and entrained gas volume fraction $1 - \bar{x}_f$. In experiment, the fuel in vapor phase continuously penetrated through the capture area which is over 20 mm measured from nozzle tip. It should be noted that the integration in streamwise direction dz for vapor fuel and entrained gas are restrictively considered with VL=20 mm.

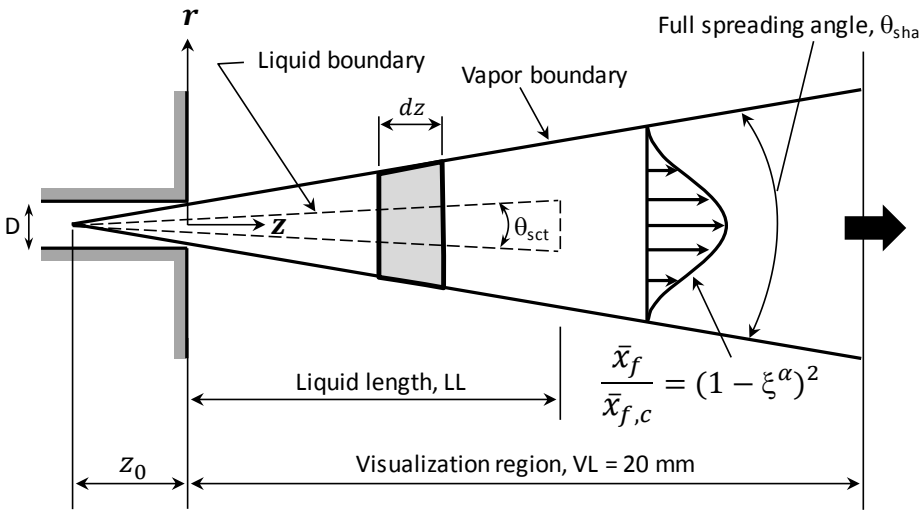

Figure 3.12 Quantification of mixture fraction based on diesel jet with momentum flux transport developed by Musculus [17]. The liquid length LL, visualization region VL, scattering θ_{sct} and shadowgraph θ_{sha} cone angles are specified.

3.5 Results and Discussions

This section consists of five subsections. It begins with fuel injection rate at four different nozzle specifications. The second subsection shows the raw images obtained from the experiment with selected gas densities at gas temperature of 890 K. Then, the measured liquid length and measured cone angles are presented in the third and fourth subsection respectively. The last section is the estimation of mixture quantities based on measured data incorporated with one-dimensional jet model.

3.5.1 Rate of Fuel Injection

The rate of fuel injection is the rate of the fuel introduction into the combustion chamber. It is the consequence to spray evolution, fuel atomization and mixing with surrounding gas which are used to determine the combustion development. Therefore, it is important to understand injection behavior for each nozzle before pursuing the spray experiment. In this study, the injection rate measurement was based on the method proposed by Zeuch [19, 20], according to which the injection is actuated in a closed, fixed-volume chamber filled with the same injected fluid. The single-hole type solenoid injectors of four varying nozzle hole length to diameter ratio L/D were used for the test. In the measuring chamber, the injection pressure was also kept at constant of 150 MPa. Figure 3.13 shows measured injection rate profile which was activated by 2.2-ms injection signal. Additionally, the discharge coefficient Cd calculated from rate of fuel injection for each nozzle is provided. Injection profile with almost rectangular shape is observed. The initial rise of injection rate for all nozzle specifications is about 0.4 ms and injection almost ends at 3.3 ms from the start of injection. The different nozzle specifications clearly show the different averaged rate of fuel injection. It is carefully noted that the rate of fuel injection is not ranged in order, for example D=0.180 mm (L/D=4.44) achieves both the highest averaged rate of fuel injection of 10.8 mg/ms and the highest discharge coefficient of 0.85. However, the nozzle is not the largest L/D ratio. In Figure 3.13, the result of fuel injection rate test can be divided into three groups which is high rate of fuel injection for D=0.180 mm (L/D=4.44) and D=0.180 mm (L/D=2.77) while middle rate of fuel injection is D=0.134 mm (L/D=3.73). The lowest rate of fuel injection is found to be D=0.072 mm (L/D=6.94). It is noted that the nozzle L/D ratio of 2.77 and 4.44 come with identical orifice diameter of 0.180 mm. Comparing between D=0.180 mm (L/D=4.44) and D=0.180 mm (L/D=2.77) which are identical nozzle orifice size, the longer nozzle hole length provides the higher rate of fuel injection. It suggests that if the same fuel properties and same injection pressure are considered, the nozzle that comes with longer nozzle hole length would supply higher amount of fuel.

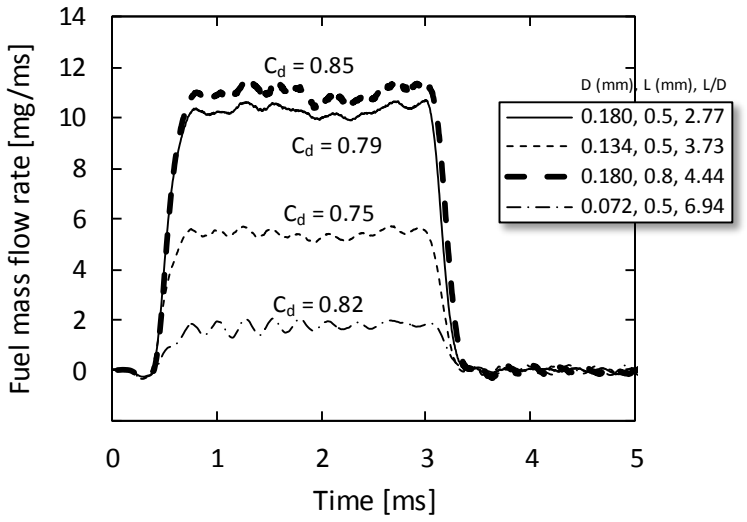

Figure 3.13 Comparison of measured rate of fuel injection using Zeuch's method. The legend presents four nozzle specifications used for injection test.

3.5.2 Near-Field Fuel Spray

Figure 3.14 displays instantaneous photographs directly captured from the experiment at gas temperature of 890 K. The images are tabulated vertically for different nozzle hole length to diameter ratio L/D of 2.77, 3.73, 4.44 and 6.94 from left to right respectively. The rows are arranged for different gas density of 46.8 kg/m^3, 23.4 kg/m^3 and 11.7 kg/m^3 from top to bottom respectively. The liquid length LL can be measured from the scattering image. However, not all gas conditions could be done, due to limitation of capturing length of 20 mm. In the scattering image, variation of light intensity is observed and it is essentially stronger at the spray centerline region. There are some variations of liquid phase cone angle incorporated with scattering intensity among gas conditions and nozzle specifications. The shortest liquid length is detected at D=0.072 mm (L/D=6.94) at gas density of 46.8 kg/m^3. This is as expected because this nozzle specifications provides the lowest rate of fuel injection in Figure 3.13 resulting in the lowest spray momentum even more when interacts with surrounding gas. In addition, the small orifice diameter tends to promote breakup process leading to smaller droplet size. Both influences could contribute to improved liquid vaporization. Increasing the orifice diameter results in slowdown liquid vaporization as reported in D=0.180 mm (L/D=2.77), D=0.134 mm (L/D=3.73) and D=0.180 mm (L/D=4.44) at gas density of 46.8 kg/m^3. The shorter liquid length and wider scattering cone angle are observed at D=0.180 mm (L/D=2.77) compared with those of D=0.180 mm (L/D=4.44), both are identical orifice diameter. It can be thought that the longer liquid length of D=0.180 mm (L/D=4.44) is reasonable due to higher rate of fuel injection tends

to lack of fuel-ambient heating process. In this pair, D=0.180 mm (L/D=2.77) is found to achieve better atomization process due to wider scattering cone angle. An improvement in atomization process is found to promote mixing process as it can obviously be seen the shorten liquid length compared with D=0.180 mm (L/D=4.44). For low gas density of 11.7 kg/m^3, the D=0.180 mm (L/D=2.77) is found to be the largest liquid portion. The influence is comparable manner as shown in high gas density which D=0.180 mm (L/D=2.77) always reports the widest liquid cone angle. For overall observation of scattering image, as the gas density decreases with keeping gas temperature constant, this noticeably slows down liquid vaporization process. It is noted that the results of liquid cone angle and liquid length could not sequentially arranged in order regarding the L/D ratio. As the shadowgraph is sensitively detected the gas phase which includes liquid phase. The detected spray cone angles are useful for further analysis for estimation of fuel mixture. It can generally be seen that the vapor cone angle detected from shadowgraph image are wider than that of scattering for all image pairs. For D=0.180 mm (L/D=2.77), all gas densities gives the widest vapor cone angle among the others. This can be a result of high dispersion from better atomization leading to improved mixing process. Besides, the D=0.134 mm (L/D=3.73) provides comparable vapor cone angle to the D=0.180 mm (L/D=2.77), even they are almost half in different in rate of fuel injection. From that similarity in dispersion, it is remarkably needed for further investigation to understand fuel distribution inside the spray. It is found that a decrease in L/D ratio tends to promote spray dispersion. It is believed that a decrease in L/D ratio is likely to improve flow behavior that the droplets would widely be distributed and enhances heat transfer, consequence to the improved spray dispersion. A decrease in gas density affects reduction of resistance force that contributes into aerodynamic interaction between injected fuel and the surrounding gas. This lack of encounter part from the surrounding gas is supposed to hold high fuel concentration inside the spray, so that mixing and distribution could not efficiently be developed.

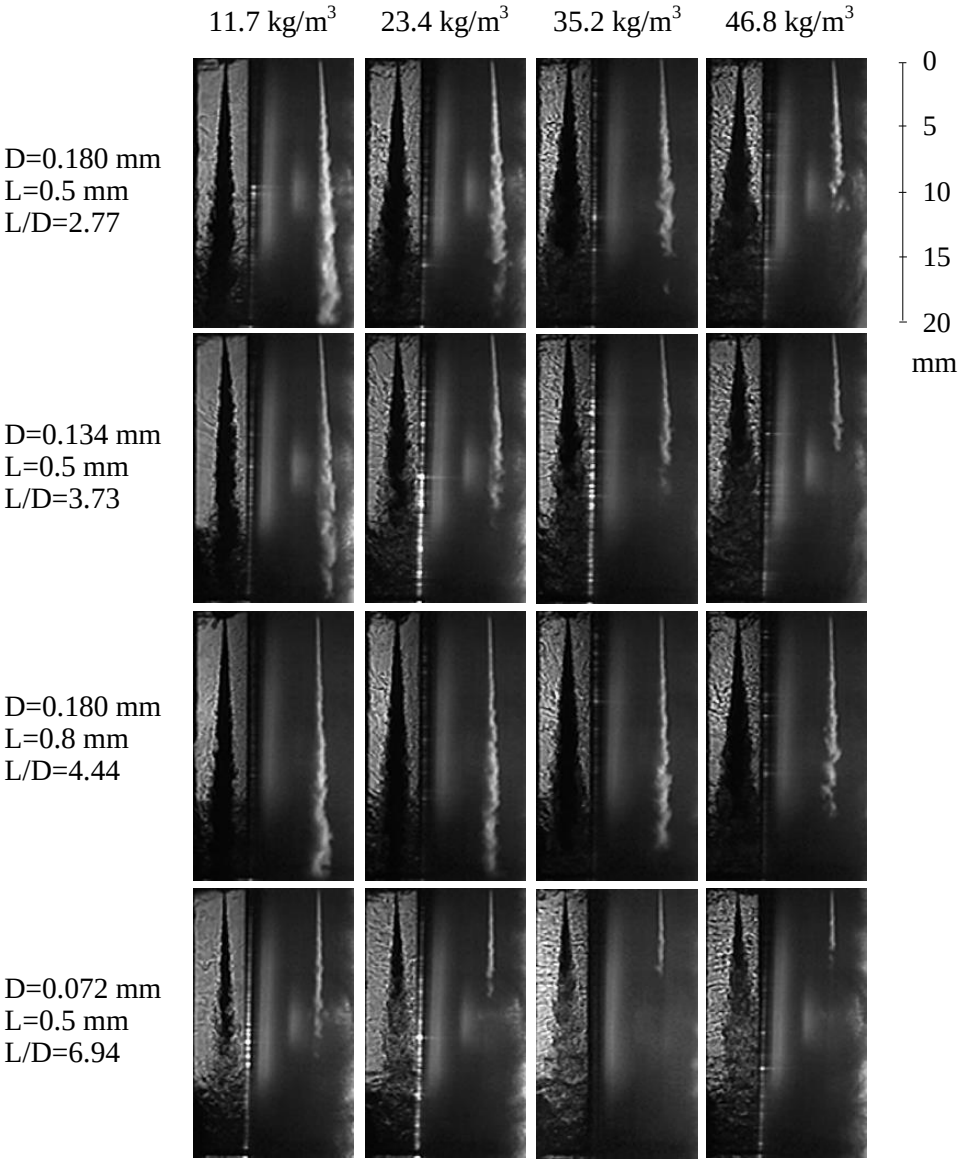

Figure 3.14 Instantaneous spray images for different nozzle specifications at 1.3 ms ASOI and surrounding gas temperature of 890 K.

3.5.3 Effect of Surrounding Gas Density on Vapor Penetration

The vapor penetration is one of the characteristics that describe the jet momentum and the liquid vaporization. In this study, the near-field fuel spray of 20-mm far from nozzle tip was imaged and processing of taken photographs demonstrated in Chapter 2 including detection of vapor penetration. Figure 3.15 shows vapor penetration at different surrounding gas densities. Because of wide range of operating gas conditions, it is clearly to see that the penetration is

slowdown when the jet enters an elevated surrounding gas pressure. High gas pressure generates high drag force that interacts with incoming jet and promotes breakup. With this the vapor dispersion tends to be higher due to better mixing process. With identical nozzle orifice size of D=0.180 mm, the longer hole length nozzle of L=0.8 mm shows longer vapor penetration due to its higher jet momentum.

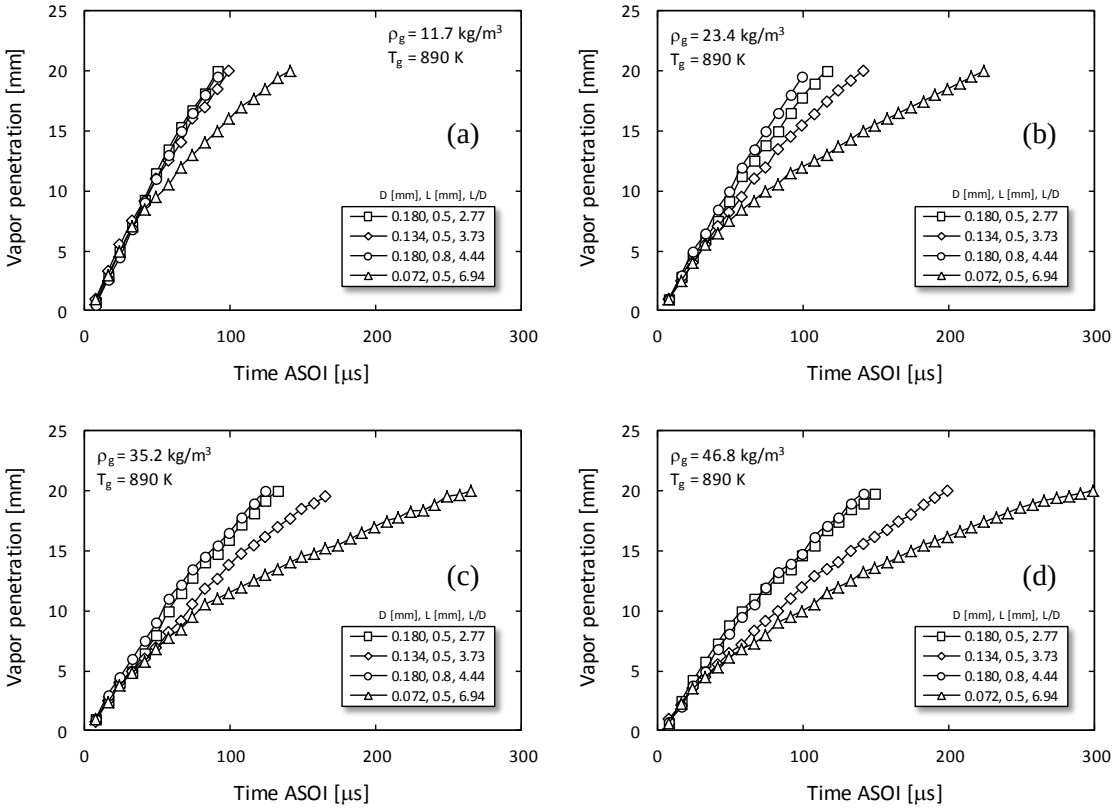

Figure 3.15 Vapor penetration at different surrounding gas densities. (a) 11.7 kg/m^3, (b) 23.4 kg/m^3, (c) 35.2 kg/m^3 and (d) 46.8 kg/m^3.

3.5.4 Effect of Surrounding Gas Density on Liquid Length

The liquid length is measurement of the maximum axial penetration distance of liquid phase fuel existing in an evaporating spray [21, 22]. To obtained information such as cone angle and liquid length from the taken images, image processing is carefully performed to appropriately detect liquid region as described at early stage in section 4.2. It is noted that not all experimental conditions that the liquid length can be detected. For example at high gas temperature but low gas density, the liquid is possible to penetrate over the capturing area of LL=20 mm far from nozzle tip. Therefore, the liquid length cannot be detected from those conditions. However, this

issue of over visualization length is considered as 20 mm and used in section 4.5 for estimation of fuel mixture. Figure 3.16 shows the effect of gas density on liquid length for four different nozzle specifications at gas temperature of 712 K and 890 K. From observation, the smallest orifice diameter of D=0.072 mm (L/D=6.94) provided the lowest rate of fuel injection exhibits the shortest liquid length. For D=0.072 mm (L/D=6.94) at the highest gas density of 46.8 kg/m^3, the liquid length of 5.02 mm and 7.84 mm are measured on gas temperature of 890 K and 712 K respectively. At gas density of 46.8 kg/m^3 for both gas temperatures of 890 K and 712 K, the longest liquid length is detected at D=0.180 mm (L/D=4.44), which nozzle gives the highest rate of fuel injection. Its value is reported to be 15.02 mm and 19.42 mm for gas temperature of 890 K and 712 K respectively. The liquid length measured at gas temperature of 890 K shows about 2-7 mm shorter than that of 712 K. This is a characteristic that the gas temperature is one of the main factors affecting the liquid length. The liquid length clearly shows an increasing tendency with decreasing surrounding density. It is found that an increase in L/D ratio is not responsible for shortening liquid length. The liquid length shows more sensitive to the rate of fuel injection and surrounding gas condition without relation with L/D ratio.

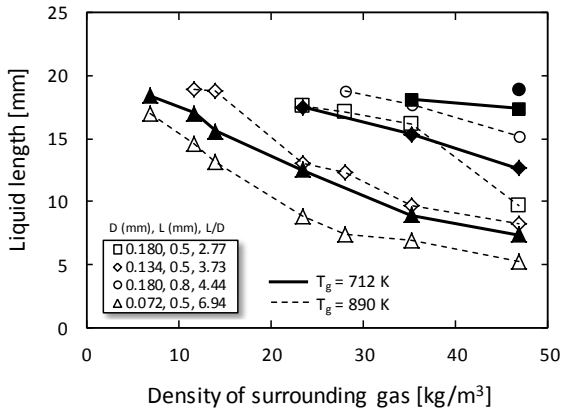

Figure 3.16 Effect of gas density on liquid length for different nozzle specifications.

3.5.5 Effect of Surrounding Gas Density on Spray Dispersion

The shadowgraph and scattering images were digitalized to obtain vapor and liquid phase boundaries respectively. Figure 3.17a-3.17c presents the measured liquid cone angle. The figure is vertically arranged for different gas temperature for 534 K, 712 K and 890 K ranging from the top to bottom. The liquid cone angle is plotted versus gas density for different four nozzle specifications. Each figure includes the legend to give detailed specifications of the the nozzle

and the marker information. It is generally seen that the liquid cone angle almost remains unchanged at high gas temperature of 890 K even when the gas density is changed. In Figure 3.17b at gas temperature of 712 K, the liquid cone angle detected from D=0.180 mm (L/D=2.77), D=0.134 mm (L/D=3.73) and D=0.180 mm (L/D=4.44) increase slightly with increasing gas density except D=0.072 mm (L/D=6.94). Figure 3.17a is at gas temperature of 534 K, it is classified as the lowest gas temperature in this experiment. It obviously exhibits that the liquid cone angle detected from D=0.180 mm (L/D=2.77) and D=0.134 mm (L/D=3.73) gives a tendency to increase with increasing gas density. The variation of liquid cone angle with gas density at low gas temperature is likely to be happened when spray dispersion is governed by breakup process. However, at high gas temperature, large difference between surrounding and liquid temperature can result in improvement in droplet heating and evaporation processes. This influence potentially overcomes dispersion of droplet associated with atomization. That is one possible reason caused liquid cone angle remaining unchanged with increasing gas density for gas temperature of 890 K. Figure 3.17d-3.17f displays measured vapor cone angle which is observed from shadowgraph. For overall observation, cone angle considerably increases with increasing the gas density, and it becomes more sensitive at higher gas temperature. This is implied that vapor cone angle is dominated by vaporization process due to high variation of cone angle actively found at high temperature range. This spreading angle increasing tendency is unlikely the same as liquid atomization which is high tendency to take place at low gas temperature. Comparing among nozzle specifications for each gas temperature provides and global conclusion that the D=0.180 mm (L/D=2.77) overcomes the others indicated the highest dispersion. An increase in gas temperature with the same gas density show liquid vaporization favored resulting into wider vapor cone angle and shortens liquid length shown in Figure 3.16. The smallest cone angle is indicated to be the nozzle D=0.072 mm (L/D=6.94) mm. This is because the small orifice diameter comes with low spray momentum and lack of spray concentration due to low rate of fuel injection that cannot achieve appropriate spray dispersion.

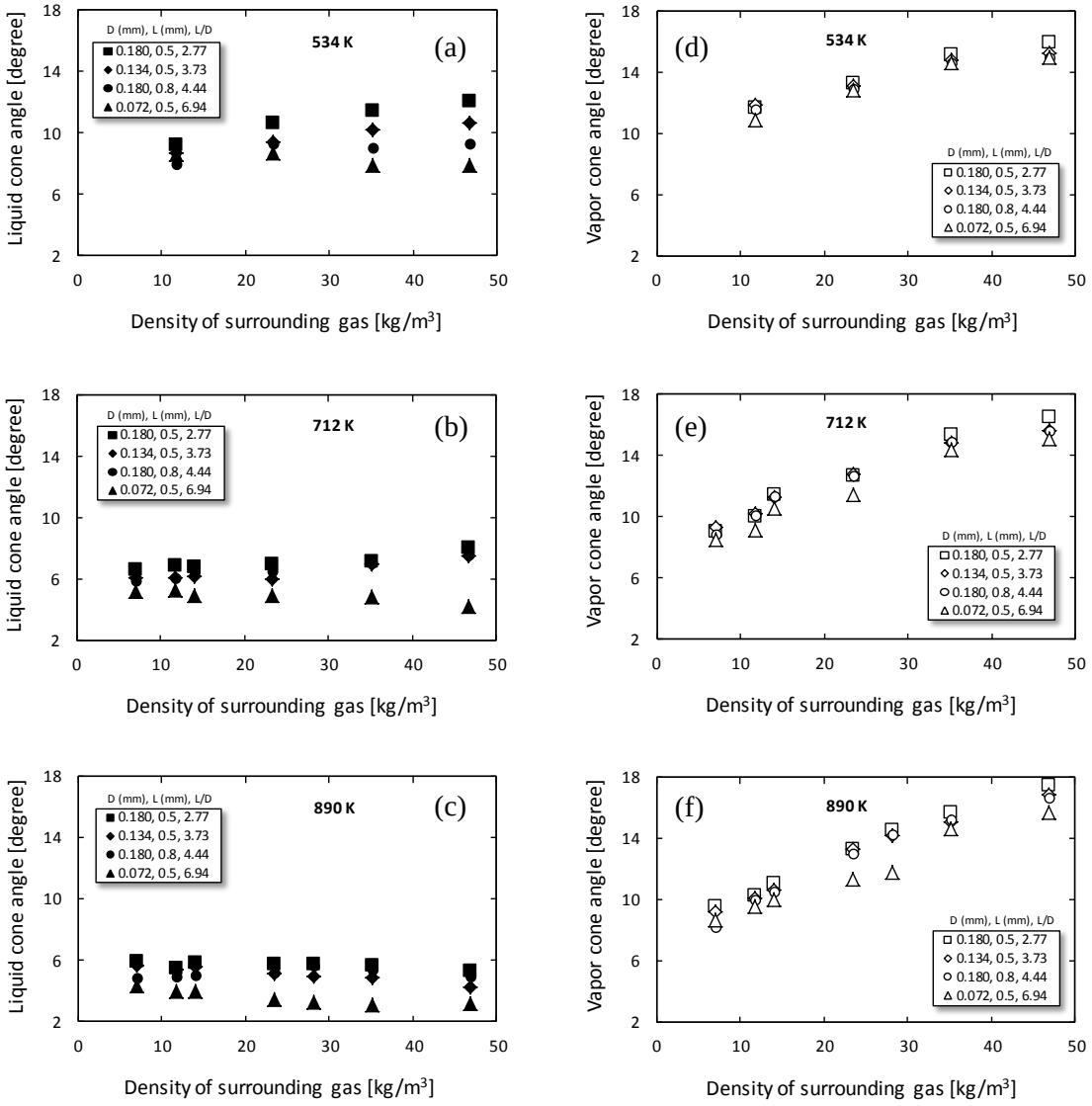

Figure 3.17 Effect of gas density on cone angles. (a) – (c) for liquid cone angle, and (d)-(f) for vapor cone angle for gas temperature of 534 – 890 K.

In general, liquid vaporization can be enhanced by increasing gas temperature and pressure. However, liquid cone angle is related with several factors such as breakup and vaporization. Figure 3.18 shows the effect of surrounding gas temperature on liquid cone angle. It is roughly found that an increase in gas temperature can promote liquid vaporization as a consequence of smaller liquid cone angle. With identical nozzle orifice size of D=0.180 mm, the shorter hole length nozzle of L=0.5 mm shows the wider liquid cone angle than that of the longer one. It can be implied that the shorter hole length nozzle has potential to breakup faster due to high amount of cavitation. This breakup and atomization lets the cone angle to be wider. The enhancement of atomization due to higher gas density is prominently seen as the liquid cone angle increases

with an increase in gas density. On the other hands, the smallest nozzle orifice size of D=0.072 mm shows smallest liquid cone angle for all surrounding gas density conditions. This is because smaller orifice size nozzle tends to generate smaller droplets size which can be heated and evaporated faster

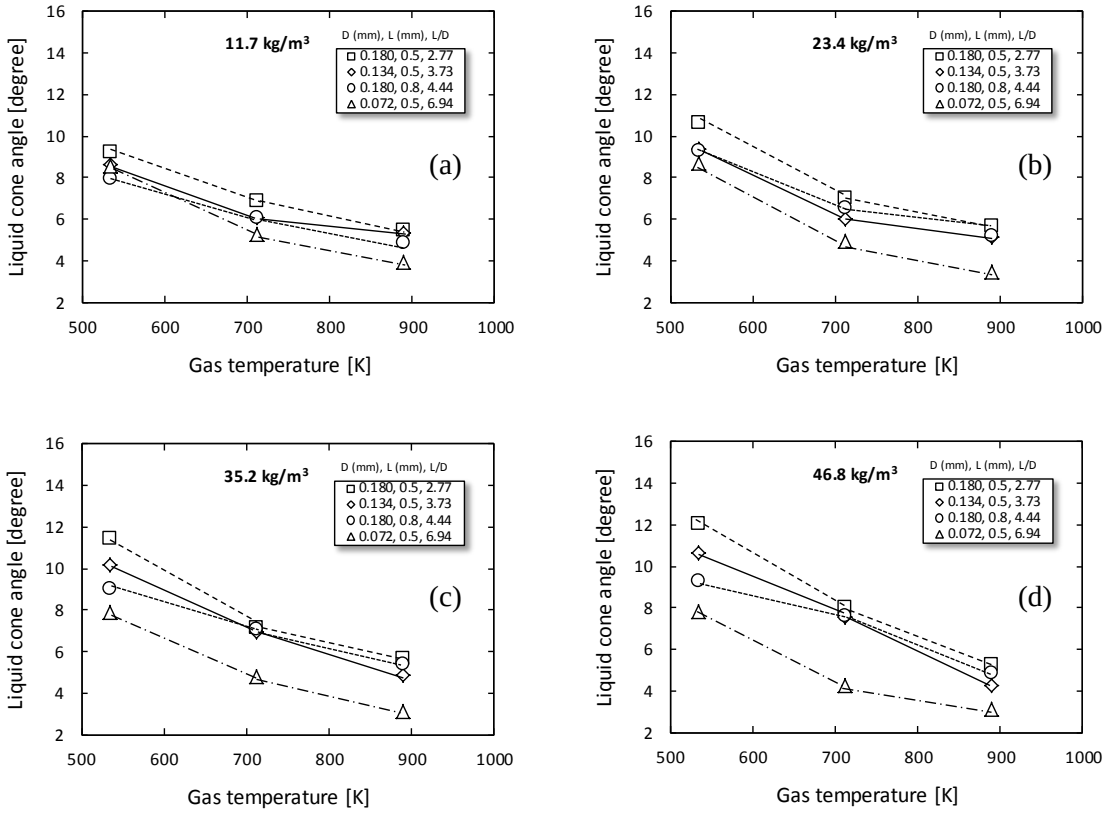

Figure 3.18 Effect of surrounding gas temperature on liquid cone angle for different nozzle specifications.

3.5.6 Effect of Weber Number on Spray Dispersion

Weber number is a dimensionless number that uses to analyze the fluid flow where there is an interface between two different fluid, in this case liquid droplet and surrounding gas. Weber number is a ratio of fluid inertia to surface tension of the liquid. The higher Weber number, the higher possibility that liquid jet undergoes breakup process. The factor that involves Weber number is gas density, jet velocity, nozzle orifice size and fuel surface tension. Figure 3.19a shows the liquid cone angle that the relation cannot be found with Weber number. However, there is a decreasing trend for smallest orifice nozzle of D=0.072 mm with Weber number increases. This characteristic is suspicious, but one possible reason is that at high Weber number

due to high gas density, the smallest orifice size nozzle that comes with smaller droplets size is dominated by the vaporization rather than breakup or atomization processes. Figure 3.19b shows the vapor cone angle with variation of Weber number. It is clear that the Weber number could be used to signify vapor dispersion. The most sensitive to the Weber number is the smallest orifice size nozzle. With identical orifice size nozzle of D=0.180 mm, there seems to show similar sensitivity, but the shorter hole length nozzle gives wider cone angle for all ranges of Weber number.

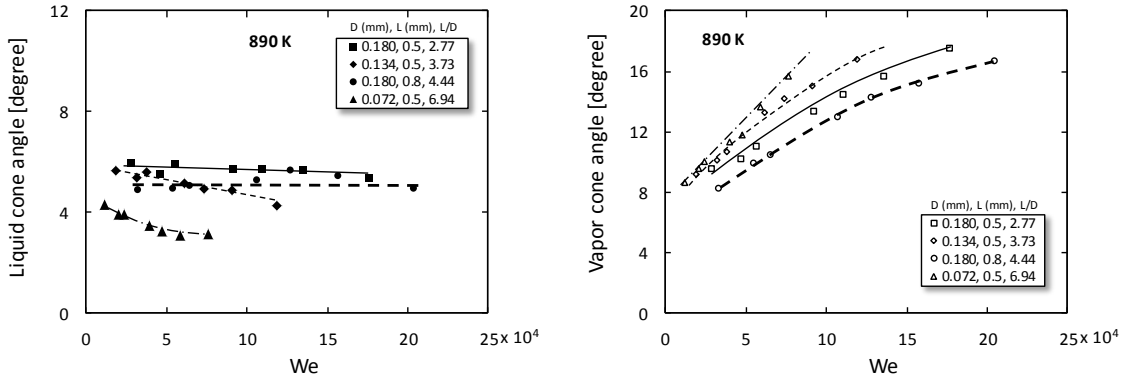

(a) (b)

Figure 3.19 Effect of Weber number at nozzle exit on liquid and vapor cone angles for T_g = 890 K.

3.5.7 Effect of Surrounding Gas Density on Entrainment

Figure 3.20 shows mass of entrained gas characteristics for different nozzle specifications with increasing gas density. Increasing the gas density directly stimulates the atomization process resulting in wider spray cone angle. With those points, it gives a chance for entrainment of surrounding gas into the spray. All nozzle specifications show significantly improvement in air entrainment with increasing gas density. With the smallest orifice size nozzle D=0.072 mm (L/D=6.94), it shows the lowest mass of entrained gas for all gas density range compared with the other nozzles. This is because the low rate of fuel injection that could not provide enough spray momentum to interact with surrounding gas leading to slowdown spray development. The smaller vapor cone angle is observed for this smallest nozzle specification. With orifice size nozzles of 0.180 mm, the shorter hole length D=0.180 mm (L/D=2.77) provides higher mass of entrained gas, which is found to be a unique feature for this shorter hole length nozzle. Due to high rate of fuel injection for D=0.180 mm, as previously discussed in produced fuel vapor mass, Figure 3.20 for nozzle D=0.180 mm nozzle provides an evidence to support that the higher amount of entrainment help improvement in liquid vaporization process. In Figure 3.21, an

increase in entrained gas amount is likely not to affect the liquid cone angle, but for vapor cone angle it is found to be obviously increases by increasing entrained gas amount. This is as it was expected that the vapor cone angle which contains entrained gas should be directly expanded when large amount of surrounding gas comes into the spray.

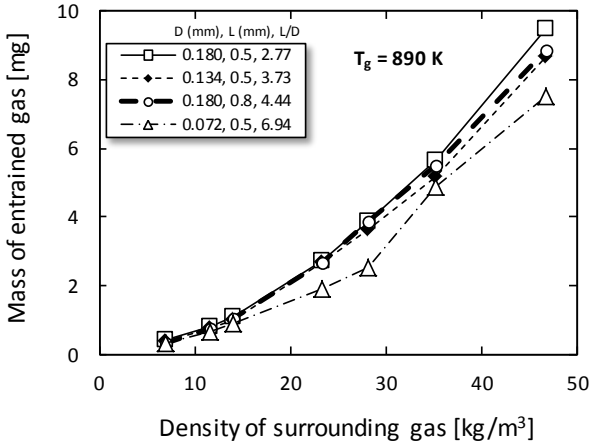

Figure 3.20 Effect of gas density on entrained gas mass for T_g = 890 K.

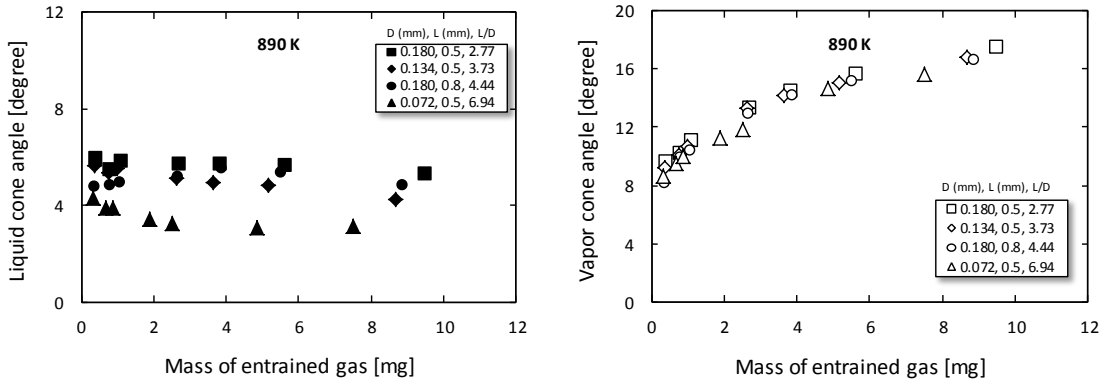

(a) (b)

Figure 3.21 Effect of entrained gas mass on liquid and vapor cone angles for T_g = 890 K.

3.5.8 Fuel/Air Mixture Characteristics in Near-Field Region

Figure 3.22 presents effect of gas density on mass of liquid fuel for four different nozzle specifications at gas temperature of 890 K. In horizontal axis, the surrounding gas density ranges between 7-46.8 kg/m^3. It is globally seen that increasing the gas density stimulates liquid phase to be vaporized into gaseous phase as a decrease in liquid mass for all nozzle

specifications. At all gas densities, the D=0.072 mm (L/D=6.94), shows substantially lower amount in liquid fuel mass compared with that of the others due to the lowest rate of fuel injection. It obviously coincides with small fuel scattering region shown in Figure 3.14 compared to the other nozzle specifications at the same gas density. The D=0.134 mm (L/D=3.73) shows significant reduction of liquid fuel mass in the range of gas density of 7-23.4 kg/m^3 and then keeping slowdown reduction until 46.8 kg/m^3. This could suggest that the the mixing process is efficiently performed at low to moderate gas density. Due to large nozzle orifice size of D=0.180 mm (L/D=2.77) and D=0.180 mm (L/D=4.44), the result shows high liquid fuel mass in all levels of gas density excepting at gas density of 7 kg/m^3 reporting somewhat lower amount of liquid fuel for D=0.180 mm (L/D=4.44). In the condition that the gas density higher than 20 kg/m^3, the liquid mass resulted from the D=0.180 mm (L/D=2.77) shows lower liquid fuel mass compared with that produced from D=0.180 mm (L/D=4.44). This result is a consequence of previous section of comparable liquid cone angles together with large vapor cone angle expanded by efficiently mixing process with stimulating a liquid vaporization. As a result, whole spray mixture fraction for D=0.180 mm (L/D=2.77) becomes diluted. However, the low amount of liquid fuel is observed for D=0.180 mm (L/D=4.44) for gas density of 11.7 kg/m^3. The result of liquid fuel mass is consistent with cone angles of both scattering and shadowgraph reported in Figure 3.17 showing small cone anlges. It would be the reason that high momentum jet with low aerodynamic drag of back pressure resulting into dense spray phase with lack of atomization process that the mixture could not be developed within this visualization region of 20 mm. Comparing between the D=0.180 mm (L/D=2.77) and D=0.180 mm (L/D=4.44) which are identical orifice diameter of 0.180 mm, the shorter nozzle hole length of L/D=2.77 is found to achieve better vaporization in moderate and high gas density.

The different nozzle orifice sizes would of course provide the different rate of fuel injection as well as the difference in spray formation characteristics. In addition to mass of liquid fuel, the fuel vapor phase produced which is a consequence of liquid break up and improved mixing due to entrained gas is shown in Figure 3.23. It is quantification of amount of vapor phase fuel with compensation of different rate of fuel injection due to orifice size different. The vertical axis is the mass ratio of vapor fuel m_{fvp} over the total fuel which is $m_{flq} + m_{fvp}$. This is as expected from the result depicted in Figure 3.22 that decreasing in liquid mass would be a consequence of an increase in vapor mass. The global tendency for all nozzle specifications shows the vapor fuel mass produced with increasing gas density, indicated almost the ratio of 0.9 at gas density of 46.8 kg/m^3 for all nozzle specifications except D=0.180 mm (L/D=4.44). With the smallest nozzle orifice size D=0.072 mm (L/D=6.94), the mixture is improved quickly as increasing the gas density and reaches its highest level at gas density of 30-46.8 kg/m^3. The injection from a small orifice size is that the fined droplets are formed giving a possibility for achieving liquid

vaporization process. For D=0.134 mm (L/D=3.73), the ratio of vapor fuel mass drastically increases from 0.22 to 0.82 at gas density ranging from 7 to 23.4 kg/m^3 and then remains a slight increase. For the identical orifice size of 0.180 mm, both nozzles show similar characteristics of almost linearly produced fuel vapor. However, the nozzle orifice size D=0.180 mm (L/D=2.77) exhibits favorable mixture compared with that D=0.180 mm (L/D=4.44). This higher fuel vapor mass at middle to high gas density range for D=0.180 mm (L/D=2.77) is a relevant outcome from reduction of fuel liquid mass shown in Figure 3.22.

In diesel spray, air entrainment plays an important role in mixing process related with heating and evaporation of liquid fuel. It is a key factor which affects the spray formation, local equivalent ratio and ignition process for combustion view point. In this study, air entrainment was calculated based on a fuel mixture fraction considering from full spreading angle as schematically expressed in Figure 3.12. Figure 3.24 presents the effect of gas density on fuel vapor mass to entrained gas mass ratio. The value of m_{fvp}/m_{N2} ratio provides information about how large amount of gas entrained into the spray compared with fuel vapor phase. The mass ratio exhibits lower than unity for all nozzle specifications except gas density of 7 kg/m^3 for D=0.072 mm (L/D=6.94). In previous discussion of Figure 3.23 and Figure 3.20, it was found that both vapor fuel mass and entrained gas mass increase with increasing gas density. In addition to those descriptions, Figure 3.24 indicates that the entrained gas even more increases with increasing the gas density since the large amount of entrained gas compared with amount of fuel vapor made the mass ratio considerably declined versus gas densities for all nozzle specifications. The vapor fuel to entrained gas mass ratio generated by each nozzle specifications roughly reports comparable values for all surrounding gas density except gas density of 11.7 kg/m^3. It should be noted that, the nozzle D=0.180 mm (L/D=2.77) exhibits a similar level of vapor-gas mass ratio at gas density of 25-46.8 kg/m^3 compared with that D=0.180 mm (L/D=4.44). This is not because of lack of produced fuel vapor but due to higher amount of entrainment. The present procedure given so far is the estimated spray mixture quantities obtained from taken liquid and vapor fuel phase photographs, which would be useful for further study on fuel-spray ignition and combustion characteristics.

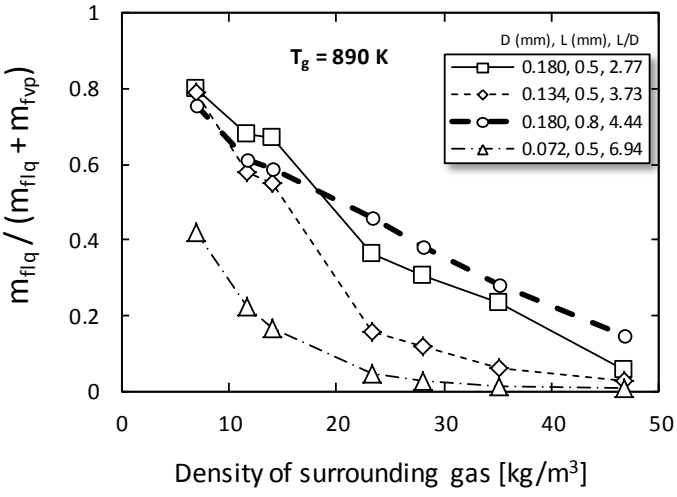

Figure 3.22 Influence of gas density on estimated near-field fuel in liquid phase at different nozzle specifications for T_g = 890 K.

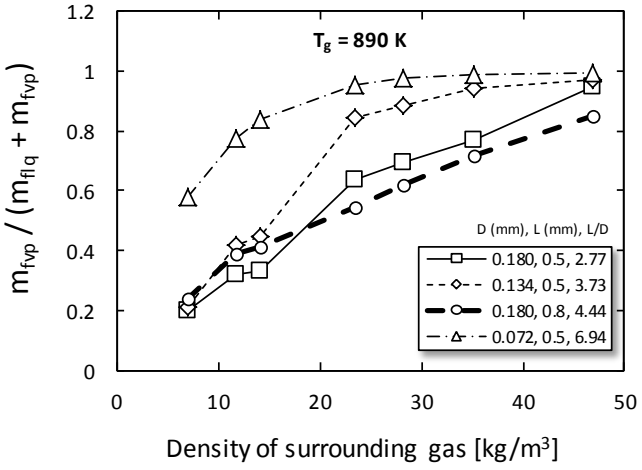

Figure 3.23 Effect of gas density on fuel vapor mass to total fuel mass ratio for T_g = 890 K.

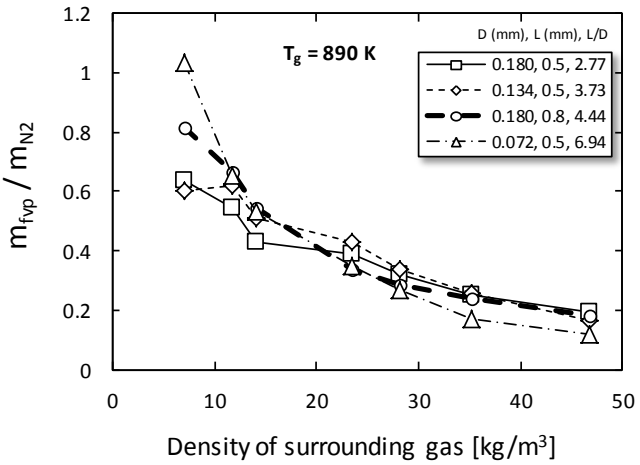

Figure 3.24 Effect of gas density on fuel vapor to entrained gas mass ratio for T_g = 890 K.

Figure 3.25 shows the effect of gas density on equivalence ratio based on vapor fuel. The global fashion indicated that large amount of vapor fuel existing at low gas density and significantly decreasing as an increase in gas density was due to entrainment of surrounding gas into spray. With identical orifice diameter of 0.180 mm, the shorter hole length nozzle of L=0.5 mm reported richer mixture at about gas density of 20-46.8 kg/m^3. It was because D=0.180 mm (L/D=2.77) contained higher vapor fuel amount as a consequence of higher entrained gas stimulating liquid vaporization process. In addition to achieving the mixing process for the shorter hole length nozzle of L=0.5 mm, the shorter liquid length was also found compared with the longer one of L=0.8 mm.

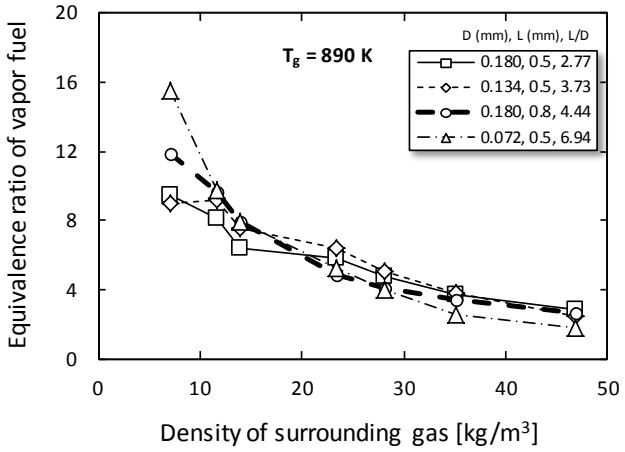

Figure 3.25 Effect of gas density on equivalence ratio based on fuel vapor phase for T_g = 890 K.

3.6 Conclusions

The effect of nozzle hole length to diameter ratio was investigated using a rapid compression-expansion machine under wide range of operating surrounding gas conditions. High-speed microscopy experiment was performed to capture vapor and liquid phase in diesel fuel spray at near-field region. The information extracted from the images was then used for estimation of fuel mixture. The main results of this work are listed below:

1. Liquid length was dominated by both gas density including gas temperature and injected fuel amount. It was not absolutely only contributed by L/D ratio. An increase in gas density increased interaction between injected fuel and surrounding gas and promoted atomization. Liquid cone angle noticeably increased with increasing gas density at low gas temperature of 534 K due to atomization dominated and lack of heat transfer between droplets and surrounding gas. It was relatively unchanged at gas temperature of 712 K and 890 K since dispersion could possibly be suspended at higher gas temperature. Vapor cone angle was observed to increase with L/D ratio decreased. The widest vapor cone angle was found at D=0.180 mm (L/D=2.77) corresponded to achievement of the highest mass of fuel in vapor phase.
2. At constant gas temperature of 890 K, fuel mass in liquid phase considerably decreased with increasing gas density. Hence, atomization was stimulated by increasing gas density, then consequentially to promote liquid vaporization. However, the vaporization became weaker

at elevated gas density for small orifice size nozzles D=0.134 mm (L/D=3.73) and D=0.072 mm (L/D=6.94) compared with that of larger size of D=0.180 mm due to low rate of fuel injection.

3. An increase in gas density significantly enhanced fuel-gas interaction and increased turbulence which showed produced vapor fuel. Until a certain gas density, the vapor phase became moderate fashion with increasing gas density for the orifice diameters smaller than 0.180 mm. For orifice diameter of 0.180 mm on both L/D=2.77 and L/D=4.44, the vapor fuel mass almost linearly increased with increasing gas density.
4. For fuel vapor to entrained gas mass ratio at high density range of 30-46.8 kg/m^3, it was found to be comparable for identical nozzles D=0.180 mm due to higher amount of both fuel vapor and entrained gas produced by D=0.180 mm (L/D=2.77) and lower amount of both quantities by D=0.180 mm (L/D=4.44).
5. With identical orifice diameter of 0.180 mm, the smaller L/D=2.77 which corresponds to shorten nozzle hole length achieved mixing process, shorten liquid length and superior entrainment compared with L/D=4.44. It was believed that the internal flow was developed by the shorter hold length nozzle.
6. With large variation of nozzle orifice size of the present study, to describe the effect of gas condition on liquid and vapor phase quantities in spray, not either L/D ratio or orifice diameter, both are necessary information. This is because the orifice diameter affects rate of fuel injection.

Bibliography

[1] D. MacMillan, A. La Rocca, P. J. Shayler, M. Murphy and I. G. Pegg, "The Effect of Reducing Compression Ratio on the Work Output and Heat Release Characteristics of a DI Diesel under Cold Start Conditions," SAE Int. J. Engines, 1(1): 794-803, 2009.

[2] R.N. Dahms and J.C. Oefelein, "On the Transition between Two-Phase and Single-Phase Interface Dynamics in Multicomponent Fluids at Supercritical Pressure," Physics of Fluids 25, 2013.

[3] J.M.H. Levelt Senger, "Thermodynamics of Solutions Near the Solvent's Critical Point," in Supercritical Fluid Technology, edited by T. J. Bruno and J. F. Ely, CRC Press, Boca Raton, FL, Chapter 1, 1991.

[4] Manin J., Bardi M., Pickett L. M., Dahms R. N. and Oefelein J. C., "Microscopic Investigation of the Atomization and Mixing Processes of Diesel Sprays Injected into High Pressure and Temperature Environments," Fuel 134, 531–43, 2014.

[5] Pickett, L., Manin, J., Kastengren, A., and Powell, C., "Comparison of Near-Field Structure and Growth of a Diesel Spray Using Light-Based Optical Microscopy and

X-Ray Radiography," SAE Int. J. Engines 7(2):1044-1053, 2014.

[6] Kastengren, A., Powell, C., Cheong, S., Wang, Y. et al., "Determination of Diesel Spray Axial Velocity Using X-Ray Radiography," SAE Technical Paper 2007-01-0666, 2007.

[7] Leick P, Reidel T, Bittlinger G, Powell CF, Kastengren AL, Wang J,Wang J, "X-ray Measurements of the Mass Distribution in the Dense Primary Break-Up Region of the Spray from a Standard Multi-Hole Common-Rail Diesel Injection System," In: Proceedings of the 21st ILASS-Europe meeting, 2007.

[8] Zhang, G., Xu, M., Zhang, Y., and Zeng, W., "Quantitative Measurements of Liquid and Vapor Distributions in Flash Boiling Fuel Sprays using Planar Laser Induced Exciplex Technique," SAE Technical Paper 2011-01-1879, 2011.

[9] J. Kamrak, B. Kongsombut, G. Grehan, S. Saengkaew, K. Kim, T. Charinpanitkul, "Mechanistic Study on Spraying of Blended Biodiesel using Phase Doppler Anemometry," Biomass and Bioenergy, Vol. 33, Issue 10, Pages 1452–1457, 2009.

[10] Pickett, L., Kook, S., and Williams, T., "Visualization of Diesel Spray Penetration, Cool-Flame, Ignition, High-Temperature Combustion, and Soot Formation Using High-Speed Imaging," SAE Int. J. Engines 2(1):439-459, 2009.

[11] Montanaro, A., Migliaccio, M., Allocca, L., Fraioli, V. et al., "Schlieren and Mie Scattering Visualization for Single-Hole Diesel Injector under Vaporizing Conditions with Numerical Validation," SAE Technical Paper 2014-01-1406, 2014.

[12] C. Yao, P. Geng, Z. Yin, J. Hu, D. Chen, Y. Ju, "Impacts of Nozzle Geometry on Spray Combustion of High Pressure Common Rail Injectors in a Constant Volume Combustion Chamber," Fuel, 179 , pp. 235-245, 2016.

[13] K. Ramamurthi, K. Nandakumar, "Characteristics of Flow Through Small Sharp-Edged Cylindrical Orifices," Flow Measurement and Instrumentation, 10 (3), pp. 133-143,1999.

[14] P. Dong, K. Nishida, Y. Ogata, "Characterization of Multi-Hole Nozzle Sprays and Internal Flow for Different Nozzle Hole Lengths in Direct-Injection Diesel Engines," Proc. IMechE Part D: J. Automobile Engineering, 2016.

[15] C. Espey, J.E. Dec, T.A. Litzinger and D.A. Santavicca, "Planar Laser Rayleigh Scattering for Quantitative Vapor-Fuel Imaging in a Diesel Jet," Combustion and Flame, 1997.

[16] Bohren, C. F.; Huffman, D. R , "Absorption and Scattering of Light by Small Particles," Wiley-VCH, 1st ed , 1983.

[17] Mark P.B. Musculus and Kyle Kattke, "Entrainment Waves in Diesel Spray," SAE 2009-01-1355, 2009.

[18] Kobori, S. and Kamimoto, T., "Development of a Rapid Compression-Expansion Machine Simulating Diesel Combustion," SAE Technical Paper 952514, 1995.

[19] Ganser, M., "Common Rail Injector with Injection Rate Control;" SAE Technical Paper

981927; SAE International: Warrendale, PA, USA, 1998.

[20] Lee, C., "An Experimental Study on Advanced Injection Rate Measurement of a Marine Engine using the Zeuch method," J. Therm. Sci. Technol.,11, JTST0026, 2016.

[21] Siebers, D., "Liquid-Phase Fuel Penetration in Diesel Sprays," SAE Technical Paper 980809, 1998.

[22] J. Manin, M. Bardi, and L. M. Pickett, "Evaluation of the Liquid Length via Diffused Back-Illumination Imaging in Vaporizing Diesel Sprays," in Proceedings of the 8th International Conference on Modeling and Diagnostics for Advanced Engine Systems, COMODIA 2012, 2012.

[23] Pickett, L., Manin, J., Genzale, C., Siebers, D. et al., "Relationship Between Diesel Fuel Spray Vapor Penetration/Dispersion and Local Fuel Mixture Fraction," SAE Int. J. Engines 4(1):764-799, 2011.

[24] A. Andriotis, "Investigation of cavitation inside multi-hole injectors for large diesel engines and its effect on the near-nozzle spray structure," in PhD Thesis, City Univeristy, 2009.

[25] H. Chaves, M. Knapp, A. Kubitzek, F. Obermeier, and T. Schneider, "Experimental study of cavitation in the nozzle hole of diesel injectors using transparent nozzles,"tech. rep., SAE Technical Paper, 1995.

[26] L. He and F. Ruiz, "Effect of cavitation on flow and turbulence in plain orifices for high-speed atomization," Atomization and Sprays, vol. 5, no. 6, 1995.

[27] C. Soteriou, R. Andrews, and M. Smith, "Direct injection diesel sprays and the effect of cavitation and hydraulic flip on atomization," tech. rep., SAE Technical Paper, 1995.

[28] W. Lauterborn and C. D. Ohl, "Cavitation bubble dynamics," Ultrasonics Sonochemistry, vol. 4, no. 2, pp. 65–75, 1997.

[29] M. E. Henry and S. H. Collicott, "Visualization of internal flow in a cavitating slot orifice," Atomization and Sprays, vol. 10, no. 6, 2000.

[30] E. Winklhofer, E. Kull, E. Kelz, and A. Morozov, "Comprehensive hydraulic and flow field documentation in model throttle experiments under cavitation conditions,"in ILASS-Europe, 17th International Conference on Liquid Atomization and Spray Systems, 2001.

[31] C. Badock, R. Wirth, A. Fath, and A. Leipertz, "Investigation of cavitation in real size diesel injection nozzles," International Journal of Jeat and Fluid Flow, vol. 20, no. 5, pp. 538–544, 1999.

[32] A. Andriotis, M. Gavaises, and C. Arcoumanis, "Vortex flow and cavitation in diesel injector nozzles," Journal of Fluid Mechanics, vol. 610, pp. 195–215, 2008.

[33] T. Hayashi, M. Suzuki, and M. Ikemoto, "Visualization of internal flow and spray

formation with real size diesel nozzle," in 12th Triennial International Conference on Liquid Atomization and Spray Systems, ICLASS, pp. 2–6, 2012.

[34] H. Watanabe, M. Nishikori, T. Hayashi, M. Suzuki, N. Kakehashi, and M. Ikemoto, "Visualization analysis of relationship between vortex flow and cavitation behavior in diesel nozzle," International Journal of Engine Research, vol. 16, no. 1, pp. 5–12, 2015.

[35] D. P. Schmidt, C. J. Rutland, and M. L. Corradini, "A fully compressible, twodimensional model of small, high-speed, cavitating nozzles," Atomization and Sprays, vol. 9, no. 3, 1999.

[36] A. Sou, B. Bic¸er, and A. Tomiyama, "Numerical simulation of incipient cavitation flow in a nozzle of fuel injector," Computers & Fluids, vol. 103, pp. 42–48, 2014.

[37] G. H. Schnerr and J. Sauer, "Physical and numerical modeling of unsteady cavitation dynamics," in 4th International Conference on Multiphase Flow, New Orleans, USA, vol. 1, 2001.

[38] A. K. Singhal, M. M. Athavale, H. Li, and Y. Jiang, "Mathematical basis and validation of the full cavitation model," Journal of Fluids Engineering, vol. 124, no. 3, pp. 617–624, 2002.

[39] R. F. Kunz, D. A. Boger, D. R. Stinebring, T. S. Chyczewski, J. W. Lindau, H. J. Gibeling, S. Venkateswaran, and T. Govindan, "A preconditioned navier–stokes method for two-phase flows with application to cavitation prediction," Computers & Fluids, vol. 29, no. 8, pp. 849–875, 2000.

[40] A. Alajbegovic, D. Greif, B. Basara, and U. Iben, "Cavitation calculation with the two-fluid model," in 3rd European-Japanese Two-Phase Flow Group Meeting, Certosa di Pontignano, 2003.

[41] P. J. Zwart, A. G. Gerber, and T. Belamri, "A two-phase flow model for predicting cavitation dynamics," in Proceedings of the 5th International Conference on Multiphase Flow, Yokohama, Japan, 2004.

[42] C. L. Merkle, J. Feng, and P. E. Buelow, "Computational modeling of the dynamics of sheet cavitation," in 3rd International Symposium on Cavitation, Grenoble, France, vol. 2, pp. 47–54, 1998.

[43] E. Giannadakis, M. Gavaises, and C. Arcoumanis, "Modelling of cavitation in diesel injector nozzles," Journal of Fluid Mechanics, vol. 616, pp. 153–193, 2008.

[44] OpenFOAM. http://www.opencfd.co.uk.

[45] B. Bicer , A. Tanaka , T. Fukuda , A. Sou , Numerical simulation of cavitation phenomena in diesel injector nozzles, in: Proceedings of the 16th Annual Conference ILASS-ASIA, Nagasaki, Japan, pp. 58–65, 2013.

[46] H.G. Weller, G. Tabor, H. Jasak, C. Fureby, A tensorial approach to computational

continuum mechanics using object-oriented techniques, Comput. Phys. 12 (6), 1998.

[47] CFD Direct, Architects of OpenFOAM. “OpenFOAM User Guide”. URL: http://cfd.direct/openfoam/user-guide/

CHAPTER 4
RELATION BETWEEN MIXTURE FORMATION IN THE NEAR FIELD AND COMBUSTION CHARACTERISTICS

4.1 Introduction

Pollutant emission generated from diesel engines strongly depends on the fuel/air mixture formation in a combustion chamber [1]. The modern diesel engines employ a micro orifice with different nozzle designs and it is critical to characterize the effect of various designs on engine performance and emissions. Effect of nozzle diameters on combustion and emission have been studied by a number of researchers. The smaller orifice size showed improvement in atomization, vaporization and fuel/air mixing resulting in a shorter ignition delay [2]. However, negative effect of small nozzle was NOx increasing. When fuel injection pressure was low, fuel particle diameters was enlarged and ignition delay increased [3]. The geometry inside the nozzle plays a vital role in controlling diesel spray atomization and combustion. In order to bring fuel droplet size small, the nozzle-hole size is required to be reduced to produce smaller droplets [4]. By decreasing the nozzle hole size, the spray tip penetration is reduced due to low spray momentum. High injection pressure with small nozzle is a common in the modern diesel engine as it reduces injection duration and improves combustion efficiency [5]. Combustion tests were carried out with micro-hole nozzle of 0.06 mm using a rapid compression-expansion machine [6]. Ignition delay was decreased by 30%, and in spite of that, both peaks of initial premixed combustion and diffusion combustion increased significantly. Different orifice designs such as hydroground and conical nozzles were investigated using computational simulation [7]. For the conical nozzle, the relative role of rich premixed combustion was enhanced and that of diffusion combustion reduced. The mixture formation process of flat wall impinging spray with micro-hole nozzle of 0.08 mm under ultra-high injection pressure of 300 MPa was studied [8]. The result showed that the combination of micro-hole nozzle and ultra-high injection pressure is effective to obtain fast vaporization and high air entrainment rate. Effects of ambient temperature, oxygen concentration and air entrainment into the spray on heat release process were studied [9]. They reported that initial heat release was activated to some periods by an increase in air entrainment into spray during ignition delay. From the literatures reviewed above, the effects of nozzle specifications, injection conditions, and surrounding gas conditions on the characteristics of fuel sprays and spray combustions have been investigated. However, the relation between the formation of fuel/air mixture in the near-nozzle field and combustion phenomena in downstream in spray flame has not been made clear especially at high boosted surrounding gas conditions.

In recent past, our study has been outlined to declare the relationship of fuel/air mixture

formation through combustion and emission particularly at relevant condition of the current heavy diesel engine. We hypothesized that the nozzle geometry would significantly affect the spray process especially at near-nozzle field region and expect to result in downstream mixture. This is because during combustion, burned gas at flame periphery tends to prevent or slowdown entrainment of surrounding gas. Then, surrounding gas condition that generally contributes substantial effect on atomization and mixing processes was considered as a studied parameter together with nozzle specifications. The near-field spray imaging technique was successfully conducted. Some distinct mixture behaviors had evidently been found. The present study is to investigate the combustion and emission characteristics regarding the variations of surrounding gas conditions and the nozzle specifications that are identical set with the previous conducted near-field spray experiment [10], and to clarify the relation between the characteristics of fuel/air mixture formation in near-nozzle field and that of combustion in downstream of spray flame in the wide range of surrounding densities including high boosted conditions.

4.2 Experimental Setup

After a single-shot compression, combustion at constant volume during piston stopping at TDC was taken place, luminous flame photo with soot and NOx emissions were recorded. Detailed experimental setup is shown in Figure 4.1. The compression unit used to simulate the desired ambient conditions employed a rapid compression and expansion machine RCEM [11] equipped with a cylinder block and fuel injection unit. RCEM is an electronically controlled and hydraulically actuated driving system which can simulate intake, compression, expansion and exhaust strokes in a single diesel cycle. RCEM was used as a rapid compression machine RCM to achieve the diesel combustion at constant volume condition in this study. The flame was a luminous diffusion flame observed through optical quartz window inserted in the cylinder head. The flame was captured by NAC GX-1 high speed camera with recorded frame rate of 10,000 fps, exposure time of 3 μs and image resolution of 464x464 pixels. The camera was fitted with Nikon 200 mm f/4 AF-D macro lens. In addition to avoid undesirable wavelength during flame imaging, a HOYA HA-50 infrared filter was placed in front of the camera for infrared cutoff. For emission measurement, soot concentration was measured by passing exhaust gas from combustion chamber through the filter paper using a vacuum pump. Smoke was trapped by a filter paper placed inside a smoke holder and it was then measured using GSM-3 smoke meter manufactured by TSUKASA SOKKEN. For NOx concentration measurement, exhaust gas was drawn passing through burned gas collecting tube with temperature controlled at 120°C and then entering SHIMADZU NOA-7000 NOx-O_2 analyzer. In order to achieve high compressed ambient gas pressure at TDC before fuel injection, the tapered-type configuration of piston head fitted with small-volume combustion chamber was designed and shown in Figure 4.2.

Table 4.1 shows the experimental conditions. The orifice sizes D used were 0.180, 0.134 and 0.072 mm which had different nozzle hole lengths L of 0.5 mm and 0.8 mm for D=0.180 mm. The injection duration was set to be constantly at 2.1 ms. The operating gas condition at TDC was four studied points which all had identical estimated temperature of 890 K.

Table 4.1 Experimental conditions.

RCEM and Chamber specifications	
Piston speed	30 ms/comp. (~1200 rpm)
Bore x Stroke	30 x 150.5 mm
Displacement	425.32 cc
Compression ratio	12.1
Injection conditions	
Nozzle hole number	1 (all nozzles)
Orifice diameter D Nozzle hole length L (L/D)	0.180 mm, 0.5 mm, (2.77)
	0.134 mm, 0.5 mm, (3.73)
	0.180 mm, 0.8 mm, (4.44)
	0.072 mm, 0.5 mm, (6.94)
Fuel temperature	310 K (± 10 K)
Injection pressure	150 MPa
Injection duration	2.1 ms
Injected fuel amount	3.3 – 19.8 mg
Overall equivalence ratio	0.03 – 0.67
Fuel properties	
n-paraffins % mass	$C_{12}H_{26}$: 11.6% $C_{13}H_{28}$: 62.6% $C_{14}H_{30}$: 25.7%
Critical pressure	1.67 MPa
Critical temperature	677 K
Density at 300 K	745.3 kg/m^3
Surface tension at 300 K	20.8 mN/m
Surrounding conditions	
Oxygen	21%
Pressure (P_g)	3, 6, 9 and 12 MPa
Temperature (T_g)	890 K
Density (ρ_g)	11.7, 23.4, 35.2 and 46.8 kg/m^3

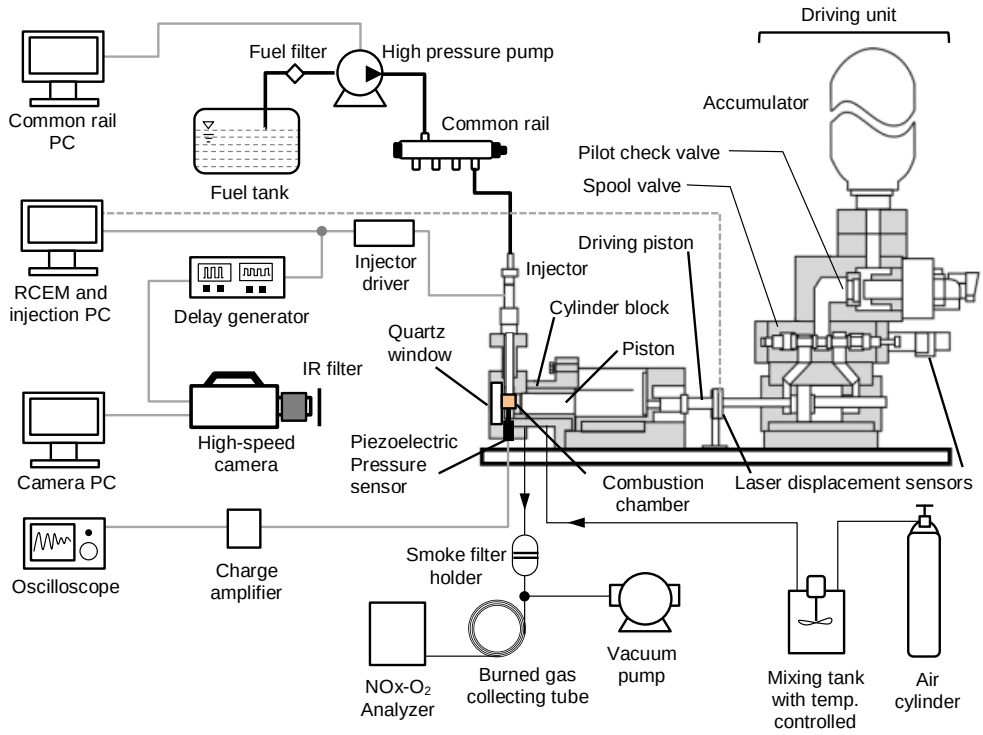

Figure 4.1 Experimental setup for high-speed imaging and emission measurement driven by rapid compression-expansion machine.

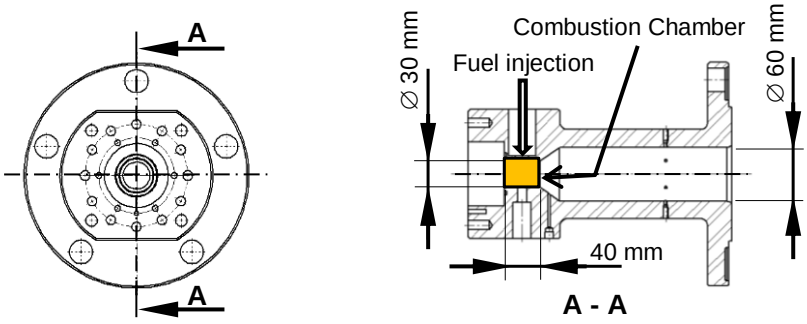

Figure 4.2 Combustion chamber for high temperature and high pressure test.

4.3 Results and Discussions

This section connects the previous section of spray characteristics to the combustion and emission characteristics. The last subsection presents the estimated equivalence ratio of vapor fuel/air mixture at start of combustion and the comparison of NOx formation between calculated and measured data.

4.3.1 In-Cylinder Pressure and Rate of Heat Release

The histories of in-cylinder pressure and apparent rate of heat release at the selected conditions of 11.7 kg/m^3 and 46.8 kg/m^3 are shown in Figure 4.3a and Figure 4.3d respectively. The injection starts at 0 ms time after start of injection ASOI and then lasts for 2.1 ms. Figure 4.3a presents low gas density condition of 11.7 kg/m^3 which corresponds to the surrounding gas pressure of 3 MPa. The ignition delay is relatively long due to low gas density affecting limited atomization process and entrained gas amount. It is detected to be 0.7-0.82 ms ASOI for all nozzle specifications. After 0.82 ms ASOI, the pressure rises sharply due to intensive combustion which is caused by large amount of fuel/air mixture accumulated during ignition delay period. The combustion pressure is clearly ranged according to injected fuel amount shown in Fig 3. Although, the beginning stage of combustion on both nozzles of D=0.180 mm shows relatively comparable level of pressure, the combustion peak pressure of the shorter hole length nozzle of D=0.180 mm (L/D=2.77) noticeably shows the lower level of pressure due to low amount of fuel delivery limiting the input energy for combustion. In apparent rate of heat release curve, the premixed combustion phase is clearly observed before 1 ms ASOI, as the first peak rises and sudden drops approximately at 1.4 ms ASOI for both large orifice nozzles of D=0.180 mm and D=0.134 mm. Comparing between identical orifice size nozzle of 0.180 mm, the longer hole length nozzle shows higher rate of heat release during premixed combustion phase due to longer ignition delay. After the premixed phase ends at 1.35 ms ASOI, the combustion enters the diffusion combustion phase which the rate of fuel delivery plays a dominant role. Both nozzles shows comparable manner of rate of heat release until the end of injection at 2.1 ms ASOI. It can be seen that the nozzle D=0.180 mm (L/D=2.77) shows a slightly lower pressure at late combustion phase, it is an indicator for the better soot oxidation process.

Figure 4.3b shows the cylinder pressure and apparent rate of heat release at the highest gas density conducted in this experiment of 46.8 kg/m^3 which is classified as high boosted surrounding gas. The cylinder pressure achieves 12 MPa at TDC position. It is seen that the premixed combustion phase is suppressed because the higher gas density enhanced entrainment and mixing processes and resulting in shorter ignition delay. The combustion of all nozzles is almost diffusion combustion. In the pressure rise curve, it is interesting that the ignition delay obviously becomes shorter for D=0.180 mm (L/D=2.77). This result is consistent with the rate of heat release beginning to rise earlier compared with that of D=0.180 mm (L/D=4.44). The combustion pressure of D=0.180 mm (L/D=2.77) shows a slightly higher throughout the injection duration. The peak pressure of 16.2 MPa is detected and almost equal for both nozzles of D=0.180 mm (L/D=2.77) and D=0.180 mm (L/D=4.44). However, slightly lower peaks of rate of heat release for the shorter hole length nozzle of D=0.180 mm (L/D=2.77) are observed

at 1.2 ms ASOI and 2.5 ms ASOI for the first and second peaks respectively. The shorter hole length nozzle is remarkable lower fuel delivery. Even though small amount of lower rate of fuel injection of the shorter hole length nozzle, the comparable peak pressure is reported. This is an evidence from our previous near-field spray characteristics that the D=0.180 mm (L/D=2.77) achieved the highest amount of fuel vapor produced and the highest entrained gas amount. It is noted that the vapor fuel highly produced was due to the enhanced mixing process by better atomization and high spray dispersion as it was reported in our previous study [10]. The rich mixture based on vapor phase fuel of the shorter hole length nozzle was obtained from the near-field experiment, far-field mixture is however believed to improve further and reach favorable condition for spontaneous ignition due to large entrained gas. Consequently, the richer vapor fuel/air mixture of shorter hole length nozzle of D=0.180 mm (L/D=2.77) evidently shows combustion proceeding more efficiently than that of the longer hole length nozzle at high boosted gas condition.

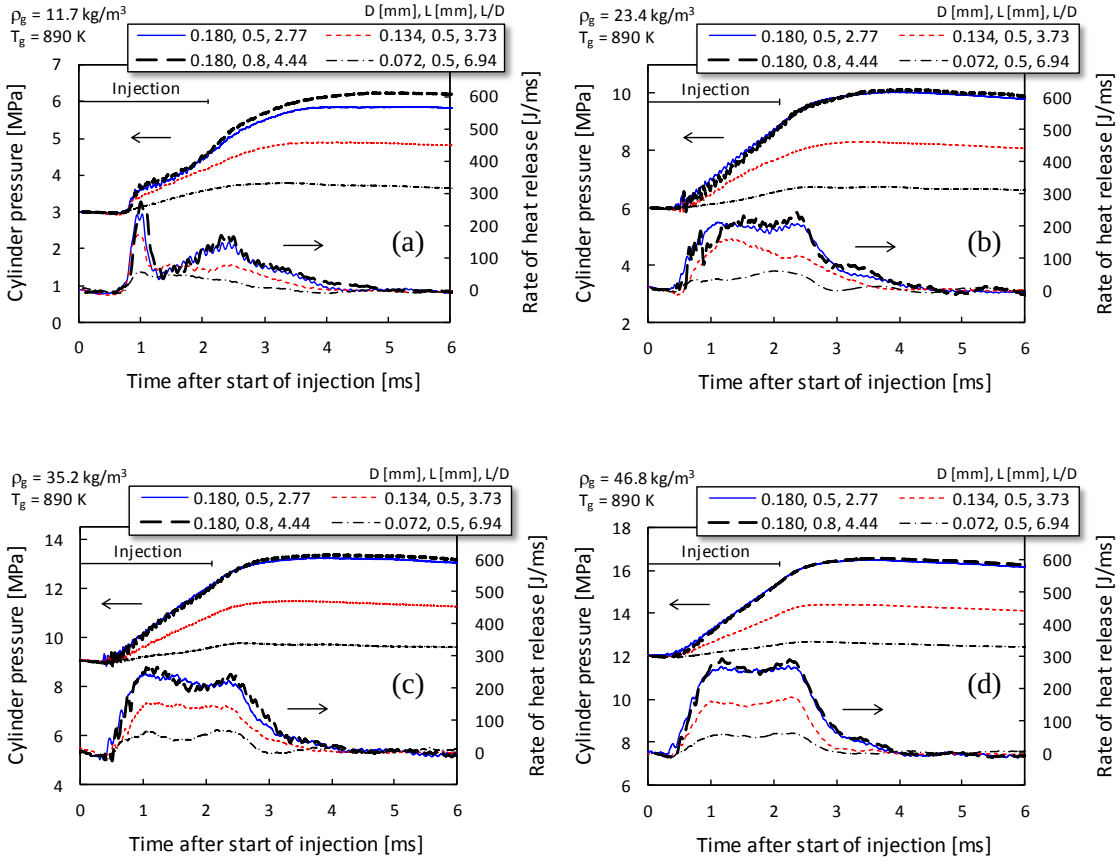

Figure 4.3 Comparison of cylinder pressure and rate of heat release at different nozzle specifications. Surrounding gas density: (a) 11.7 kg/m^3, (b) 23.4 kg/m^3, (c) 35.2 kg/m^3 and (d) 46.8 kg/m^3.

Figure 4.4 shows effect of surrounding gas density on apparent rate of heat release for each nozzle specification. In general, it is seen that an increase in gas density by increasing the gas pressure, peak of rate of heat release becomes higher. This is an evidence of combustion reaction is accelerated which produced more energy. Its tendency is found to suppress premixed combustion phase. This is because high density gas can be used to enhance atomization and mixing resulting in shorten ignition delay which can avoid accumulated fuel. In addition, higher gas density promotes soot oxidation that can be identified by a sharper declined slope after EOI.

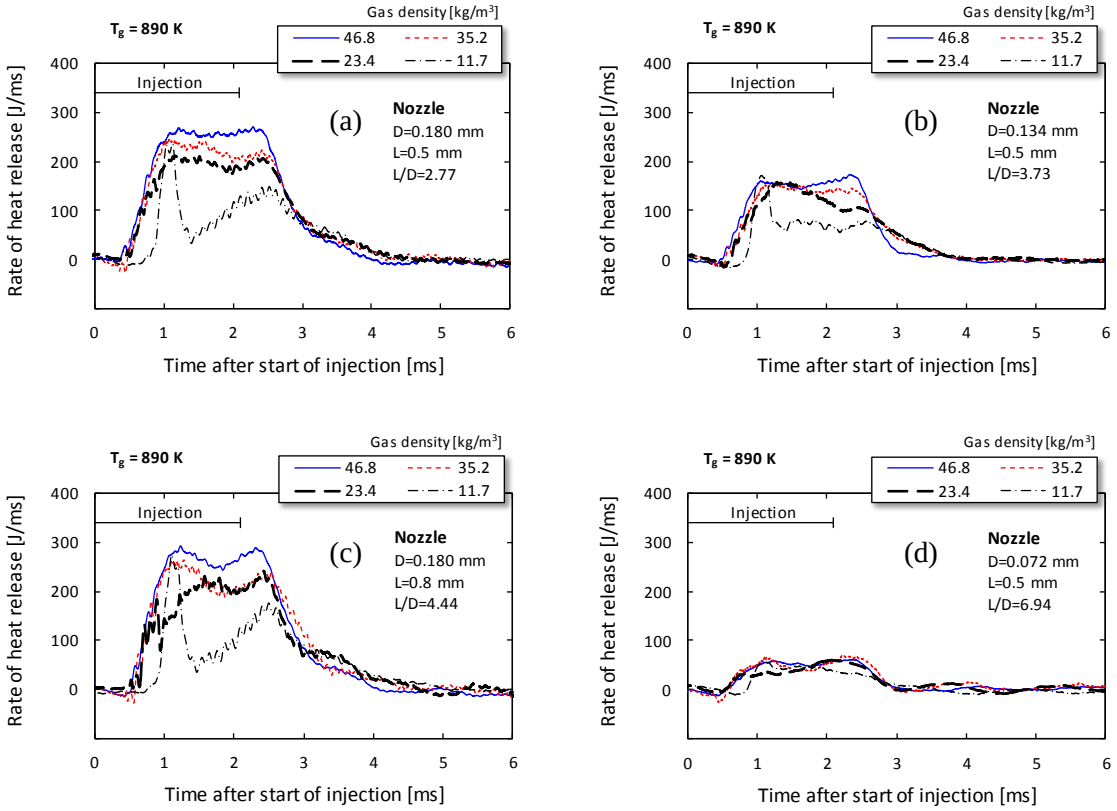

Figure 4.4 Rate of heat release as a function of surrounding gas density. Nozzle hole length to diameter ratio: (a) L/D=2.77, (b) L/D=3.73, (c) L/D=4.44, and (d) L/D=6.94.

4.3.2 Ignition Delay and Combustion Phasing

The ignition delay is considered from the time after start of injection to first rate of heat release becoming positive value after heat absorbed by the evaporating fuel. Combustion of a liquid fuel in an oxidizing gas actually happens in the gas phase. It is the vapor that burns, not the liquid. From now on, the equivalence ratio of vapor fuel/air mixture in the near field ϕ_{NF}

which was obtained from the previous near-field spray study and presented in section 3 is introduced for quantitative discussion on effect of near-field mixture preparation on combustion and emissions. According to Figure 3.25, it can be concluded that the lower equivalence ratio of vapor fuel/air mixture ϕ_{NF} is the consequence of the mixture under high surrounding gas density while the higher equivalence ratio of vapor fuel/air mixture is the result of the mixture under low surrounding gas density. Figure 4.5 clearly shows that ignition delay increases by an increase in equivalence ratio of vapor fuel/air mixture. It is found that the shortest igntion delay in all ranges of equivalence ratio of vapor fuel/air mixture is at the nozzle of D=0.180 mm (L/D=2.77) due to high entrainment. However, ignition delay tends to increase more significantly at high equivalence ratio. From our previous spray data, it was reported that the nozzle of D=0.180 mm (L/D=2.77) showed lack of atomization and vaporization processes at low gas density condition which is equivalent to high equivalence ratio in Figure 4.5.

The cumulative apparent heat release normalized by its maximum value which has similar characteristics to the burned mass fraction is used for determination of progress of combustion. Figure 4.6 shows combustion phases for different different nozzle specifications and surrounding gas conditions. It is found that the combustion duration dratically reduces as increasing in gas density. With identical orifice size nozzle of D=0.180 mm, the shorter hole length nozzle of L=0.5 mm shows the shorter combustion duration for all gas conditions compared with that of the longer hole length nozzle of L=0.8 mm. This is because preferable mixture is given to the shorter hole length nozzle as well as high entrained gas amount. Figure 4.7 shows 90% and 50% of total heat release for Figure 4.7a and Figure 4.7b respectively. In Figure 4.7b, all nozzle specifications shows comparable result of 1.7-1.8 ms ASOI at low equivalence ratio of vapor fuel/air mixture. It is fluctuated with in small range for the nozzle of D=0.134 mm and D=0.072 mm while rising tendency at increasing equivalence ratio of vapor fuel/air mixture is observed for the nozzle orifices of D=0.180 mm. This is because high amount of fuel injection needs longer times for proceeding combustion and improper mixture preparation in case of poor spray process. The shorter hole length nozzle of L=0.5 mm which corresponds to L/D=2.77 reaches the center of combustion faster compared with the longer hole length nozzle of L=0.8 mm in whole range of the equivalence ratio. This is owing to the better mixing process of the shorter hole length nozzle responsible for faster combustion. In Figure 4.7a, the variation turns upwards suggested that longer time is required to complete combustion as the equivalence ratio increases for the nozzle of D=0.134 mm and D=0.072 mm. For rough observation, the combustion using longer hole length nozzle spends longer time from start of injection through the end of combustion compared with that of the shorter one. It can be implied that the well-prepared mixture of the shorter hole length nozzle is supposed to continue with consistent manner throughout injection process, so that it achieves faster rate of combustion.

From this point, the soot emission produced by the longer hole length nozzle is expected to be higher.

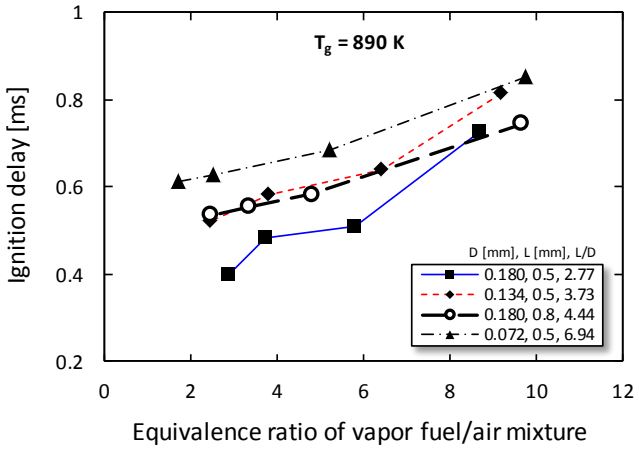

Figure 4.5 Variation of equivalence ratio of vapor fuel/air mixture with ignition delay for different nozzle specifications.

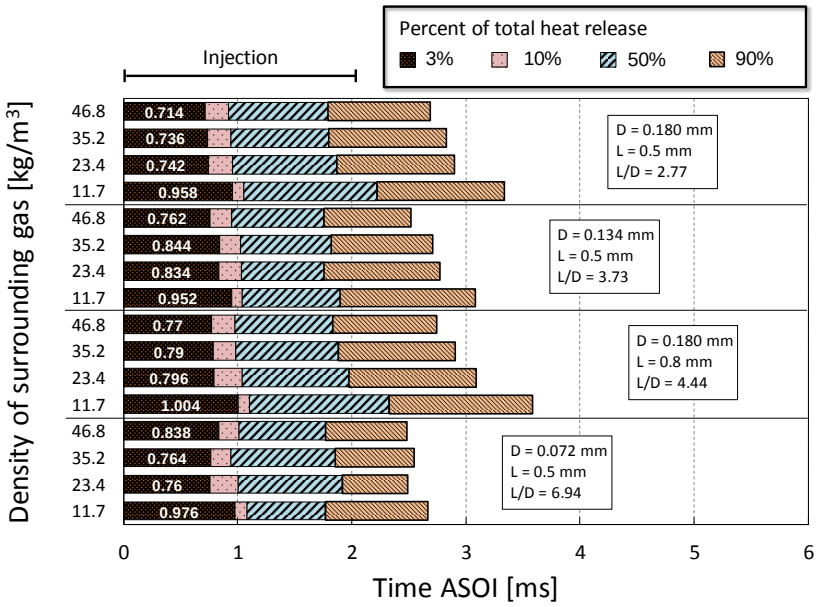

Figure 4.6 Combustion phases for different surrounding gas densities and different nozzle specifications.

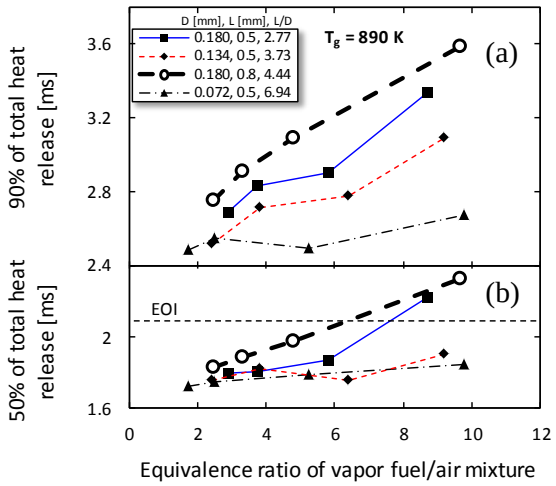

Figure 4.7 Influence of equivalence ratio of vapor fuel/air mixture on combustion phasing. (a) 90% of total heat release and (b) 50% of total heat release.

4.3.3 Soot and NOx Emissions

Soot emission is formed in the fuel-rich region of reaction zone and it is as a product of incomplete combustion. Soot amount in exhaust gas was found to influence by in-cylinder flow motion and flame-flame interaction [17] even in expansion stroke affecting radial flow velocity leading to enhanced soot oxidation. Soot produced in diesel combustion chamber consists of both formation and oxidation processes. Figure 4.8 shows soot emission with variation of equivalence ratio of vapor fuel/air mixture in the near field ϕ_{NF} for different nozzle specifications. For small orifice size nozzle of D=0.072 mm (L/D=6.94) and D=0.134 mm (L/D=3.73), the soot fluctuates with a limited range of 0.001-0.002 at the equivalence ratio of 1.8-6.5. As an increase in the equivalence ratio, the soot generated by the nozzle D=0.134 mm (L/D=3.73) considerably increases due to richer mixture leading to incomplete combustion while the nozzle D=0.072 mm (L/D=6.94) still keeps similar low soot level. The possible reason is that the smallest orifice nozzle of 0.072 mm delivers very small injected fuel amount with a small orifice size producing lean mixture in downstream region. The soot formation is possible to be slowdown due to high oxygen content in the mixture and the soot oxidation is promoted in the late phase of combustion. Comparing between the identical orifice size nozzle of D=0.180 mm but different hole length of L=0.5 mm and L=0.8 mm, the longer hole length nozzle produces larger amount of soot at the equivalence ratio of 2.2-8.2. The shorter hole length nozzle has a tendency to produce more soot as the equivalence ratio increases beyond 8.5 where an intersection point of both slopes exists. This result of different hole length effect is consistent with the previous subsection of discussion about combustion characteristics. The shorter hole

length nozzle has shown the combustion improved significantly compared with the longer one at elevated gas density which condition is equivalent to low equivalence ratio of vapor fuel/air mixture in Figure 4.8. However, it tends to be the significantly produced amount of soot at high equivalence ratio because the mixing process turns to be weaker, see Figure 3.25 at low gas density of 10-20 kg/m^3.

Figure 4.9 reports NOx emission correlated with equivalence ratio of vapor fuel/air mixture in the near field ϕ_{NF}. In general, the NOx decreases with increasing the equivalence ratio. On the other hand, the leaner mixture due to high entrainment enhances the combustion resulting in higher combustion temperature and larger amount of NOx is produced. For small orifice size nozzle of D=0.072 mm (L/D=6.94) and D=0.134 mm (L/D=3.73), the NOx emission linearly increases with decreasing the equivalence ratio. However, the D=0.134 mm (L/D=3.73) produces larger amount of NOx, as a result of higher rate of heat release and the higher expected flame temperature compared with nozzle of D=0.072 mm. Comparing between identical orifice size nozzle of D=0.180 mm, the shorter hole length nozzle produces higher amount of NOx. This is because from the previous spray study, the shorter hole length nozzle achieved the highest amount of entrained gas among four nozzle specifications, so that the combustion proceeded efficiently as discussed in subsection 4.2.

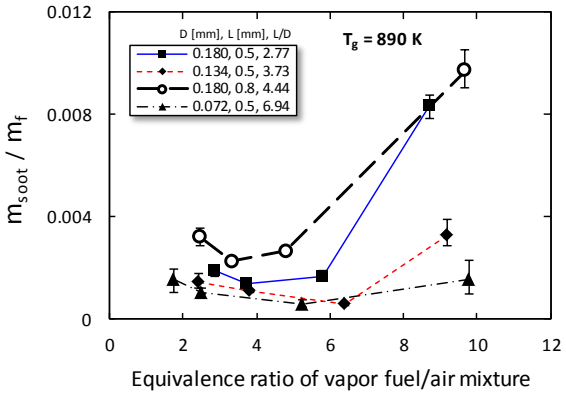

Figure 4.8 Soot mass normalized by injected fuel amount versus equivalence ratio of vapor fuel/air mixture.

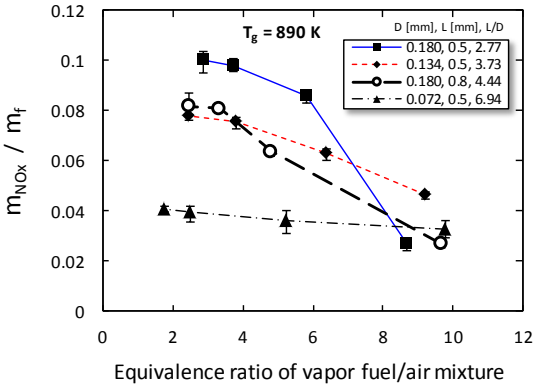

Figure 4.9 NOx mass normalized by injected fuel amount versus equivalence ratio of vapor fuel/air mixture.

4.3.4 Flame Temperature and KL Factor

For typical exhaust of current diesel engine consisting of NOx and soot. Flame temperature is a key parameter for reaction rate of combustion and formation mechanism of NOx. The direct photo is used to analyze by means of two-color method [12, 13] to obtain flame temperature and

KL factor which corresponds to soot concentration contained in the optical path. The two-color method is an optical thermometry technique that makes use of the presence of soot within a flame. Figure 4.10 shows the histories of flame temperature and integrated KL factor located at upper and lower part of each gas condition respectively. The gas density of 11.7 kg/m^3 is shown in Figure 4.10a while the 46.8 kg/m^3 is shown in Figure 4.10b. The flame temperautre T_f is the spatially averaged value inside the luminous flame area at instantenous time while the integrated KL factor is the summation of all KL values presence in the luminous flame. In Figure 4.10a, it can be seen that the luminous flame starts right after 1 ms ASOI. This is just after the cylinder pressure suddenly rises up and ignition delay is detected at 0.75 ms ASOI for nozzle of D=0.180 mm (L/D=2.77), see Figure 4.3a. The nozzle of D=0.180 mm (L/D=2.77) shows the fastest initial luminous flame which this result is consistent with the detected ignition delay shown in Figure 4.5. At identical orifice size nozzle of D=0.180 mm, the shorter hole length nozzle exhibits slightly higher flame temperature compared with that of the longer one for whole flame duration. The peak of averaged flame temperature of 2255 K is indicated at the shorter hole length nozzle of D=0.180 mm (L/D=2.77) while the lowest one of 2200 K is found at the smallest orifice size nozzle of D=0.072 mm (L/D=6.94). One point is that the fashion of the flame temperature is not the same as the rate of heat release curve that contains premixed combustion incidence without the radiation from soot particles. With integrated KL factor, it rises significantly from the beginning for the shorter hole length nozzle and reaches its peak at 3 ms ASOI. The unique feature for the longer hole length nozzle compared with that of the shorter one is that the flame temperature is lower with higher KL and the peak is shifted to later 3.9 ms ASOI. The marker for soot oxidation is a declined slope which is after 3 ms ASOI for the shorter hole length nozzle. The soot oxidation performs earlier with lower oxidation rate for the shorter hole length nozzle. However, the end of flame is almost similar at 6 ms ASOI. This would be the result of poor mixing given from the shorter hole length nozzle at low surrounding gas density condition which is unprofitable to the soot oxidation. Figure 4.10b at 46.8 kg/m^3, the flame temperature and integrated KL factor development are completely different from those presense at lower gas density of 11.7 kg/m^3. This high gas density enhances the spray formation leading to stimulation of combustion. The fastest flame appearance is again found at the nozzle of D=0.180 mm (L/D=2.77). The flame duration is found to be longer for the longer hole length nozzle which ends at 3.5 ms ASOI while the shorter hole length nozzle ends at 3 ms ASOI. The integrated KL factor of the shorter hole length nozzle declines suddenly and the shorter flame duration compared with the longer one. From the calculated flame tempeature and integrated KL factor, it can be used to support the discussion in previous subsection of measured soot emission. The reason of lower amount of soot produced by the shorter hole length nozzle of D=0.180 mm (L/D=2.77) is due to favorable mixture, higher flame temperature, shorter flame

duration and soot oxidation performed intensively. This reason of higher flame temperature of the shorter hole length nozzle can express the NOx emission in the same manner. The spatial evolution of flame temperature and a single instantenous KL factor for different nozzle specifications and surrounding gas densities are tabulated in Figure 4.11. In general, start of flame is fast at higher gas density of 46.8 kg/m^3 and the flame temperature spatially varied between 2000-2400 K. Since the elevated gas density essentially promotes fuel/air mixing and accelerates reaction, flame duration is significantly shortened at gas density of 46.8 kg/m^3 and flame area is confined which can be said that the combustion efficiently completed within a limited zone. This enhanced combustion under higher gas density obviously supports the discussion in measured soot emission. Comparing the idential orifice size nozzle of D=0.180 mm, the shorter hole length nozzle clearly reveals the start of flame faster prominently at gas density of 46.8 kg/m^3. This can refer to the shorter ignition delay which is indicated to be the shorter hole length nozzle. Additionally, the high level of flame temperatuare and its distribution are an evidence that the efficient combustion is indicated to the shorter hole length nozzle. Although the lower injected fuel amount for the shorter hole length nozzle, the combustion is drastically promoted due to sufficient mixture with high dispersion and high entrainment. This information supports the result of cylinder pressure rising and reaching comparable level of peak pressure with the longer hole length nozzle at gas density of 46.8 kg/m^3.

Figure 4.12 shows the averaged flame temperature that the spatially averaged flame temperature in an instantaneous time is again averaged over the flame period plotted against equivalence ratio of vapor fuel/air mixture in the near field ϕ_{NF}. It is noted that the combustion is known to be taken place in the gas phase. Due to the relatively higher equivalence ratio of vapor fuel/air mixture with higher entrainment quantified at near-field region of the shorter hole length nozzle of D=0.180 mm (L/D=2.77), it is found to be preferable to combustion, as it shows highest averaged flame temperature for whole range of equivalence ratio of vapor fuel/air mixture excepting uncertain tendency at equivalence ratio of vapor fuel/air mixture rising above 8. Figure 4.13 shows the variation of averaged flame temperature with NOx emission. The relation is as expected that NOx emission increases with an increase in flame temperature. High temperature zones within the flame cause nitrogen molecules in the air to separate, allowing them to combine with oxygen, which leads to the formation of NOx. The amount of thermal NOx formed actually depends largely on the temperature of the flame and residence time. It is found that the NOx emission is not only governed by the flame temperature but also the minor influences are observed such as size of reaction zone and flame duration.

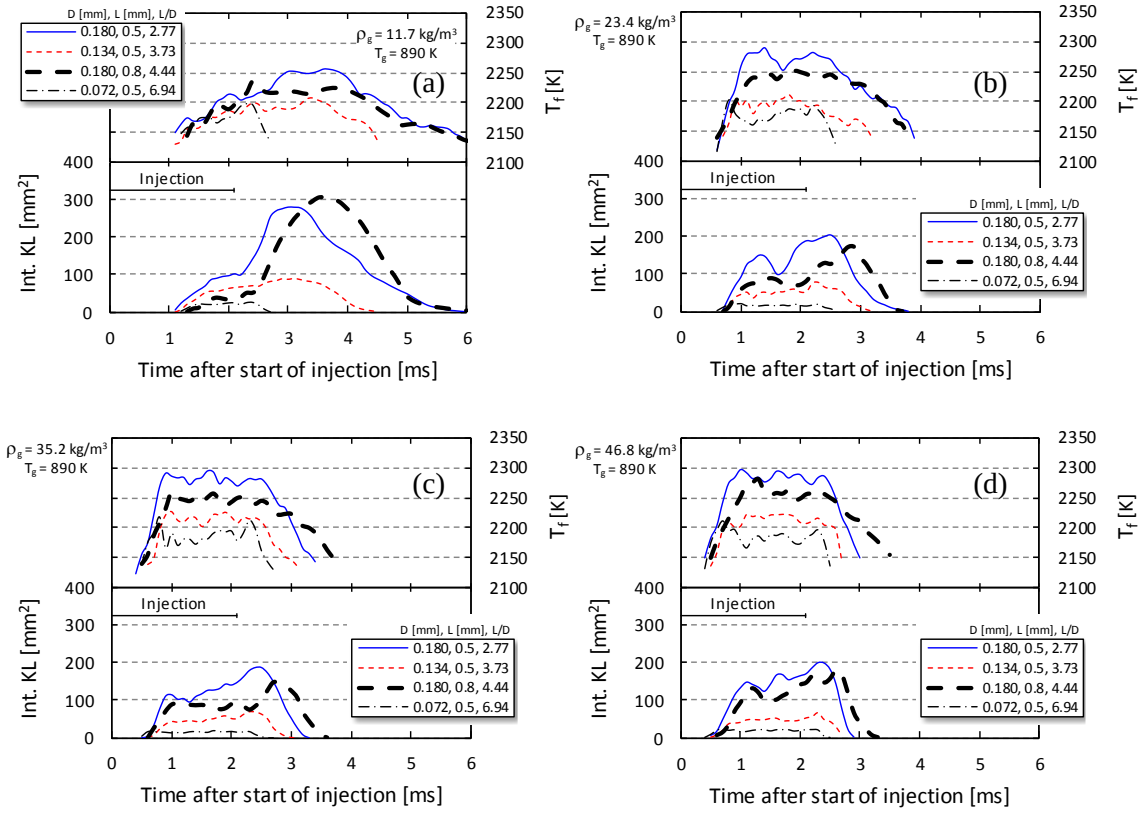

Figure 4.10 Histories of flame temperature and integrated KL factor. Surrounding gas density: (a) 11.7 kg/m^3, (b) 23.4 kg/m^3, (c) 35.2 kg/m^3 and (d) 46.8 kg/m^3.

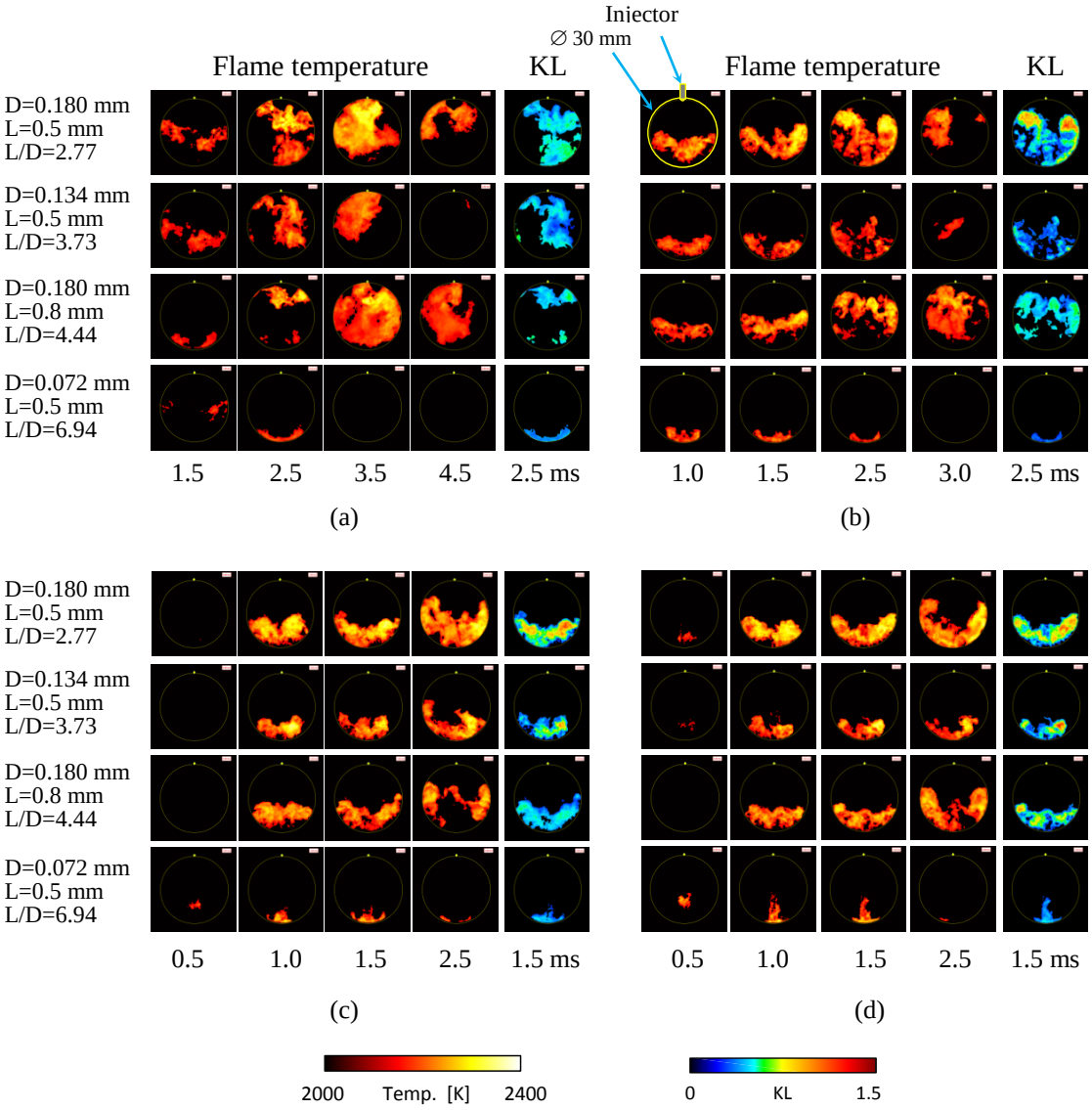

Figure 4.11 Temporal evolution of flame temperature and an instantaneous KL factor analyzed based on 2-color method. Surrounding gas density: (a) 11.7 kg/m^3, (b) 23.4 kg/m^3, (c) 35.2 kg/m^3 and (d) 46.8 kg/m^3.

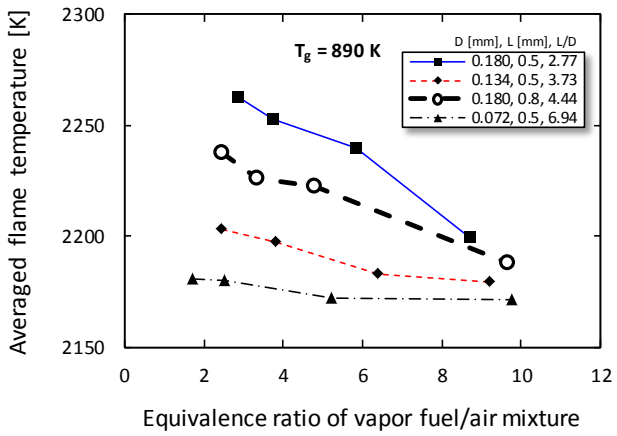

Figure 4.12 Effect of equivalence ratio of vapor fuel/air mixture on averaged flame temperature for four different nozzle specifications.

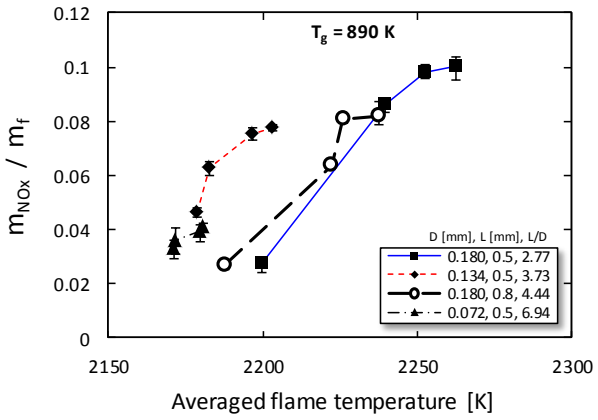

Figure 4.13 Relation between averaged flame temperature and NOx emission.

4.4 Evaluation of NOx Formation

In diesel combustion, the nitric oxides NOx consists of NO and NO_2 which is formed in the flame front and in the post-flame zone. Thermal NOx is the most dominant pathway which is formed when nitrogen and oxygen within the combustion gas at a relatively high temperature above 1800 K [14]. This study employs Zeldovich mechanism [15] for thermal NO formation. The NOx and NO terms may be used interchangeably. In calculation, the chemical equilibrium approach of the system containing C, H, O and N atoms, other than NO, is used to obtain the equilibrium concentration of product gases at given mixture composition and the system temperature and pressure. For simplicity, it is reasonable to assume that the fuel/air mixture is perfectly mixed and ignition occurs at spray tip with ignoring the effect of either spray or flame

wall impingement. Equivalence ratio presented in section 3 is the equivalence ratio of vapor fuel/air mixture that was considered in a limited area which is 20-mm near field from nozzle exit ϕ_{NF}. At this time, we need to know that quantity when the spray penetrates farther downstream using the measured near-field spray characteristics such as liquid length, liquid and vapor cone angles until it reaches ignition time which is equal to the measured ignition delay. Since an averaged velocity decay of spray at centerline can be estimated using Musculus's jet model [16], the spray penetration and spatially mixture distribution for each elapsed time can then be derived. Thus, once the ignition delay is known associated with near-field spray characteristics, the equivalence ratio of vapor fuel/air mixture at start of combustion $\phi_{\mathrm{vp,soc}}$ can eventually be obtained at corresponding penetration. Figure 4.14 shows the relation between ϕ_{NF} and $\phi_{\mathrm{vp,soc}}$. It suggests that the mixture becomes drastically learner when the spray penetrates up to ignition time. The $\phi_{\mathrm{vp,soc}}$ is used as the mixture composition just before the ignition for NO formation. The system temperature and pressure are the values considered at TDC conditions. The NO formation is supposed to primarily confine in the flame and expand through the chamber volume. The averaged flame temperature analyzed based on 2-color method is used to represent the burned gas temperature while the flame duration is assumed to be a residence time for NO formation.

Figure 4.15 shows the comparison between measured NOx and thermal NO calculated using the method described above plotted against the equivalence ratio of vapor fuel/air mixture at start of combustion $\phi_{\mathrm{vp,soc}}$. The relationship between the measured NOx emission and equivalence ratio of vapor fuel/air mixture under both schemes, those are at near field shown in Figure 4.9 and at start of combustion shown in Figure 4.15a exhibits similar fashion. It is found that an increase in equivalence ratio of vapor fuel/air mixture caused by poor atomization and lack of entrained gas resulting in lower flame temperature sequentially slowdown NOx formation. The calculated NO emission shows a significant relation with $\phi_{\mathrm{vp,soc}}$ as shown in Figure 4.15b. Although, several factors including spatial and temporal changes in flame temperature and ambiguous identification of NO formation zone may cause discrepancies between measured and calculated NO emissions, the consistency between them can be observed.

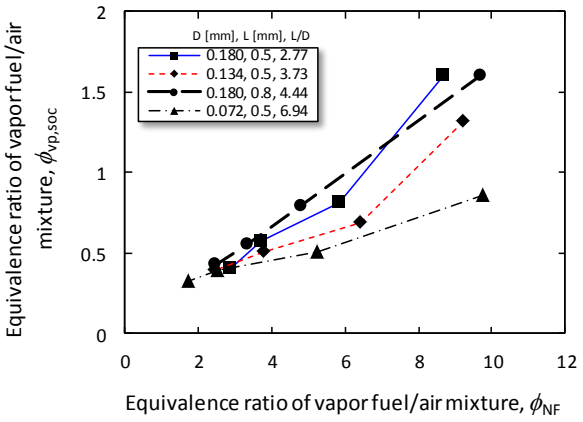

Figure 4.14 Relation between equivalence ratio of vapor fuel/air mixture determined at near-field region ϕ_{NF} and at start of combustion $\phi_{vp,soc}$.

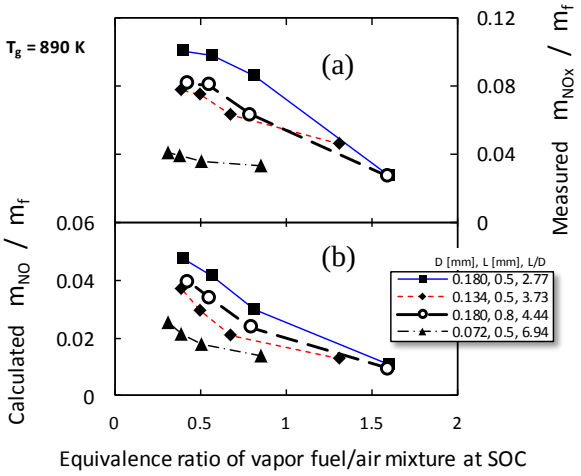

Figure 4.15 Effect of the equivalence ratio of vapor fuel/air mixture at start of combustion $\phi_{vp,soc}$ on NOx emission. (a) measurement and (b) calculation based on extended Zeldovich mechanism.

Flame temperature analyzed based on two-color method can give both spatial and temporal resolutions. In order to consider both effect on emissions, the averaged flame temperature $T_{2C,avg}$ and the maximum flame temperature $T_{2C,max}$ are determined. Figure 4.16a shows comparison between averaged and maximum flame temperature for different nozzle specifications. It is seen that in between 20-40 K the maximum flame temperature is higher than the averaged flame temperature On the other hands, Figure 4.16b shows comparison between averaged flame

temperature $T_{2C,avg}$ and adiabatic flame temperature T_{ad}. For this comparison, it gives large difference between those that the adiabatic flame temperature is about 270-520 K higher than the averaged flame temperature.

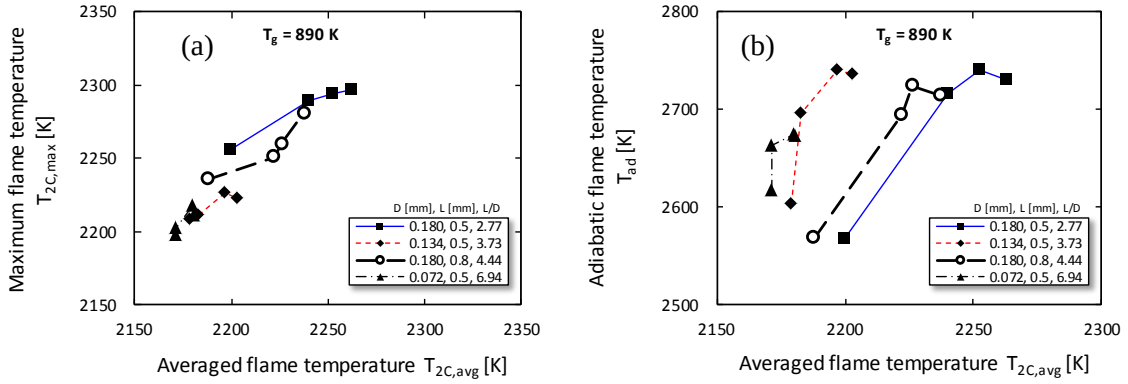

Figure 4.16 Comparison of flame temperatures. (a) $T_{2C,avg}$ vs. $T_{2C,max}$ and (b) $T_{2C,avg}$ vs. T_{ad}.

Figure 4.17 shows comparison of NOx emission between measurement and calculation. The calculation is carried out based on two assumptions of flame temperature T_f which are the two-color method flame temperature T_{2C} mentioned above, and the adiabatic flame temperature T_{ad}. In this study, although the surrounding gas temperature is kept constant at 890 K, wide-range gas pressures of 3-12 MPa are prepared before fuel injection and combustion taking place. In such large variation of pressure, it needs to be taken into consideration as the combination of radicals occurs faster at high pressure combustion [18]. This can influence significant portion of energy from combustion and resulting in product temperature. The constant-pressure adiabatic flame temperature T_{ad} is calculated by the method based on chemical equilibrium state. The equilibrium mole fractions of 10 combustion product gases such as CO_2, CO, O_2, O, NO, N_2, H, H_2, OH, and H_2O at given initial temperature, pressure and fuel/air mixture are firstly computed using the equilibrium constants obtained from [19]. The initial temperature and pressure of the mixture are considered at the start of heat release which is essentially close to the TDC surrounding gas condition while the equivalence ratio of vapor fuel/air mixture at start of combustion $\phi_{vp,soc}$ is used as the initial fuel/air mixture. Based on the thermodynamic properties of air and combustion products obtained from [20], and those for diesel fuel obtained from [21], the flame temperature starts estimating from 2000 K and then iteratively updated until the enthalpy of the combustion products matches the enthalpy of the unburned mixture. Under $T_{2C,avg}$ assumption, the result shows significantly underestimated. The data set of D=0.134-0.180 mm is displaced from that of D=0.072 mm. There is a possible reason that two-color method flame temperatures of D=0.134-0.180 mm are suspected to be low

which values are farther than that of the actual flame. The calculated NO amount is found to increase when using maximum flame temperature $T_{2C,max}$, but the results are still located in the underestimated side. When the NO formation is calculated based on T_{ad} the results are shifted to a slightly overestimated side. As it is expected that T_{ad} is actually somewhat higher than $T_{2C,avg}$ and $T_{2C,max}$, the corresponding NO emission obviously increases. The variations of flame temperature based on those assumptions are 2175-2265 K for $T_{2C,avg}$ and 2550-2750 K for T_{ad} which is approximately 430 K for an averaged difference. Under T_{ad} assumption, the results are more linearly predicted compared with the measured data. Although both assumptions of flame temperature used for NO formation are not properly fitted to the measured data, it suggests that using T_{ad} is an appropriate assumption which consequently provides better accuracy. Advantage of using T_{ad} is due to its simple to obtain without any setup of high speed flame imaging and two-color calibration devices.

Figure 4.18a shows relationship between adiabatic flame temperature T_{ad} and measured soot emission. It can be seen that soot amount shows unclear correlation with adiabatic flame temperature especially for small orifice size nozzle of D=0.072-0.134 mm. For small orifice size nozzle, the injected fuel amount is low and fuel/air mixture just before ignition is diluted by entrained gas. The soot emission is determined by the balance between the formation and oxidation of soot. Both formation and oxidation of soot are affected by temperature and oxygen concentration. Thus, the soot emission in exhaust is unreasonable to be expressed by only adiabatic flame temperature. Moreover, balance of formation and oxidation of soot may be changed when the orifice diameter of nozzle is reduced. For NOx emission shown in Figure 4.18b, strong correlation is observed for all nozzle specifications as NOx proportionally increases with an increase in the flame temperature particularly for large orifice size nozzle of D=0.134-0.180 mm. However, a small nozzle orifice size of D=0.072 mm displays less sensitive to the flame temperature due to lack of fuel amount participating in combustion, sequentially resulting in small variation of flame temperature.

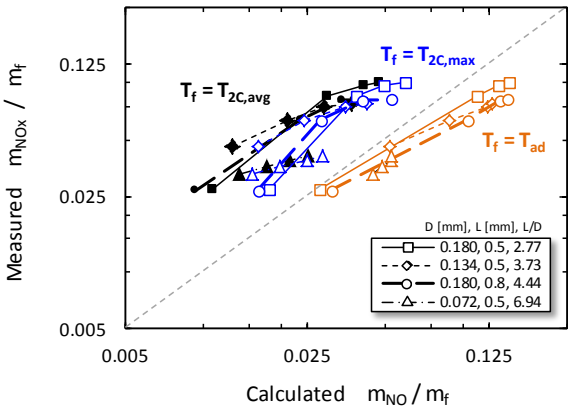

Figure 4.17 Comparison of NOx emission between measurement and calculation using different assumptions of flame temperature T_f.

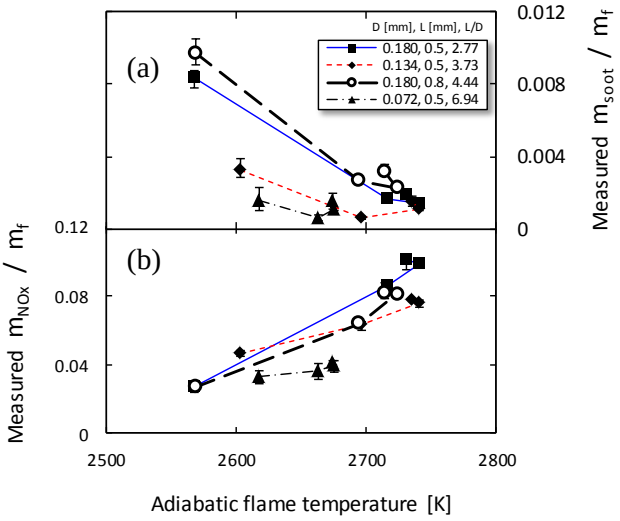

Figure 4.18 Variation of adiabatic flame temperature with soot and NOx emissions. (a) measured soot and (b) measured NOx emissions.

4.5 Conceptual Model

The liquid-gas phases of diesel spray under wide range of gas densities of 11.7-46.8 kg/m^3 have been visualized and described in chapter 3. The corresponding fuel/air mixture quantified in the near field has been extended to the farther downstream at start of combustion and the combustion and emission characteristics have then been shown in this chapter. Figure 4.19 shows a simple conceptual model revealing relation between fuel/air mixture and combustion processes for low and high surrounding gas density conditions which is 11.7 kg/m^3 and 46.8

kg/m^3 respectively. Figure 4.19a and Figure 4.19b depict graphical spray, fuel/air mixture and combustion flame while Figure 4.19c and Figure 4.19d show corresponding rate of heat release and measured flame area respectively. At 20-mm near field from nozzle tip, significant leaner fuel/air mixture ϕ_{NF} is detected in the high surrounding gas density condition compared with that of the low one. This is because an intense interaction between high gas density and injected liquid fuel promotes atomization and high spray dispersion is found which result in enhanced mixing process. From analysis, it was revealed that the high surrounding gas condition showed higher entrained gas amount which is one of the factors that stimulates vaporization and improves mixing process. At start of combustion where ignition taking place, the fuel/air mixture ϕ_{SOC} is estimated and the mixture with high surrounding gas density still shows leaner mixture. Due to high entrained gas amount and preferable mixture, ignition occurs faster and reaction is accelerated as can be seen in Figure 4.19c. The shorter ignition delay and significantly higher rate of heat release are indicated at high surrounding gas density condition. Figure 4.19d shows that the detected flame area corresponding to the reaction zone is much smaller for high surrounding gas density condition. It means that the combustion is taken place and completed in a confined area. It is found that the combustion with the mixture prepared under high surrounding gas density promotes some particular levels of soot oxidation process.

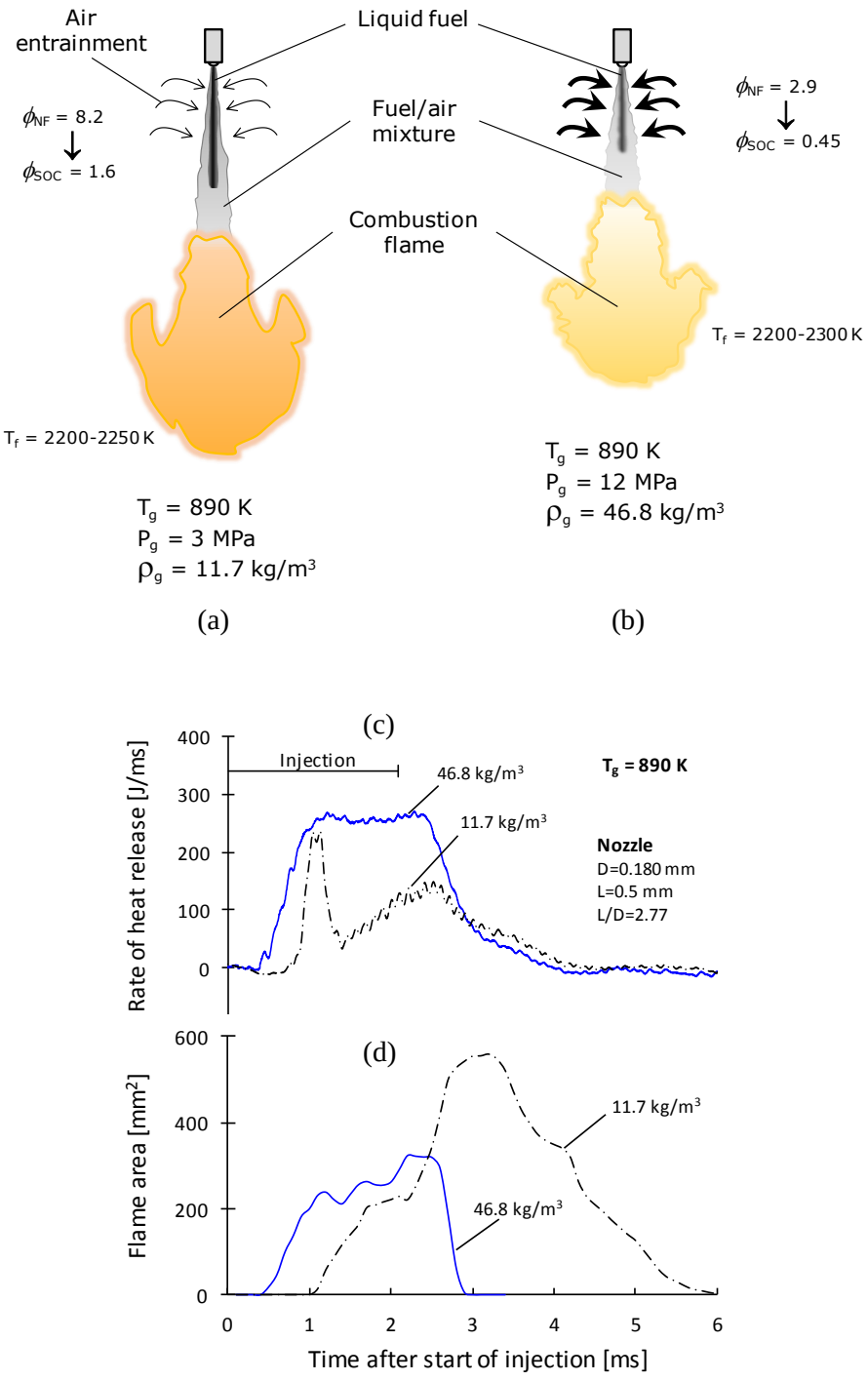

Figure 4.19 Conceptual model of diesel spray combustion for different surrounding gas density conditions. (a) 11.7 kg/m^3 and (b) 46.8 kg/m^3.

4.6 Conclusions

The relation between spray characteristics in near field region and combustion characteristics in diesel spray flame was investigated under wide range of operating ambient gas densities of 11.7-46.8 kg/m^3. High-speed imaging arrangement with soot and NOx emissions were measured. An estimated NO formation based on Zeldovich mechanism was also demonstrated and compared with the measured data. The main results of this work are listed below:

1. The premixed combustion phase was observed at low gas density of 11.7 kg/m^3 and substantially suppressed by increasing gas density. The is becuase the shorter ignition delay, the lower amount of fuel is accumulated. At elevated surrounding gas density, entrainment of surrounding gas into a spray drastically increased. The higher amount of entrained gas was sequentially helped improve combustion.
2. In near-field mixture behavior, with identical orifice size nozzle, the shorter hole length nozzle of D=0.180 mm (L=0.5 mm) provided the shorter liquid length, higher spray dispersion, higher entrainment and richer vapor fuel compared with the longer hole length nozzle of D=0.180 mm (L=0.8 mm). The near-field mixture behavior was found to continuously proceed up to upstream of ignition and throughout injection period as it was responsible for shorter ignition delay and combustion occurring more efficiently with higher flame temperature.
3. The lower amount of soot produced by the shorter hole length nozzle of D=0.180 mm (L=0.5 mm) compared with that of the longer one is due to the better mixture preparation, higher flame temperature and shorter flame duration. In addition, the oxidation of soot was intensively stimulated at late combustion phase.
4. NOx emission was found to decrease with equivalence ratio of vapor fuel/air mixture increased and relatively showed an inverse trend with soot emission. This was because the richer mixture caused by lack of entrainment of surrounding gas into a spray eventually resulted into weak reaction and lower flame temperature.
5. The measured NOx emission showed a strong function of adiabatic flame temperature. By increasing the adiabatic flame temperature, NOx progressively increased for large orifice size nozzles of D=0.134-0.180 mm, and gently increased for a small one of D=0.072 mm. In spite of that, the measured soot emission showed an unclear correlation to both equivalence ratio of vapor fuel/air mixture and adiabatic flame temperature.
6. The combustion and emission characteristics showed significant correlation with near-field spray behavior, particularly the influence of amount of fuel in vapor phase and entrainment of surrounding gas into the spray. The proper mixture preparation with high entrainment

was declared to be a promising factor for efficient combustion with low soot emission at high boosted gas condition.

Bibliography

[1] Giménez, B., Tinaut, F., Melgar, A., and Payri, R., "Effects of the Operating Variables and Atomization Parameters on Diesel Spray Characteristics by means of a Transient Evaporative Spray Atomization Model," SAE Technical Paper 2004-01-2013, 2004.

[2] M. Vijay Kumar, A. Veeresh babu, P. Ravi Kumar, and T. Manoj Kumar Dundi, "Influence of Different Nozzle Hole Orifice Diameter on Performance, Combustion and Emissions in a Diesel Engine," Australian Journal of Mechanical Engineering, Volume 17, 2019.

[3] Baumgarten, "Mixture Formation in Internal Combustion Engines," Springer, (2006).

[4] Seang-wock Lee, Daisuke Tanaka, Jin Kusaka, Yasuhira Daisho, "Effects of Diesel Fuel Characteristics on Spray and Combustion in a Diesel Engine," JSAE Review. Volume 23, Issue 4, Pages 407-414, 2002.

[5] İsmetÇelıkten, "An Experimental Investigation of the Effect of the Injection Pressure on Engine Performance and Exhaust Emission in Indirect Injection Diesel Engines," Applied Thermal Engineering, Volume 23, Issue 16, Pages 2051-2060, 2003.

[6] Kobori, S., Kamimoto, T., and Kosaka, H, "Ignition, Combustion and Emissions in a DI Diesel Engine Equipped with a Micro-Hole Nozzle," SAE Technical Paper 960321, 1996.

[7] Sibendu Som, Anita I.Ramirez, Douglas E.Longman, Suresh K. Aggarwal, "Effect of Nozzle Orifice Geometry on Spray, Combustion, and Emission Characteristics under Diesel Engine Conditions," Volume 90, Issue 3, Pages 1267-1276, 2011.

[8] W. Zhang, K. Nishida, J. Gao, D. Miura, "An Experimental Study on Flat-Wall-Impinging Spray of Microhole Nozzles under Ultra-High Injection Pressures," Proc IMechE Part D: J Automob Eng, Pages 1731-1741, 2008.

[9] Khalid, A., Hayashi, K., Kidoguchi, Y., and Yatsufusa, T., "Effect of Air Entrainment and Oxygen Concentration on Endothermic and Heat Recovery Process of Diesel Ignition," SAE Technical Paper 2011-01-1834, 2011.

[10] Shinabuth, D., Nagasawa, T., Sato, S. and Kosaka, H., "Study on Effect of Nozzle Hole Length to Diameter Ratio on Near-Field Diesel Spray Characteristics at High Density Condition," International Journal of Automotive Engineering, Volume 11, Issue 4, Pages 159-168, 2020.

[11] Kobori, S. and Kamimoto, T., "Development of a Rapid Compression-Expansion Machine Simulating Diesel Combustion," SAE Technical Paper 952514, 1995.

[12] Takeyuki Kamimoto, Noboru Uchida, Tetsuya Aizawa, Katsufumi Kondo, Tatsuya Kuboyama, "Diesel Flame Imaging and Quantitative Analysis of In-Cylinder Soot

Oxidation," IJER, Volume 18, Issue 5-6, Pages 422-435, 2016.

[13] Yukio Matsui, Takeyuki Kamimoto and Shin Matsuoka, "A Study on the Time and Space Resolved Measurement of Flame Temperature and Soot Concentration in a D.I. Diesel Engine by the Two-Color Method," SAE Transactions, Volume 88, Section 2: 790267–790526, Pages 1808-1822, 1979.

[14] S. C. Hill and L. Douglas Smoot, "Modeling of Nitrogen Oxides Formation and Destruction in Combustion Systems," Progress in Energy and Combustion Science, Volume 26, Issue 4-6, Pages 417-458, 2000.

[15] Y.B. Zel'dovich, "The Oxidation of Nitrogen in Combustion Explosions," Acta Physicochimica U.S.S.R. Volume 21, Pages 577–628, 1946.

[16] Musculus, M. and Kattke, K., "Entrainment Waves in Diesel Jets," SAE Int. J. Engines 2(1):1170-1193, 2009.

[17] Hesameddin Fatehi, Tommaso Lucchini, Gianluca D'Errico, Anders Karlsson, Xue-Song Bai and Öivind Andersson, "Effect of In-cylinder Flow Structures on Late Cycle Soot Oxidation in a Quiescent Heavy-duty Diesel Engine," Combustion Science and Technology, 2019.

[18] Sara McAllister; Jyh-Yuan Chen; A. Carlos Fernandez-Pello, "Fundamentals of Combustion Processes," Chapter 2, Mechanical Engineering Series, Springer, Pages15-47, 2011.

[19] Olikara, C. and Borman, G., "A Computer Program for Calculating Properties of Equilibrium Combustion Products with Some Applications to I.C. Engines," SAE Technical Paper 750468, 1975.

[20] Gordon, S., and McBride, B. J., "Computer Program for Calculation of Complex Chemical Equilibrium Composition, Rocket Performance, Incident and Reflected Shocks, and Chapman-Jouguet Detonations," NASA SP-273, 1971.

[21] Ferguson, C.R., "Internal Combustion Engines", Wiley, 1986.

CHAPTER 5
CONCLUSIONS AND FUTURE WORKS

5.1 Conclusions

This chapter is the final conclusion of this dissertation.

1. At high boosted gas conditions, faster liquid vaporization with higher spray dispersion was found and the fuel/air mixture was significantly diluted by entrainment of surrounding gas. Under this mixture condition, ignition took place much faster and it significantly accelerated reaction.
2. With identical orifice diameter of 0.180 mm, the shorter hole length nozzle of 0.5 mm achieved mixing process, shorten liquid length and superior entrainment compared with that of the longer hole length nozzle of 0.8 mm.
3. Surrounding gas density was found to be the most influential parameter to mixture formation and combustion rather than nozzle specifications.
4. At high boosted gas condition, the lower amount of soot produced by the shorter hole length nozzle was prominently exhibited due to strong combustion resulting in higher flame temperature and soot oxidation performed intensively during late combustion phase.
5. NOx emission was found to be a function of equivalence ratio of vapor fuel/air mixture at upstream of ignition and strongly related with adiabatic flame temperature.
6. The combustion and emission characteristics showed significant correlation with near-field spray behavior, particularly the influence of amount of fuel in vapor phase and entrainment of surrounding gas into the spray. The proper mixture preparation with high entrainment was declared to be a promising factor for efficient combustion with low soot emission at high boosted gas condition.

5.2 Future Works

There are other efforts which can be made in the following study.

1. This study employed a single-hole type nozzle for both spray and combustion experiment. For further observation, if the multiple hole type nozzle is used, spray formation is expected to be different due to complicated vortex and turbulence structure generated in sac volume.
2. There was an evidence that at high density gas condition showing high spray dispersion and faster vaporization. It is recommended to declare detailed mechanisms and fluid state under such high boosted gas condition.
3. In this study, a small combustion chamber was used for achieving high pressurized gas, so that spray either liquid or vapor phase would be impinged on the wall. Therefore, it is recommended to consider this impingement effect on combustion and emissions.